Volume 4. No. 2. June 2026

The Institution of Engineers of Kenya
Founded 1972

AJERI

African Journal of Engineering Research and Innovation

The Institution of Engineers of Kenya

ISSN: 2957- 7780

In partnership with

ENGINEERS BOARD OF KENYA

Enhancing Professionalism

ISSN: 2957- 7780

AJERI

African Journal of Engineering in Research and Innovation

ISSN: 2957- 7780 Volume 4. No 2. 2026

IEK

Published by:

The *Institution of Engineers of Kenya*

P.O Box 41346- 00100

Nairobi Kenya

Tel: +254 (20) 2729326, 0721 729363, (020) 2716922

Email: editor@iekenya.org

Website: www.iekenya.org

African Journal of Engineering Research and Innovation (AJERI), is published by ***The Institution of Engineers of Kenya,*** IEK, as an international forum for publication of high-quality papers in all areas of Engineering

ISSN: 2957- 7780

CONTENTS **Pages**

Error Analysis and SER Approximation of Correlated M-QAM Signals over Rayleigh Fading Channels

E. Omosa[1*], J. Obadha[2], M. Mutie[1]

[1]Faculty of Engineering, Chuka University, Chuka, Kenya

[2]Technical University of Kenya, Nairobi, Kenya

Corresponding author's email:edwinomosa@gmail.com

Abstract

This paper presents a comprehensive analysis of the Symbol Error Rate (SER) performance of M-ary Quadrature Amplitude Modulation (M-QAM) signals over correlated Rayleigh fading channels in the presence of additive white Gaussian noise (AWGN). The study focuses on three widely employed diversity combining techniques, namely Maximum Ratio Combining (MRC), Equal Gain Combining (EGC), and Selection Combining (SC). A unified closed-form approximate expression for the SER under the considered diversity schemes is derived, incorporating the effects of fading correlation, noise, and modulation order. The analytical formulation provides a tractable means of evaluating system reliability while enabling direct performance comparison among the three combining strategies. To assess the accuracy of the proposed expression, extensive Monte Carlo simulations are conducted using MATLAB, and the results confirm a high degree of consistency with the theoretical predictions. The findings demonstrate that correlation among diversity branches and the severity of fading significantly influence the error performance, thereby offering valuable insights for the design and optimization of diversity-assisted wireless communication systems operating in multipath fading environments.

Key words: MRC, EGC, SC, Rayleigh fading, diversity reception, correlated channels, Monte Carlo simulation

1. Introduction

The continuous evolution of wireless communication technologies has intensified the demand for high data rates, improved spectral efficiency, and reliable connectivity. Despite these advances, system performance remains fundamentally constrained by multipath fading and additive white Gaussian noise (AWGN), which cause random fluctuations in the amplitude and phase of received signals [1]. Among the different fading models, the Rayleigh distribution is widely used to characterize non-line-of-sight (NLOS) propagation environments, particularly in dense urban areas and indoor wireless networks [2], [3]. Under such conditions, the probability of symbol detection errors increases significantly, necessitating the deployment of robust error-mitigation strategies.

Diversity combining techniques are among the most effective methods for combating fading, as they exploit independent replicas of a transmitted signal captured through multiple antennas or propagation paths [4]. Three classical schemes have been extensively investigated: Maximum Ratio Combining (MRC), Equal Gain Combining (EGC), and Selection Combining (SC). MRC is theoretically optimal since it weights each branch according to its instantaneous signal-to-noise ratio (SNR), but it requires accurate channel state information (CSI) and entails high computational complexity. EGC reduces CSI requirements by coherently combining signals with equal amplitude weighting, though at some cost in performance relative to MRC. SC, on the other hand, offers a low-complexity approach by selecting the branch with the maximum SNR, albeit with inferior error performance compared to MRC and EGC [1], [3]-[6].

Over the past two decades, extensive research has focused on evaluating the SER of digital modulation schemes in fading environments. For example, closed-form SER expressions for M-ary Phase Shift Keying (M-PSK) and M-QAM under independent Rayleigh fading channels are well established in the literature. Analytical frameworks relying on conditional error probabilities, moment-generating functions, and Q-function approximations have provided valuable insights under idealized fading assumptions [7]-[9]. However, independent fading is rarely encountered in practice. Spatial and temporal correlation, often caused by limited antenna spacing, shared scatterers, or restricted propagation diversity, introduces dependencies across fading channels that can significantly degrade performance.

Recent works have extended error analysis to correlated fading environments, particularly in the context of multiple-input multiple-output (MIMO) systems, spatial modulation, and generalized fading models such as Nakagami-m, Ricean, and Weibull [10], [11]. These studies underscore the role of correlation modeling through frameworks such as Kronecker-based approaches and eigenvalue decompositions [10], [11].

Nevertheless, most existing analyses are restricted to specific receiver architectures, interference-limited systems, or alternative modulation formats. A unified, tractable SER framework for higher-order M-QAM in correlated Rayleigh fading channels with AWGN

MRC, EGC and SC remains largely unexplored. Moreover, several existing models rely on idealized uncorrelated assumptions or lack thorough simulation-based validation across a wide range of modulation orders and correlation regimes.

Motivated by these gaps, this paper develops a comprehensive analytical framework for evaluating the SER of M-QAM under correlated Rayleigh fading and AWGN with different diversity combining strategies. This problem is of particular importance given the widespread use of M-QAM in communication standards such as Wi-Fi, LTE, and 5G New Radio (NR), where optimizing trade-offs between performance, complexity, and implementation cost is critical.

The objectives of this study are:

1) To derive a closed-form approximate expression for the SER of M-QAM signals over correlated Rayleigh fading channels with AWGN under unified MRC, EGC, and SC combining.
2) To validate the analytical framework through extensive Monte Carlo simulations across different modulation orders and correlation scenarios.

The main contributions of this work are summarized as follows:

1) Develop a compact analytical expression that captures the combined effects of fading correlation, modulation order, and AWGN for a unified MRC, EGC, and SC.
2) Integrate correlation models into SER analysis, bridging the gap between idealized independent-fading assumptions and realistic propagation environments.
3) Verify the proposed expressions through Monte Carlo simulations, demonstrating their accuracy and robustness under diverse operating conditions.

Organization

The structure of this paper is as follows: Section I provides the introduction, while Section II outlines the system model. Section III presents the performance analysis, followed by the discussion of results in Section IV. Finally, Section V concludes the paper with closing remarks.

Notation

Throughout this paper, bold uppercase symbols are employed to represent matrices, whereas scalars are denoted using standard letters. The notation $Q(\cdot)$ refers to the Gaussian

Q-function. Furthermore, E[·], (·)*, and $(\cdot)^H$ are used to denote the expectation operator, complex conjugation, and Hermitian transpose, respectively.

2. System Model

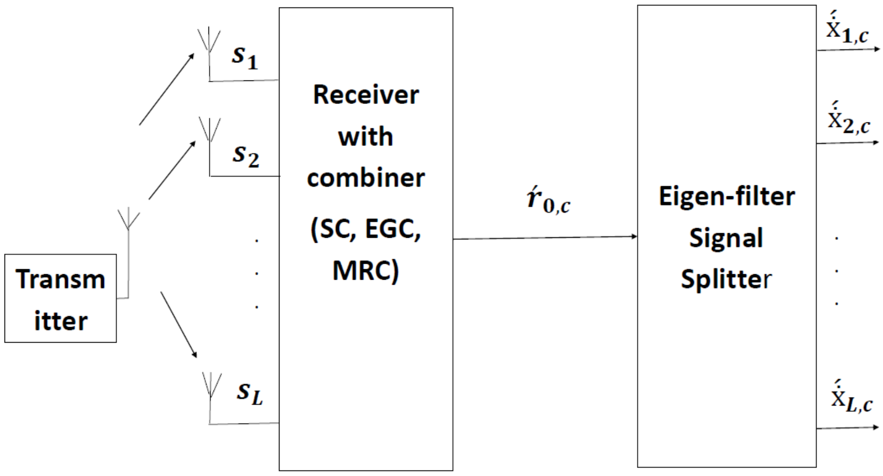

Figure.1: Illustration of the correlated system diversity model implementation.

An L-branch diversity system is considered. The correlated signals received from the L branches are combined using any diversity combiner e.g. MRC, EGC and SC, and equalized so as to obtain the estimate of the symbol $\acute{x}\ (0, c)$ sent by the transmitter. Where c represents the type of combiner. If the estimated symbol passes through a channel with a combined coefficient, $\hat{h}\ (0, c)$ then the combined signal output, $\acute{r}$(0,c) = $\hat{h}\ (0, c)\acute{x}\ (0, c)$. To analyze the L correlated signals, the combined signal output goes through a power splitter where a transformer decompose them into L independent symbols, $\acute{\acute{x}}_{(m,c)}, m \in\ [1{:}\,L]$ as illustrated in Figure 1. A transformer that can be applied in such a scenario is the Eigenvalue Decomposition (EVD) [10]-[12]

a. Correlated signal under Rayleigh

In diversity systems, the modulated correlated signal collected by the receiver of the L_{th} branch can be expressed as [12]:

$$s_k = \propto_L e^{j\Psi_L} x_m + n_L \tag{1}$$

where x_m is the transmitted symbol, $\propto_L$ denotes the random amplitude following a Rayleigh distribution, with E[${\propto_L}^2$] = $2{\sigma_L}^2$. The parameter Ψ_L represents a stochastic phase process, while n_L corresponds to additive zero-mean Gaussian noise. The noise components are assumed to be mutually uncorrelated and statistically independent of the transmitted signal.

By using the conventional method, a system correlation can be modeled. Taking the correlation coefficient between the l_{th} and the i_{th} branch to be ρ_{li} . This can be expressed as 10]-[12]:

$$\rho_{li} = \frac{E[\hat{h}_l \hat{h}^*{}_i]}{\sqrt{\sigma^2_{\hat{h}_l} \sigma^2_{\hat{h}_i}}}, i, l = 1,2, \dots L \tag{2}$$

where $\sigma^2_{\hat{h}_l}$is the variance of the random variables (RV) $\hat{h}_l$ and $\sigma^2_{\hat{h}_i}$ is is the variance of the RV $\hat{h}_i$.

Let **R** denote the normalized correlation matrix, which can be expressed as [13], [14]:

$$\boldsymbol{R} = \begin{pmatrix} 1 & \rho_{12} & \cdots & \rho_{1l} \\ \rho_{12} \vdots & 1 & \ddots & \rho_{2l} \vdots \\ \rho_l & \dots & \cdots & 1 \end{pmatrix} \tag{3}$$

The matrix **R** is considered positive-definite and, therefore, has strictly positive eigenvalues [2], [8]. By applying eigenvalue decomposition (EVD), **R** can be represented in terms of its orthogonal eigenvectors and corresponding eigenvalues. This transformation is typically realized through an eigen-filtering process, as described in [12]-[15].

$$\Lambda = \boldsymbol{QRQ}^H \tag{4}$$

where **Q** denotes the matrix composed of eigenvectors, while Λ represents the diagonal matrix containing the positive eigenvalues. The EVD process produces **Q**, whose rows form an orthonormal basis, thereby making **Q** a unitary matrix. Consequently, it satisfies the property $\boldsymbol{Q}^H$=Q^{-1}. The transformation network defined by **Q** is reciprocal in nature. Therefore, **Q** functions as the eigen-filter or diversity de-correlator, providing the output through a unitary transformation of the input.

b. Eigen-filter Operation

The purpose of the eigen-filter diversity de-correlator is to de-correlate received envelop signal vector $\hat{\boldsymbol{r}}_{c,d}$ of length L. Generally, a filter $\mathbf{h}_f$ of length L, would be needed to produce a new uncorrelated signal estimates $\hat{\hat{\boldsymbol{x}}}_{c,d}$. the filter output vector is customary expressed as $\hat{\hat{\boldsymbol{x}}}_{0,d}$ =$\boldsymbol{h}_f^H \hat{\boldsymbol{r}}_{c,d}$ [15]. As a result, the signal power at the output of the filter is written as [12], [15]:

$$\begin{aligned} p_{0,d} &= E\left[\left|\hat{\hat{\boldsymbol{x}}}_{0,d}\right|^2\right] \\ &= \left(\boldsymbol{h}_f^H \hat{\boldsymbol{r}}_{c,d}\right)\left(\hat{\boldsymbol{r}}_{c,d}^H \boldsymbol{h}_f\right) \\ &= \boldsymbol{h}_f^H \hat{\boldsymbol{R}} \boldsymbol{h}_f \\ &= \boldsymbol{h}_f^H \left(\hat{\boldsymbol{Q}}^H \hat{\Lambda} \hat{\boldsymbol{Q}}\right) \boldsymbol{h}_f \\ &= \sqrt{\hat{\Lambda}}\left(\hat{\boldsymbol{Q}} \boldsymbol{h}_f\right)^H \sqrt{\hat{\Lambda}}\left(\hat{\boldsymbol{Q}} \boldsymbol{h}_f\right) \end{aligned} \tag{5}$$

where $\widehat{\boldsymbol{R}} = \hat{\boldsymbol{r}}_{c,d}\hat{\boldsymbol{r}}_{c,d}^{H}$ is the autocorrelation of $\hat{\boldsymbol{r}}_{c,d}$ and $\widehat{\Lambda}$ contains the eigenvalues of $\widehat{\boldsymbol{R}}$. Also, the autocorrelation $\widehat{\boldsymbol{R}}$= **R** and $\widehat{\Lambda} = \Lambda$ [16].

Choosing the filter coefficients vector to be $\boldsymbol{h}_f = \widehat{\boldsymbol{Q}}$, rewriting, Equation (5) becomes:

$$\begin{aligned} p_{0,d} &= \boldsymbol{h}_f^H\left(\widehat{\boldsymbol{Q}}^H\,\widehat{\Lambda}\widehat{\boldsymbol{Q}}\right)\boldsymbol{h}_f \\ &= \sqrt{\widehat{\Lambda}}\left(\widehat{\boldsymbol{Q}}\boldsymbol{h}_{\boldsymbol{f}}\right)^H\sqrt{\widehat{\Lambda}}\left(\widehat{\boldsymbol{Q}}\boldsymbol{h}_f\right) \\ &= \sqrt{\widehat{\Lambda}}\left(\widehat{\boldsymbol{Q}}\widehat{\boldsymbol{Q}}\right)^H\sqrt{\widehat{\Lambda}}\left(\widehat{\boldsymbol{Q}}\widehat{\boldsymbol{Q}}\right) \end{aligned} \tag{6}$$

From Equation (6), the equivalent channel coefficient corresponding to the L_{th} output branch can be written as:

$$\hat{h}_L = \sqrt{\boldsymbol{\epsilon}_L}\widehat{\boldsymbol{Q}}_L\widehat{\boldsymbol{Q}}_L = \sqrt{\boldsymbol{\epsilon}_L}\widehat{\boldsymbol{Q}}_L\hat{\hat{\boldsymbol{h}}} \tag{7}$$

where $\boldsymbol{\epsilon}_L \in \Lambda$ and $\widehat{\boldsymbol{Q}}_L$ represents the k_{th} column of $\widehat{\boldsymbol{Q}}$. The term $\hat{\hat{\boldsymbol{h}}}_L$ denotes the approximated Rayleigh fading channel in a correlated system, characterized by a complex coefficient whose amplitude follows a circularly symmetric complex Gaussian distribution, CN(0,1), while the phase is uniformly distributed over $(0, 2\pi)$. As established in [16], the resulting product yields statistically independent entries. Hence, the correlated branches can be regarded as eigenvalue-weighted representations of otherwise independent fading paths. Normally, **Q** is computed from **R** or given. Therefore, this paper provides a blind filter matrix **Q** that does not consist of the evaluation of **R**

Performance of MQAM in AWGN channel

In this segment, the consequences of Rayleigh Fading with MQAM are assessed. The SER will be used as the measure of performance.

The SER of square MQAM at an instantaneous signal-to-noise ratio, $\gamma_L = h^2\frac{E_s}{N_0}$ in AWGN channel is expressed as [1], [2], [7], [17], [18]:

$$SER_{MQAM} = 4\left(1 - \frac{1}{\sqrt{M}}\right)Q\left(\sqrt{\frac{3E_s}{N_0(M-1)}}\right) - 4\left(1 - \frac{1}{\sqrt{M}}\right)^2 Q^2\left(\sqrt{\frac{3E_s}{N_0(M-1)}}\right)$$

(8)

h^2 denotes the instantaneous power of the fading channel, where h is a random variable representing the channel gain. The ratio $\frac{E_s}{N_0} = \gamma$ corresponds to the symbol energy-to-noise power density in an AWGN channel without fading. By defining $a = \left(1 - \frac{1}{\sqrt{M}}\right)$ and $= \frac{3}{M-1}$, the preceding expression simplifies to:

$$SER_{MQAM} = 4aQ\left(\sqrt{b\gamma}\right) - 4a^2Q^2\left(\sqrt{b\gamma}\right) \tag{9}$$

Q is the Marcum Q-function, $Q\left(\sqrt{b\gamma}\right)$ *and* $Q^2\left(\sqrt{b\gamma}\right)$are given by Craig's formula as [19]:

$$Q\left(\sqrt{b\gamma}\right) = \frac{1}{\pi}\int_0^{\frac{\pi}{2}} exp\left(-\frac{b\gamma}{2sin^2\theta}\right) d\theta \tag{10}$$

$$Q^2\left(\sqrt{b\gamma}\right) = \frac{1}{\pi}\int_0^{\frac{\pi}{4}} exp\left(-\frac{b\gamma}{2sin^2\theta}\right) d\theta \tag{11}$$

Solving for $Q\left(\sqrt{b\gamma}\right)$ *and* $Q^2\left(\sqrt{b\gamma}\right)$ using the trapezoidal rule, they become:

$$Q\left(\sqrt{b\gamma}\right) = \frac{1}{2n}\left(\frac{e^{-b\gamma/2}}{2} + \sum_{k=1}^{n-1} e^{-\left(\frac{b\gamma}{2sin^2\left(\frac{k\pi}{2n}\right)}\right)}\right)$$

(12)

$$Q^2\left(\sqrt{b\gamma}\right) = \frac{1}{4t}\left(\frac{e^{-b\gamma}}{2} + \sum_{k=1}^{t-1} e^{-\left(\frac{b\gamma}{2sin^2\left(\frac{k\pi}{4t}\right)}\right)}\right)$$

(13)

By Letting n=2t and substituting the above Equations (12) and (13) in Equation (9) gives:

$$SER_{MQAM} = \frac{a}{t}\left\{\frac{e^{-b\gamma/2}}{2} - \frac{ae^{-b\gamma}}{2} + (1-a)\sum_{i=1}^{t-1} e^{-\frac{b\gamma}{S_i}} + \sum_{i=t}^{2t-1} e^{-b\gamma/S_i}\right\} \tag{14}$$

Where t is the sampling frequency, $S_i = 2sin^2\theta_i$ and $\theta_i = \frac{i\pi}{4}$

a. Performance of MQAM in AWGN channel under Rayleigh Fading

If α is the fading coeffient of Rayleigh fading channel with a probability density function (PDF) of $\gamma = \alpha^2\frac{E_s}{N_0}$ expressed as $f_\gamma(\gamma) = \frac{1}{\bar{\gamma}}exp\left(-\frac{\gamma}{\bar{\gamma}}\right)$ [2], [19] then the conditional SER for QAM is given as:

$$SER_{MQAM}(e|\propto^2) = \frac{a}{t}\left\{\frac{e^{-b\gamma/2}}{2} - \frac{ae^{-b\gamma}}{2} + (1-a)\sum_{i=1}^{t-1} e^{-\frac{b\gamma}{S_i}} + \sum_{i=t}^{2t-1} e^{-b\gamma/S_i}\right\}$$

(15)

Where $\bar{\gamma}$-is the average received signal to noise ratio $\bar{\gamma} = E[\gamma] = E\left[\alpha^2 \frac{E_s}{N_0}\right] = E[\alpha^2]\frac{E_s}{N_0}$[12] Assuming $E[\alpha^2] = 1$, then $\bar{\gamma}$=$\frac{E_s}{N_0}$.

The average symbol error probability of M-QAM in Rayleigh fading channel is expressed as [19]:

$$P_{ser} = E\left[SER_{MQAM}(e|\alpha^2)\right] = \int_0^\infty SER_{MQAM}(e|\gamma)\, f_\gamma(\gamma) d\gamma \quad (16)$$

Though substitution Equation (16) becomes:

$$P_{ser} = \int_0^\infty \frac{a}{t}\left(\frac{e^{-b\gamma/2}}{2} - \frac{ae^{-b\gamma}}{2} + (1-a)\sum_{i=1}^{t-1} e^{-\frac{b\gamma}{S_i}} + \sum_{i=t}^{2t-1} e^{-b\gamma/S_i}\right)\frac{1}{\bar{\gamma}} e^{-\frac{\gamma}{\bar{\gamma}}} d\gamma \quad (17)$$

Solving Equation 17() result in Equation (18).

$$P_{ser} = \frac{a}{t}\left(\frac{1}{2}\frac{2}{b\bar{\gamma}+2} - \frac{a}{2}X\frac{1}{b\bar{\gamma}+1} + (1-a)\sum_{i=1}^{t-1}\frac{S_i}{b\bar{\gamma}+S_i} + \sum_{i=t}^{2t-1}\frac{S_i}{b\bar{\gamma}+S_i}\right) \quad (18)$$

b. Receive Diversity with N Receive Antennas

For a SIMO system with L receive antennas the signal received on the L_{th} antenna is given as [10]-[16]:

$$y_L = h_L x + n_L \quad (19)$$

Where $y_L$is the received signal on the receive antenna,h_L- channel gain on the L_{th} receive antenna, x- transmitted signal and n_L- noise on the L_{th} receive antenna which is modeled as AWGN.

c. Diversity Combining with Maximal ratio combining (MRC)

For MRC the PDF of the combined SNR is given as [4], [5]

$$f_\gamma(\gamma) = \frac{1}{(L-1)!\bar{\gamma}^L}\gamma^{L-1}e^{\frac{\gamma}{\bar{\gamma}}} \quad (20)$$

Further, the SER for MRC can be expressed as

$$P_{ser\_MRC} = \prod_k^L E\left[SER_{MQAM}(e|\overline{\gamma})\right] = \int_0^\infty \prod_k^L SER_{MQAM}(e|\overline{\gamma})\ f_\gamma(\overline{\gamma})d\gamma$$

(21)

$$P_{ser\_MRC} = \int_0^\infty \prod_k^L \frac{a}{t}\left\{\frac{e^{-b\gamma/2}}{2} - \frac{ae^{-b\gamma}}{2} + (1-a)\sum_{i=1}^{t-1} e^{-\frac{b\gamma}{S_i}} + \sum_{i=t}^{2t-1} e^{-b\gamma/S_i}\right\}\frac{\gamma^{L-1}}{(L-1)!\overline{\gamma}^L} e^{\frac{\gamma}{\overline{\gamma}}}\, d\gamma$$

(22)

Equation (22) can be solved using Moment Generating Function (MGF). MGF is defined as [20]

$$M_\gamma(s) = \int_0^\infty \ldots \int_0^\infty exp(-s\sum_{k=1}^L \gamma_k)\ \prod_k^L\left(f_\gamma(\gamma_k)d\gamma_k\right) = \prod_k^L M_{\gamma_k}(s)$$

(23)

where

$$M_{\gamma_k}(s) = \exp(-s\gamma_k)\, f_\gamma(\gamma_k)d\gamma_k = \frac{1}{\hat{\gamma}_k}\int_0^\infty \exp\left[-\gamma_k\left(\frac{1}{\hat{\gamma}_k} - s\right)\right] d\gamma_k = \frac{1}{1-\hat{\gamma}_k s}$$

For the case where L=1, Equation (22) reduces to Equation (18). Substituting Equation (18) into Equation (22) and solving results in:

$$P_{ser\_MRC} = \frac{a}{t}\left[\frac{1}{2}\prod_{k=1}^L \frac{2}{b\overline{\gamma}+2} - \frac{a}{2}\prod_{k=1}^L \frac{1}{b\overline{\gamma}+1} + (1-a)\sum_{i=1}^{t-1}\prod_{k=1}^L \frac{S_i}{b\overline{\gamma}+S_i} + \sum_{i=t}^{2t-1}\prod_{k=1}^L \frac{S_i}{b\overline{\gamma}+S_i}\right]$$

(24)

d. Diversity Combining with Equal gain combining (EGC)

A unified formulation for the three conventional combining techniques can be obtained by incorporating the average received branch SNR, denoted as $\bar{\gamma}$. Accordingly, the expected output SNR for each EGC branch is expressed as [3], [5]:

$$\overline{\gamma}_{k,EGC} = \epsilon_k \frac{\overline{\gamma}_{0,EGC}}{L} = \epsilon_k\left(\frac{1+(L-1)\frac{\pi}{4}}{L}\right)\bar{\gamma} \quad (25)$$

e. Diversity Combining with Selection combining (SC)

On the same note as in EGC, the mean output SNR for each SC branch can be expressed as [16], [19]-[21]:

$$\overline{\gamma}_{k,SC} = \epsilon_k \frac{\overline{\gamma}_{0,SC}}{L} = \epsilon_k \left(\frac{\sum_{i=1}^{L}\frac{1}{i}}{L}\right)\overline{\gamma} \tag{26}$$

Equation (25) and Equation (26) can be combined as:

$$\overline{\gamma}_{0,C} = \epsilon_k \beta_c \overline{\gamma} \tag{27}$$

$$\text{Where } \beta_c = \begin{cases} \beta_{MRC} = 1 \; for \; MRC \\ \beta_{EGC} = \frac{1+(L-1)\frac{\pi}{4}}{L} \; for \; EGC \\ \beta_{SC} = \frac{\sum_{i=1}^{L}\frac{1}{i}}{L} \; for \; SC \end{cases}$$

Substituting Equation (27)into Equation (24), it becomes

$$P_{ser} = \frac{a}{t}\left[\frac{1}{2}\prod_{k=1}^{L}\frac{2}{b\overline{\epsilon_k\beta_c\gamma}+2} - \frac{a}{2}\prod_{k=1}^{L}\frac{1}{b\epsilon_k\beta_c\overline{\gamma}+1} + (1-a)\sum_{i=1}^{t-1}\prod_{k=1}^{L}\frac{S_i}{b\epsilon_k\beta_c\overline{\gamma}+S_i} + \sum_{i=t}^{2t-1}\prod_{k=1}^{L}\frac{S_i}{b\epsilon_k\beta_c\overline{\gamma}+S_i}\right] \tag{28}$$

3. Simulations

In the simulation and theoretical analysis, a system with four receiving antennas was considered. The antennas were placed with uniform spacing, each separated by half the wavelength of a 5G carrier signal operating at 60 GHz. The correlation coefficient, which quantifies the relationship between signals at different antennas, was expressed as [10]-[16]:

$$\rho = J_0\left(2\pi\frac{l}{\lambda}\right) \tag{29}$$

where λ is the carrier wavelength, l is the distance between antennas, and J_0 represents the zero-order Bessel function.

For the simulation setup, antenna spacing was deliberately restricted to values not exceeding half the operating wavelength (λ/2). This design choice reflects a well-established principle: antenna elements spaced more than λ/2 apart exhibit reduced signal correlation, resulting in higher statistical independence, whereas smaller separations lead to stronger correlations. To balance practical implementation constraints and spatial limitations, spacing values of 0.15λ,

0.25λ, and 0.45λ were selected. These configurations were considered adequate for the objectives of this study. The resulting correlation coefficients naturally fall within the standard range $0< \rho < 1$.

$$\rho = J_0\left(2\pi\frac{Ll}{\lambda}\right) \tag{30}$$

Based on Equation (30), the parameters applied in the simulation are summarized in **Table 1**.

Table 1. Parameters Used in the Simulation

l (spacing)	$J_0\left(2\pi\frac{l}{\lambda}\right)$	$J_0\left(2\pi\frac{2l}{\lambda}\right)$	$J_0\left(2\pi\frac{3l}{\lambda}\right)$	$J_0\left(2\pi\frac{4l}{\lambda}\right)$
0.15λ	0.7900	0.2906	-0.1962	-0.4020
0.25λ	0.4720	-0.3042	-0.2659	0.2203
0.45λ	-0.1962	0.0452	0.0468	-0.1100

From these correlation coefficients, the correlation matrix can be constructed. Since no direct analytical method exists for processing correlated signals, the matrix is decomposed through Eigenvalue Decomposition (EVD), which effectively produces independent signal branches.

To demonstrate, consider three uniformly spaced receive antennas with an inter-element distance of $l = 0.45\lambda$ and correlation coefficient ρ. The resulting correlation matrix **R**, derived from Equation (3), Equation (30) and Table 1, is:

$$\boldsymbol{R} = \begin{pmatrix} 1 & -0.1962 & 0.0452 & 0.0468 \\ -0.1962 & 1 & -0.1962 & 0.0452 \\ 0.0452 & -0.1962 & 1 & -0.1962 \\ 0.0468 & 0.0452 & -0.1962 & 1 \end{pmatrix} \tag{31}$$

Furthermore, using EVD, the eigenvalue matrix corresponding to Equation (31), obtained from simulation through the KLT, can be expressed as:

$$\Lambda_4 = \begin{pmatrix} 1.3450 & 0 & 0 & 0 \\ 0 & 1.1191 & 0 & 0 \\ 0 & 0 & 0.8044 & 0 \\ 0 & 0 & 0 & 0.7315 \end{pmatrix} \tag{32}$$

Finally, the simulation included an iterative process defined by parameter t, representing the number of iterations. The value was set to (t=15), as further iterations (t >15) did not significantly enhance the accuracy of results.

4. Results and Discussions

In this section, the results obtained through Monte Carlo simulations are compared with those derived from analytical formulations to validate their accuracy. The analysis investigates the performance of the proposed approach across different antenna configurations for 4-QAM, 16-QAM, 64-QAM and 256-QAM modulation schemes. The evaluation is conducted over a Rayleigh fading channel, with the SER adopted as the key performance metric. In the figure legends, 'Sim' and 'Theory' are used to denote simulation-based and analytical outcomes, respectively.

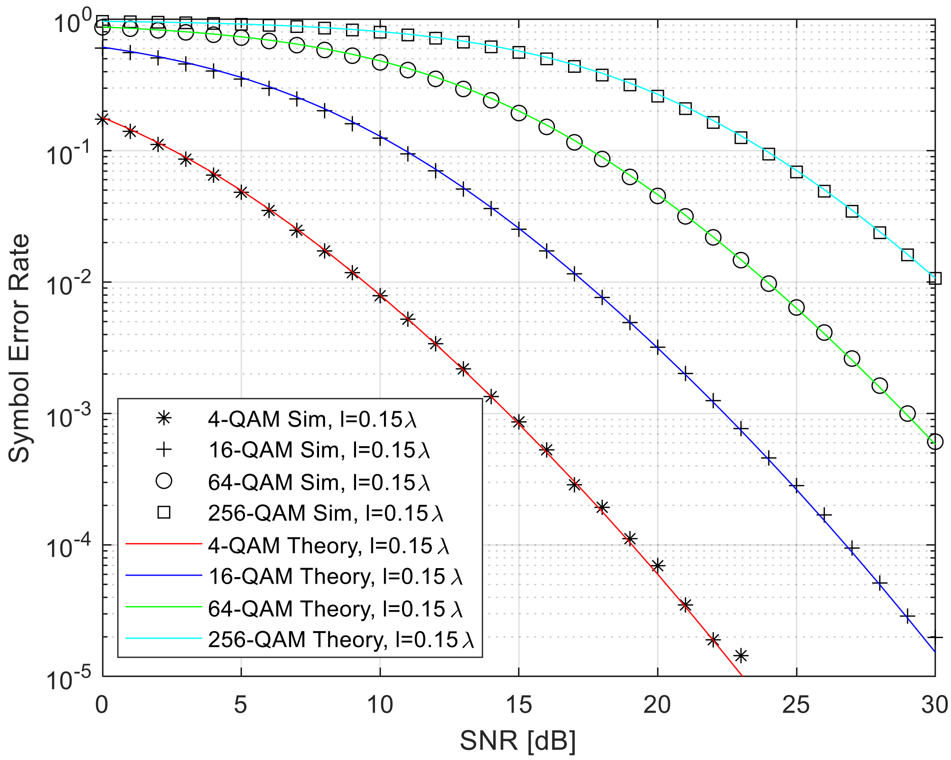

Figure 2: SER performance of EGC with 4QAM, 16QAM, 64QAM and 256QAM for 3 correlated branches at antenna spacing l=0.15λ

Figure 2 illustrates that at lower modulation orders, such as 4-QAM, the system achieves substantially lower SER across all SNR levels. As the modulation order increases to 16-QAM, 64-QAM, and 256-QAM, performance deteriorates due to the reduced Euclidean distance between constellation points, which increases susceptibility to noise and fading. While all modulation schemes exhibit high SER at low SNRs, 4-QAM consistently demonstrates superior robustness. At moderate to high SNRs, higher-order modulations, particularly 64-QAM and 256-QAM, exhibit noticeable error floors, underscoring the trade-off between spectral efficiency and reliability. Furthermore, the close agreement between theoretical and simulated results confirms the validity of the analytical framework.

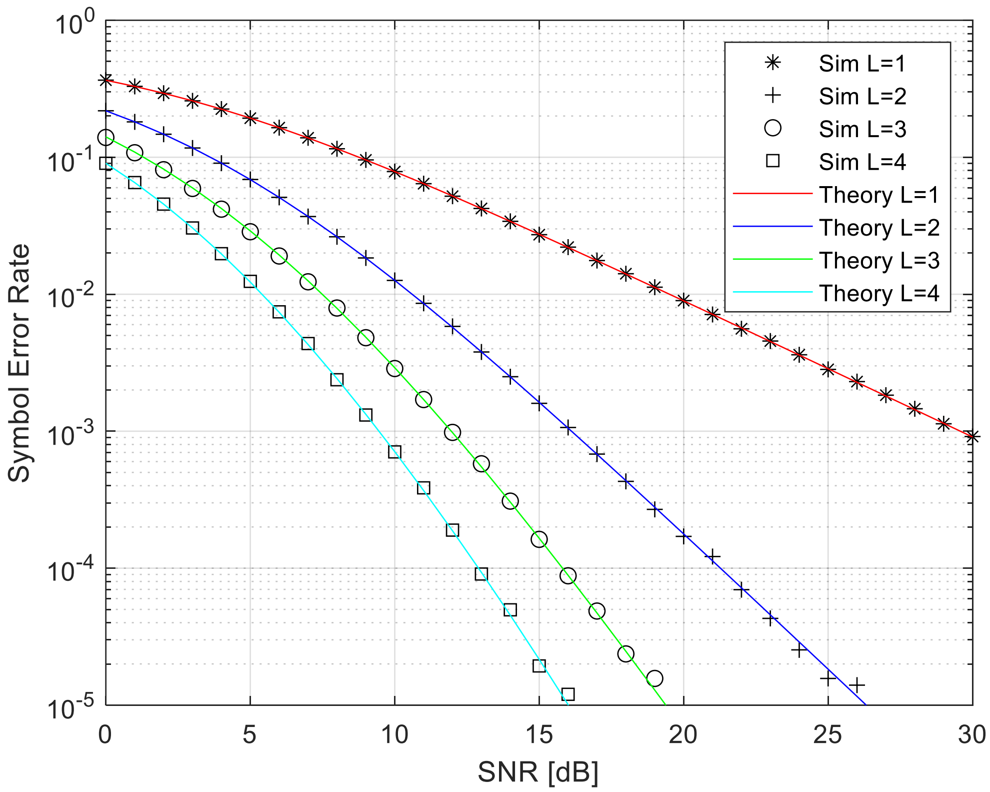

Figure 3: BER performance of MRC with 4QAM for 1, 2, 3, and 4 correlated branches at antenna spacing l=0.25λ

Figure 3 presents the performance of MRC with 4-QAM for 1 to correlated receive branches at an antenna spacing of l=0.25λ, corresponding to a moderate correlation coefficient. The results show that increasing the number of branches lowers the SER at a given SNR. At low SNRs, all curves converge due to noise dominance, whereas at moderate-to-high SNRs, the curves diverge, with correlation effects limiting the achievable diversity gains as L increases. The close agreement between analytical and simulation results further validates the accuracy of the analysis.

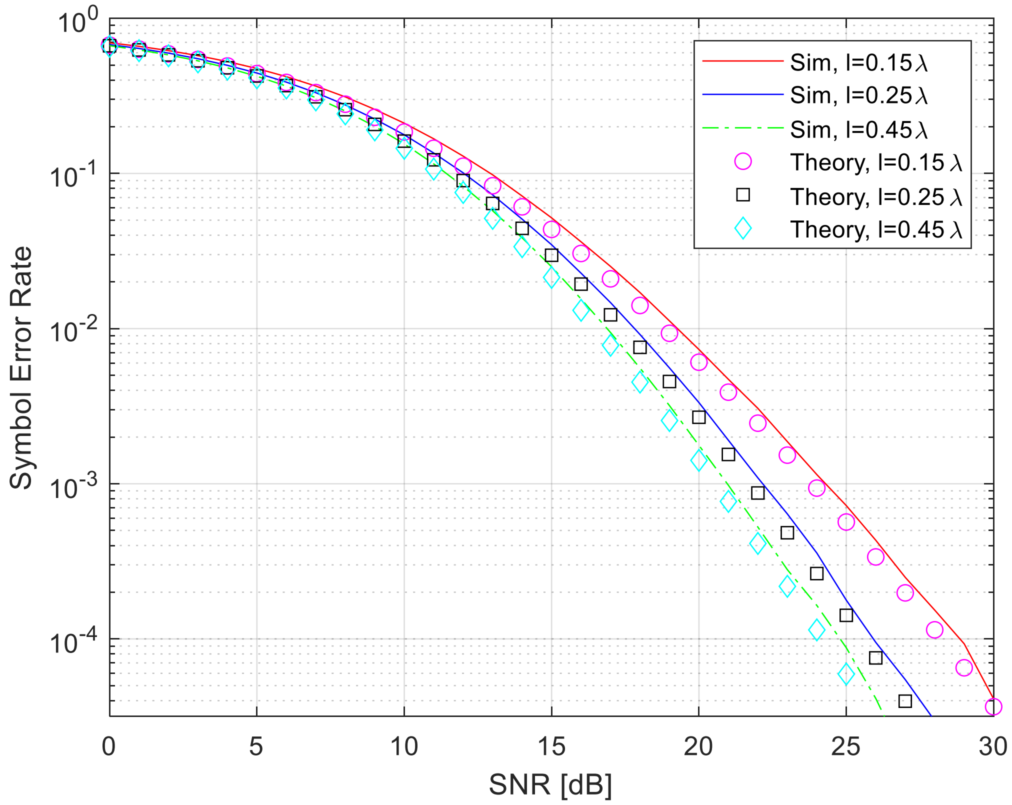

Figure 4: BER performance of SC employing 16QAM for 4 correlated branches at antenna spacings of d=0.15λ, d=0.25λ, and d=0.45λ.

Figure 4 illustrates the SER performance of EGC with 16-QAM for four correlated branches. The results highlight the impact of antenna spacing: small spacing (0.15λ) yields the poorest performance due to strong correlation, moderate spacing (0.25λ) provides partial diversity benefits, while larger spacing (0.45λ) offers the best results by approximating uncorrelated fading. Theoretical curves closely match the simulations across the full SNR range, confirming the reliability of the analysis.

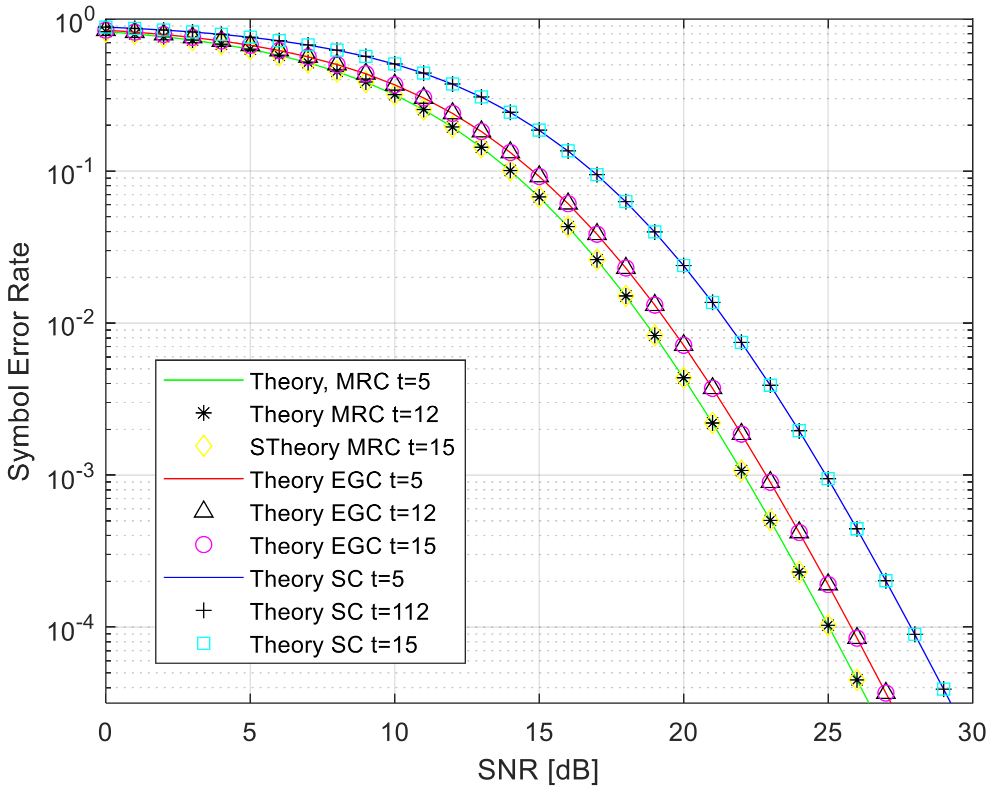

Figure 5: BER comparison of SC, EGC, and MRC combining techniques with 64QAM for L=4 correlated branches at antenna spacing d=0.45λ.

Figure 5 presents the BER performance comparison of SC, EGC, and MRC combining schemes employing 64-QAM for L=4 correlated branches at an antenna spacing of l=0.45λ. Among the three techniques, MRC achieves the lowest error rates, followed by EGC and then SC. The curves corresponding to t=10, 12, and 15 are closely aligned, indicating that the approximation error of the Q-function becomes negligible for t>10. Consequently, t=10 was adopted in the simulations without loss of accuracy.

5. Conclusions

This paper has presented a unified analytical and simulation-based study of the SER performance of square M-QAM signals over correlated Rayleigh fading channels under AWGN. Three diversity combining schemes; MRC, EGC, and SC were evaluated, highlighting the influence of correlation, antenna spacing, and modulation order on system reliability. Results confirm that MRC provides the best performance, followed by EGC and SC, while higher modulation orders suffer greater degradation due to reduced Euclidean distances between symbols. The close alignment between theoretical analysis and Monte Carlo simulations validates the accuracy of the proposed framework. These findings offer practical insights into the trade-offs between spectral efficiency, diversity order, and correlation effects, which are critical for the design of robust next-generation wireless communication systems.

Future Work

Future research can extend this work in several directions. First, exploring generalized fading models such as Rician, or Weibull would provide deeper insights into more diverse propagation conditions. Second, the integration of advanced combining techniques and hybrid diversity schemes could be investigated to further mitigate correlation effects. Third, secrecy capacity and outage probability analysis under correlated fading channels may offer valuable contributions to the design of secure wireless systems. Finally, applying machine learning and adaptive signal processing methods to optimize combining strategies in real-time presents a promising avenue for enhancing the performance of 5G and emerging 6G networks.

References

[1]. R. Mehta, "Performance analysis of Rayleigh fading wireless networks with multiple propagation paths and spatial diversity"**,** *International Journal of Wireless and Mobile Computing*, vol. 25, no. 4, pp. 309–321, 2023.

[2]. A. Abdelbari and B. Bilgehan, "The derivation of the probability of error for BPSK, 16-QAM and 64-QAM in Rayleigh fading channel: A unified approach", arXiv preprint arXiv:2406.16548, 2024.

[3]. F. A. García, H. C. Mora, and N. O. Garzón, "Improved exact evaluation of equal-gain diversity receivers in Rayleigh fading channels," *IEEE Access*, vol. 10, pp. 26974–26984, 2022.

[4]. S. Hawaibam and A. D. Singh, "Performance evaluation of L-maximal ratio combining diversity with estimation error for Shadowed Beaulieu-Xie fading channels," *International Journal of Communication Systems*, vol. 37, no. 3, 2024.

[5]. A. Chauhan, M. I. Hasan, S. Singh, I. H. Khan, and R. Ya, "Mean SNR Analysis of Different Diversity Combining Techniques Under Nakagami-m Fading Channels—A Review," in *2024 International Conference on Computer, Electronics, Electrical Engineering & their Applications (IC2E3)*, pp. 1–6, Jun. 2024.

[6]. W. K. New, K. K. Wong, H. Xu, K. F. Tong, and C. B. Chae, "Fluid antenna system: New insights on outage probability and diversity gain," *IEEE Transactions on Wireless Communications*, vol. 23, no. 1, pp. 128–140, 2023.

[7]. C. Liu and N. C. Beaulieu, "Exact SER and BER analysis on jointly optimal maximum likelihood detection of two QPSK signals with phase offset", *IEEE Transactions on Vehicular Technology*, vol. 70, no. 11, pp. 11695–11709, November 2021.

[8]. P. K. Singya, P. Shaik, N. Kumar, V. Bhatia, and M. S. Alouini, "A survey on higher-order QAM constellations: Technical challenges, recent advances, and future trends", *IEEE Open Journal of the Communications Society*, vol. 2, pp. 617–655, 2021.

[9]. R. E. Mvone, C. Hannachi, D. Hammou, E. Moldovan, and S. O. Tatu, "Optimization of 16-QAM and 32-QAM constellations for mitigating impairments of phase noise in millimeter-wave receivers", *IEEE Transactions on Wireless Communications*, vol. 21, no. 6, pp. 3605–3616, June 2021.

[10]. D. Lato and R. Mudoi, "Physical Layer Security Analysis for Correlated Nakagami-m Fading Channel," in *International Conference on Communication, Devices and Networking*, Singapore: Springer Nature Singapore, Jan. 2024, pp. 249–259.

[11]. D. Ayanda, S. Solwa, and K. Abdulsalam, "Eigenfilter-based analysis of uncoded space-time labeling diversity with three transmit antennas in correlated Nakagami-m fading channels," *Trans. Emerg. Telecommun. Technol.*, vol. 34, no. 6, 2023.

[12]. E. Omosa, P. O. Akuon, and V. O. Kalecha, "A unified symbol error rate (SER) expression for equal gain combining (EGC) and maximum ratio combining (MRC) over correlated Nakagami-m fading channels," *AJERI*, vol. 2, no. 3, 2024.

[13]. J. Lin and H. Poor, "Optimum combiner for spatially correlated Nakagami-m fading channels," *IEEE Transactions on Wireless Communications*, vol. 20, no. 2, pp. 771–784, Feb. 2020.

[14]. A. Olutayo, J. Cheng, and J. F. Holzman, "Performance bounds for diversity receptions over a new fading model with arbitrary branch correlation," *EURASIP Journal on Wireless Communications and Networking*, vol. 2020, no. 1, 2020.

[15]. E. Omosa, P. Akuon, H. Xu, and V. Oduol, "Gain of spatial diversity with conjoint signals in arbitrarily correlated Rayleigh fading channels," *Wireless Communications and Mobile Computing*, vol. 2023, no. 1, pp. 1–12, 2023.

[16]. S. Al-Juboori and X. Fernando, "Characterizing a decorrelator for selection combining receivers in Nakagami-m fading channels," *AEU - International Journal of Electronics and Communications*, vol. 106, pp. 12–19, 2019.

[17]. Y. Jang, J. Park, and I. Kim, "BER expression of QAM for symbol-level jamming", *IEEE Transactions on Wireless Communications*, vol. 21, no. 2, pp. 1037–1048, February 2021.

[18]. R. E. Mvone, C. Hannachi, D. Hammou, E. Moldovan, and S. O. Tatu, "Optimization of 16-QAM and 32-QAM constellations for mitigating impairments of phase noise in millimeter-wave receivers*", IEEE Transactions on Wireless Communications*, vol. 21, no. 6, pp. 3605–3616, June 2021.

[19]. E. Omosa, P. Akuon, and O. Kalech., "Reed-solomon(rs) coding gain on correlated rayleigh fading," *2019 IEEE AFRICON. IEEE Xplore*, July 2020.

[20]. R. Deergha, Channel Coding Techniques for Wireless Communications, S. M, Springer (India) Pvt. Ltd.: Springer, 2015, no. ISBN 978-81-322- 2291-0.

[21]. H. Al-Hmood and H. S. Al-Raweshidy, "Performance analysis of mmWave communications with selection combining over fluctuating-two ray fading model," *IEEE Communications Letters*, vol. 25, no. 8, pp. 2531–2535, 2021.

Optimization of Solar Photovoltaic Systems for Maximum Direct Normal Irradiance Capture and Hybrid Diesel-PV Modelling in a Marine Environment

P. C. Kimunguyi*, M. Saulo, S. Kariuki, G. G. Kidegho.

Department of Technical University of Mombasa, Mombasa, Kenya

Corresponding author's email: peterkimunguyi@gmail.com

Abstract

The maritime sector faces increasing pressure to reduce greenhouse gas emissions and operational fuel costs, motivating the integration of renewable energy into shipboard power systems. While solar photovoltaic (PV) systems present a viable solution for auxiliary power generation, their effectiveness in marine environments is significantly constrained by vessel motion, which degrades Direct Normal Irradiance (DNI) capture and overall energy yield. This study proposes an optimized marine PV framework incorporating an artificial intelligence (AI)–based dual-axis gimbal tracking system to maximize DNI under dynamic roll, pitch, and yaw conditions. A comprehensive simulation model was developed in MATLAB/Simulink using coastal solar and environmental data from Mombasa, Kenya, and applied to the auxiliary power demand of the MV Safari ferry (432.5 kWh/day). The AI tracker predicts optimal tilt and azimuth angles in real time based on vessel motion, solar position, and measured irradiance, enabling effective motion compensation. Results demonstrate that the proposed system maintains up to 90% effective irradiance under moderate sea states and achieves a 17% increase in energy yield compared to a fixed-tilt marine PV configuration. When integrated into a hybrid diesel–PV–battery system, solar energy supplies 57.66% of the daily load, reducing diesel generator runtime by approximately 57.66% and lowering annual CO_2 emissions by 101.5 tonnes. A techno-economic assessment indicates a 4-year payback period, confirming the economic viability of the proposed solution. The findings establish a scalable and replicable approach for optimizing solar energy utilization in marine environments and support the broader decarbonization of maritime auxiliary power systems.

Keywords: AI-based solar tracking, direct normal irradiance optimization, hybrid diesel–PV–battery systems, marine solar photovoltaic system and shipboard energy management system

1. Introduction

Marine vessels continue to rely predominantly on diesel generators to supply auxiliary and hotel loads, resulting in high fuel consumption, elevated operating costs, and significant greenhouse gas emissions. In response to increasingly stringent environmental regulations and global decarbonization initiatives, hybrid shipboard power systems incorporating renewable energy sources have gained substantial research and industrial attention. Solar photovoltaic (PV) technology is particularly attractive for auxiliary power applications due to its modularity, scalability, and compatibility with existing marine electrical infrastructure.

Despite these advantages, the deployment of PV systems in marine environments is fundamentally challenged by vessel motion. Wave-induced dynamics and operational manoeuvres cause continuous variations in roll, pitch, and yaw, leading to misalignment between the solar radiation vector and the PV surface. This misalignment reduces Direct Normal Irradiance (DNI) capture and degrades energy yield, particularly for fixed-tilt installations. Several studies have reported substantial performance degradation of marine PV systems under moderate sea states, highlighting the need for motion-aware solar tracking solutions.

Conventional solar tracking approaches applied in maritime contexts typically rely on astronomical sun-position algorithms or predefined control strategies. While effective under steady conditions, these methods exhibit limited adaptability to rapid and stochastic vessel motion and often neglect the coupled interaction between ship dynamics and irradiance variability. Furthermore, most existing marine PV studies treat solar irradiance as a quasi-static input, overlooking the nonlinear and time-varying nature of DNI in dynamic marine environments.

Recent advances in artificial intelligence (AI) and data-driven control techniques provide new opportunities to address these limitations. By leveraging real-time inertial measurement unit (IMU) data, solar position information, and irradiance measurements, AI-based models can learn complex nonlinear relationships governing DNI availability under motion-affected conditions. Such models enable adaptive solar tracking strategies capable of compensating for vessel dynamics in real time. However, the application of AI-enhanced solar tracking systems for marine PV installations remains limited, and their integration within complete hybrid shipboard energy systems has not been sufficiently explored.

In practical shipboard applications, solar PV systems must operate within a hybrid energy management framework to ensure reliability and power quality. Diesel generators remain essential during periods of low irradiance or high load demand, while battery energy storage systems support power smoothing and operational flexibility. Consequently, evaluating the techno-economic performance of hybrid diesel–PV–battery systems is critical for quantifying fuel savings, emission reductions, and overall system viability in marine environments.

This paper addresses these research gaps by proposing an AI-enhanced dual-axis solar tracking strategy designed to maximize DNI capture under dynamic marine roll, pitch, and yaw conditions and by integrating the proposed tracker within a hybrid diesel–PV–battery shipboard power system. A comprehensive MATLAB/Simulink model is developed and applied to a real ferry case study operating in the coastal region of Mombasa, Kenya. The main contributions of this work are summarized as follows:

- development of an AI-based solar tracking strategy capable of maintaining high irradiance efficiency under dynamic marine conditions;
- integration of the proposed tracking system within a hybrid diesel–PV–battery architecture for auxiliary power supply; and
- techno-economic assessment demonstrating significant reductions in diesel fuel consumption, operating costs, and carbon emissions.

2. Methodology

2.1 System Overview and Case Study Description

This study models a hybrid shipboard auxiliary power system integrating a solar photovoltaic (PV) array, a diesel generator, and a battery energy storage system (BESS). The system is evaluated for the MV Safari passenger ferry, operating along the coastal region of Mombasa, Kenya, where solar irradiance is favourable throughout the year. The vessel's daily auxiliary energy demand is approximately 432.5 kWh, representing passenger service systems, navigation and communication equipment, lighting, and essential onboard services. This case study reflects typical operational conditions of medium-sized passenger ferries in tropical marine environments, ensuring practical relevance while maintaining a fully simulated framework.

2.2 Load Profiling and Energy Demand

The auxiliary load inventory is summarized in Table 1. All loads are classified as essential, requiring uninterrupted supply—no load shedding is permitted. The total peak load is 41.925 kW.

Table 1: Auxiliary load inventory

S/No.	**Load Type**	**Quantity**	**Unit Power (kW)**	**Total Power (kW)**	**Runtime per Day (Hrs)**	**Daily Energy (kWh)**
1	Control RoomAC	1	1.5	1.5	12	18.0
2	Equipment Room AC	2	1.5	3.0	24	72.0
3	Water Pumps	3	7.45	22.35	2	44.7
4	Navigation Equipment	8	1.0	8	24	192.0
5	VHF Communication	3	0.025	0.075	24	1.8
6	Lighting	20	0.1	2.0	12	24
7	Miscellaneous Devices	5	1.0	5.0	16	80
Total				**41.925Kw**		**432.5kWh/Day**

2.3 Resource Assessment and Data Collection

Solar irradiance and meteorological data were obtained from the National Solar Radiation Database (NSRDB) for coordinates 04°04.7643" S, 039°39.9058" E. Key parameters included hourly DNI, GHI, temperature, solar zenith angle, and wind speed. Vessel motion data (roll, pitch, yaw) were simulated based on typical sea states for the region.

Load data from the ferry were collected and input into **HOMER Pro** for preliminary sizing and analysis. The load profiles were then integrated into the simulation framework to evaluate system performance, including **battery utilization, PV contribution, and diesel generator output**, under varying irradiance and vessel motion conditions. This process enabled assessment of the hybrid system's ability to meet continuous auxiliary power demand in a marine environment.

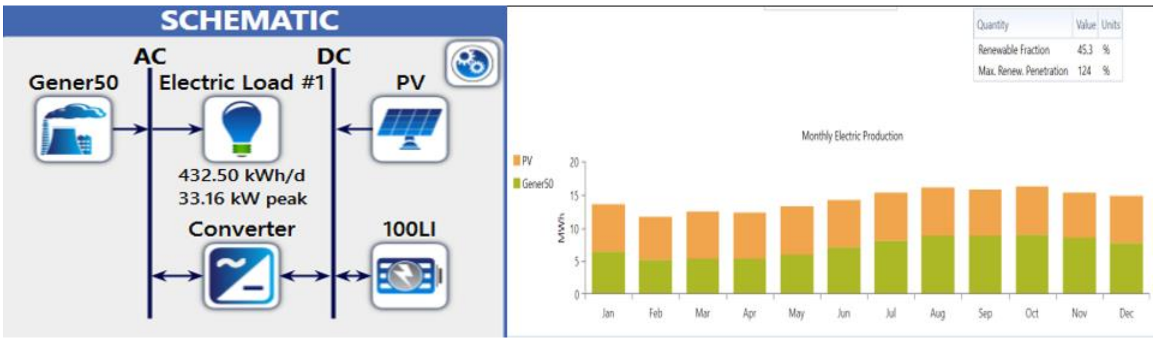

Figure 1 HOMER system design

2.4 Hybrid System Configuration

The system components were sized using HOMER Pro for preliminary techno-economic optimization. The final configuration includes:

- PV array: 20 kW (capped at 15 kW for inverter stability)
- Diesel generator: 50 kW
- Battery: Li-ion, SOC maintained between 70–77%
- Inverter: 50 kW grid-tied hyrid inverter

2.5 Marine PV System and Dual-Axis Gimbal Tracking Model

A 20 kW PV array is modelled in MATLAB/Simulink and virtually mounted on a dual-axis gimbal. The gimbal compensates for simulated vessel roll and pitch motions by adjusting tilt and azimuth angles, keeping the PV surface normal aligned with the incident solar radiation. Mechanical constraints are incorporated in the model, with tilt angles limited to ±90° and azimuth angles wrapped within 0°–360°.

The effective Direct Normal Irradiance (DNI) incident on the PV array is computed as a function of solar position, simulated vessel orientation, and gimbal angles, forming the basis for tracking performance evaluation.

2.6 AI-Based Solar Tracking Strategy

An **artificial neural network (ANN)** is developed to predict optimal PV tilt and azimuth angles under simulated marine conditions. The training done using python and then weights loaded to Matlab R2016. The ANN inputs include:

- Simulated vessel roll, pitch, and yaw angles
- Solar azimuth and elevation angles
- Simulated DNI values

The outputs are:

- Commanded tilt and azimuth angles to maximize DNI capture
- Predicted DNI for performance monitoring

2.7 Neural Network Architecture and Training

The ANN was developed in Python using a multi-layer feedforward architecture with the following structure:

- Input Layer: 6 neurons (roll, pitch, yaw, sun_az, sun_el, DNI)
- Hidden Layers: Fully connected layers with 64, 32, and 16 neurons, using ReLU activation and dropout for regularization
- Custom Interaction Layer: Multiplicative interaction between DNI and other features to capture nonlinear relationships
- Output Layer: 3 neurons (tilt, azimuth, predicted DNI)

2.8 Training Output and Model Performance

- Tilt Angle Prediction: $R^2 = 0.9968$, MAE = 1.24°
- Azimuth Angle Prediction: $R^2 = 0.9539$, MAE = 4.94°
- DNI Prediction: $R^2 = 1.0000$, MAE = 0.50 W/m²

The trained model and scaling parameters were exported to ai_solar_tracker.mat and ai_solar_tracker_net.mat for integration into MATLAB/Simulink.

Figure 2 model training process

- Tilt Angle (β): The model achieved near-perfect performance in predicting the tilt setpoint, with an R^2 value of 0.9968 and a mean absolute error (MAE) of just 1.24 degrees. This indicates the model has learned the underlying physics of vertical sun tracking with extremely high fidelity.
- Azimuth Angle (γ): Prediction of the azimuth setpoint is also excellent ($R^2 = 0.9539$), though with a slightly higher error (MAE = 4.94 degrees). This is expected, as azimuth correction can be more sensitive to rapid changes in vessel yaw and heading. The error remains well within acceptable limits for effective solar tracking.

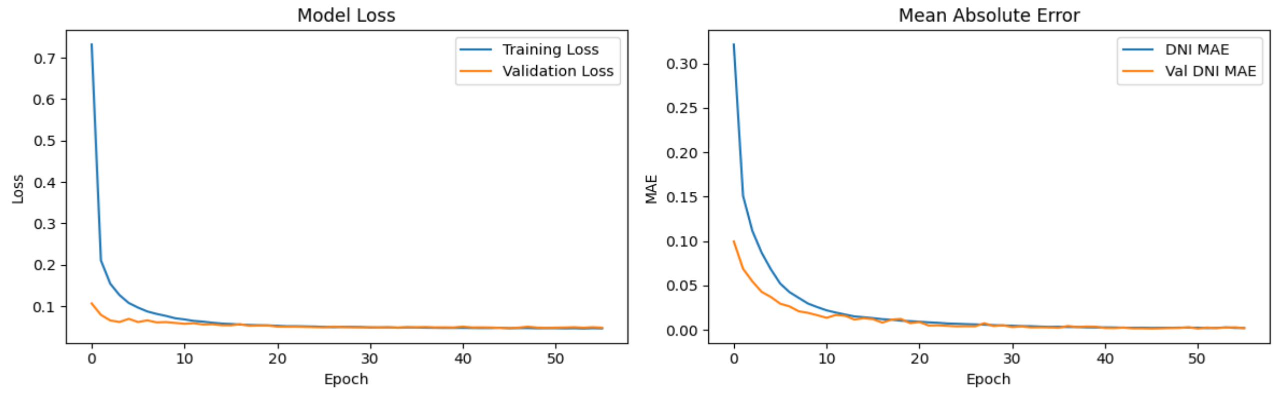

Figure 3 Model Loss and Mean Absolute Error plots

- Direct Normal Irradiance (DNI): The model's prediction of irradiance is outstanding, with an R^2 of 1.0000 and an MAE of 0.50 W/m². This near-perfect score is a direct result of the custom Interaction Layer, which allowed the model to learn the precise nonlinear relationship between vessel motion, sun position, and the resulting irradiance on the compensated panel surface. The plot of Predicted vs Input DNI (generated by the code) would show a tight clustering of points along the ideal line, visually confirming the accuracy quantified by the metrics.

- The accompanying Model Loss and Mean Absolute Error plots (from plot_training_history()) would show curves for training and validation that converge smoothly, indicating a stable training process without overfitting. The validation curves closely following the training curves confirm the model's strong ability to generalize to unseen data.

2.9 Gimbal Control System

The gimbal control system uses a PID controller with the following transfer functions:

For tilt control:

$$G_{tilt}(s) = \frac{0.58s^2 + 3.62s + 2.2}{s^3 + 4.48s^2 + 6.02s + 2.2}$$

For azimuth control:

$$G_{azimuth}(s) = \frac{0.09s^2 + 1.62s + 1.9}{s^3 + 3.99s^2 + 4.0s + 1.9}$$

2.10 DNI Compensation Model

A linear correction model was developed to quantify motion-induced DNI losses:

$$\text{Pred\_DNI} = \frac{Meas\_DNI}{1+k_r \cdot Roll + K_P \cdot Pitch + k_y \cdot Yaw + k_{sa} SunAz + k_{se} SunEl}$$

Where the coefficients obtained through regression are:

$k_r \approx 0.0003007$, $K_P \approx -0.0072618$, $k_y \approx -0.0008622$, $k_{sa} = 0.0004350$, $k_{se} = \mathbf{-0.0010841}$

This model enables the system to maintain approximately **90% effective irradiance** under moderate sea states (roll ±5°, pitch ±3°).

After training, the model, along with the feature (scaler_X) and target (scaler_y) scalers, was exported to ai_solar_tracker.mat. A warning during export (Scaler for target 'comp' not found) was safely handled by the code, defaulting to identity scaling for that parameter without affecting model performance. This file provides all necessary parameters for the Simulink model to preprocess inputs and postprocess outputs, enabling accurate real-time inference within the marine energy management system simulation.

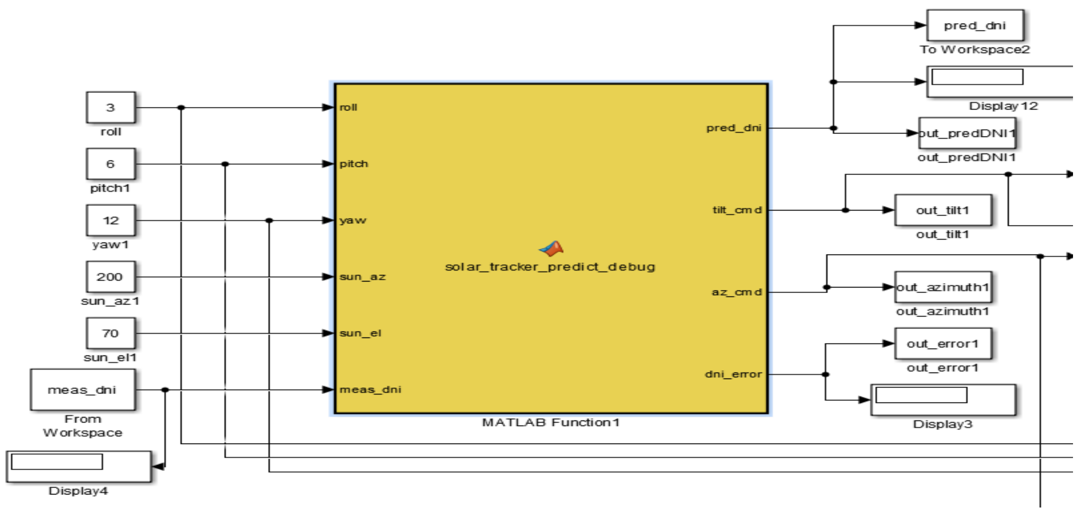

Figure 4 Simulink model of Dual-Axis Gimbal Tracking

2.11 Hybrid System Simulation in MATLAB/Simulink

The complete hybrid system was modelled in MATLAB/Simulink with the following components:

1. PV Array Model: 20 kW array with MPPT and DC-DC converter
2. Diesel Generator: 50 kW model with fuel consumption characteristics
3. Battery Bank: Li-ion BESS with SOC management (70–77% operating window)

4. AI-Based EMS: Rule-based controller with 6 operational modes:
   - Mode 0: PV only
   - Mode 1: PV + Battery
   - Mode 2: Battery only
   - Mode 3: Diesel only
   - Mode 4: PV + Diesel
   - Mode 5: Battery + Diesel

The EMS prioritizes renewable sources while ensuring uninterrupted power supply through seamless transitions between modes.

2.12 Simulation Setup and Performance Metrics

The system is simulated under varying **sea state conditions**, with bounded roll and pitch angles to reflect realistic vessel motion. Solar irradiance and environmental datasets are derived from the Mombasa coastal region. Simulation time steps are chosen to capture both **fast vessel dynamics** and **slower energy system responses**.

Key performance metrics include:

- Effective DNI capture
- PV energy yield
- Diesel fuel consumption
- CO_2 emissions
- Economic indicators such as annual fuel savings and payback period

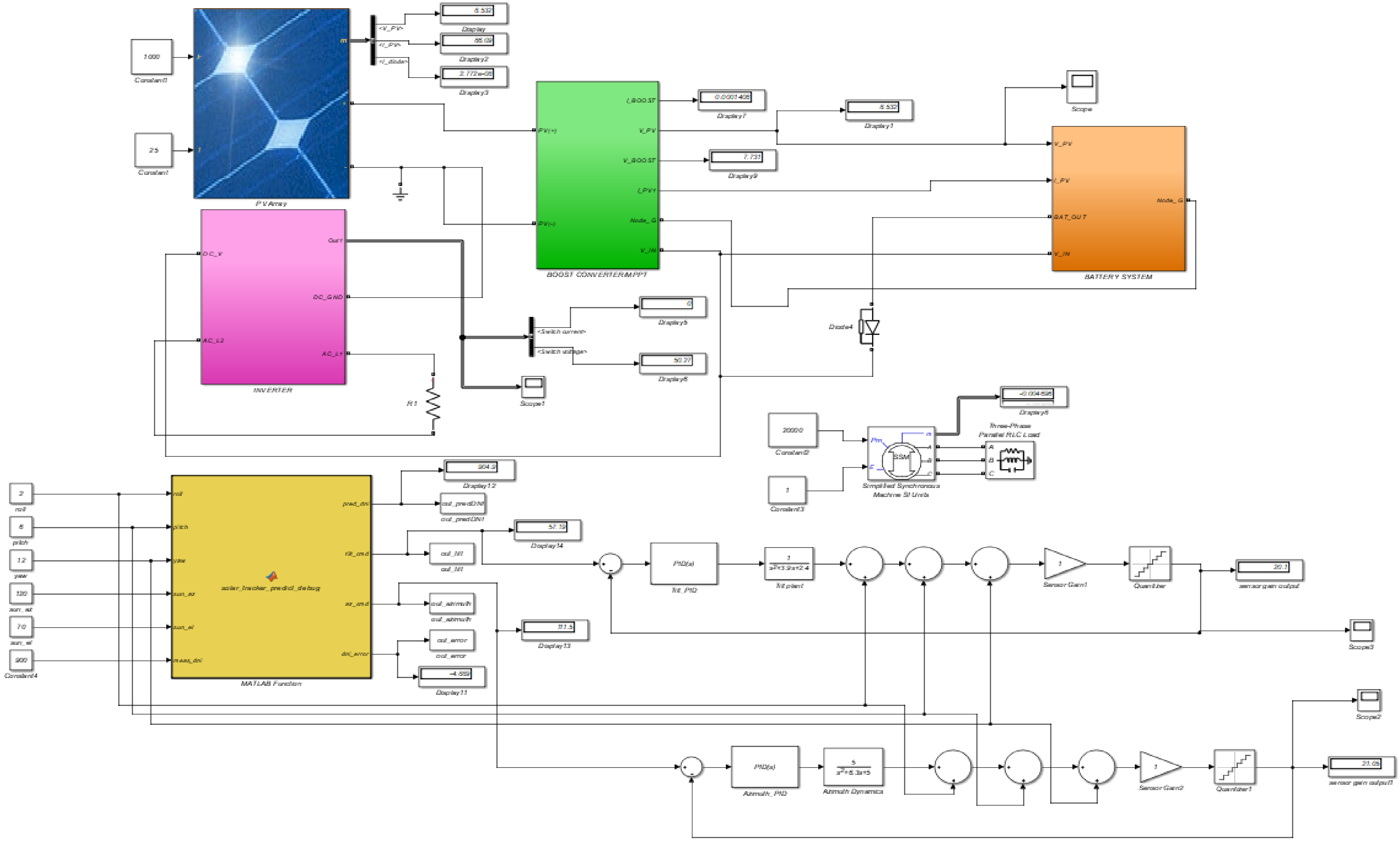

Figure 5 A complete hybrid power system

3. Results and Discussion

3.1. DNI Capture Optimization

The AI-driven gimbal system significantly improved DNI capture compared to a fixed-tilt configuration. Under moderate sea conditions (roll ±5°, pitch ±3°), the gimbal system maintained an average effective irradiance of 90% of available DNI, whereas the fixed-tilt system experienced drops to as low as 60%.

3.2. Energy Yield Enhancement

The gimbal-tracked system produced 3.6 kWh over a simulated period, compared to 3.1 kWh from the fixed-tilt system—an increase of approximately 17%. The predicted DNI formula derived from the AI model is given by:

$$\text{Pred\_DNI} = \frac{Meas\_DNI}{1+k_r \cdot Roll+K_P \cdot Pitch+k_y \cdot Yaw+k_{sa}SunAz+k_{se}SunEl}$$

$k_r \approx 0.0003007$, $K_P \approx -0.0072618$, $k_y \approx -0.0008622$, $k_{sa} = 0.0004350$, $k_{se} = -0.0010841$

The AI-driven gimbal system significantly enhanced energy harvest. Compared to an equivalent fixed-tilt array, the tracking system increased energy yield by approximately 17%. The fixed-tilt system produced an estimated 3.1 kWh, while the gimbal system produced 3.6 kWh over the same period. This increase is directly attributable to maintaining a near-optimal incidence angle throughout the day and compensating for vessel motion.

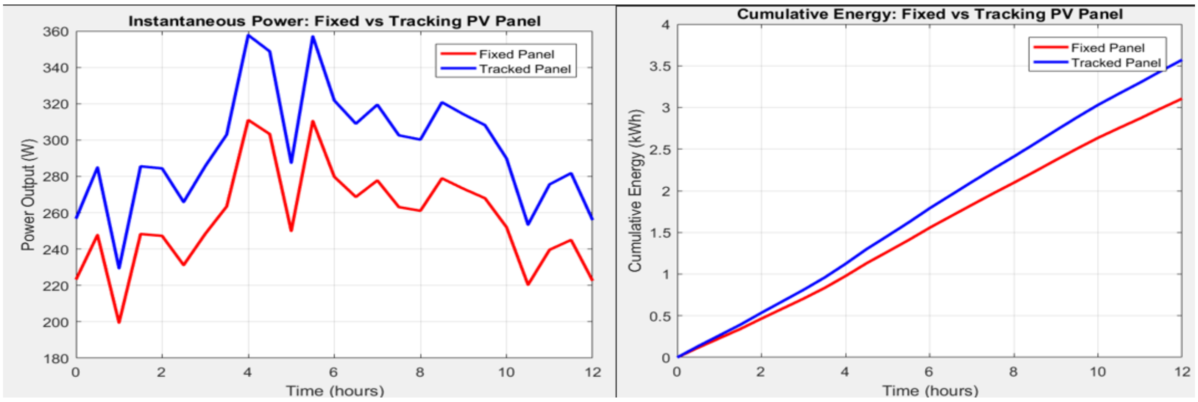

Figure 6 AI gimbal DNI tracking system improves energy capture by 17%

3.3. Hybrid System Performance

The hybrid energy system successfully met 100% of the auxiliary load demand, which amounts to 432.5 kWh per day of this total energy requirement, approximately 57.66% was supplied by the solar PV system, while the diesel generator provided the remaining 42.34%. By integrating solar PV into the energy mix, the operation of the diesel generator was significantly reduced, with its runtime decreasing from 24 hours to roughly 10.16 hours per day.

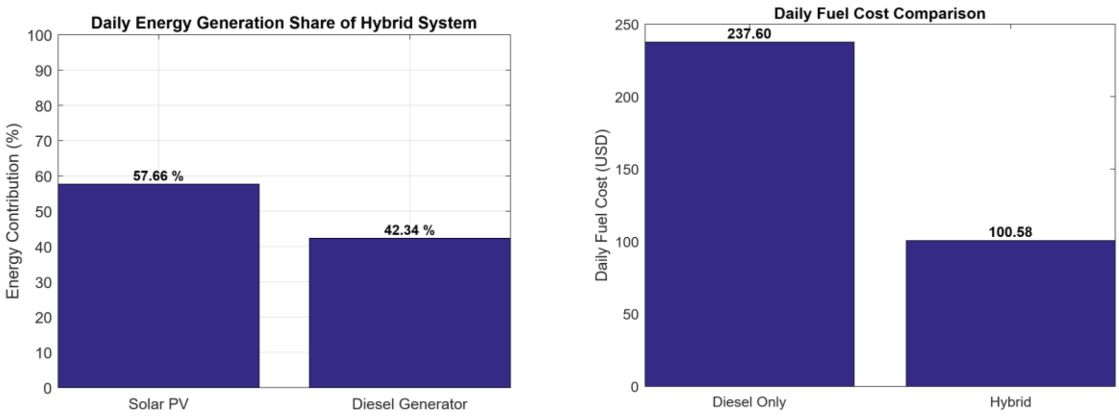

Figure 7 Daily energy generation share of the hybrid system and daily fuel cost comparison

This reduction in generator usage resulted in substantial operational benefits, including estimated annual fuel savings of USD 50,012.30 and a corresponding decrease in CO_2 emissions by 101.5 tonnes, highlighting both economic and environmental advantages of the hybrid system.

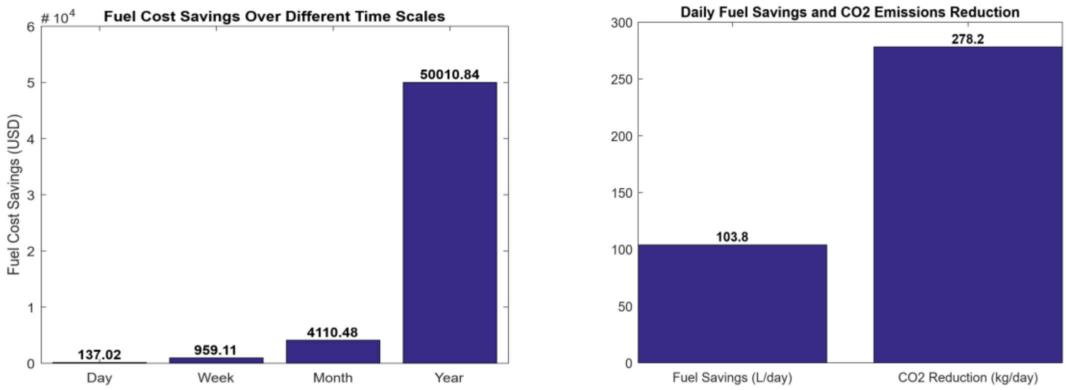

Figure 8 Fuel cost savings and CO2 Emissions Reduction

If the capital cost (PV, batteries, inverter, EMS, and gimbal system) is assumed at, say, USD 200,000, then:

$$\text{ROI} = \text{Annual savings} / \text{CAPEX} = 50{,}012.30 / 200{,}000 \approx 25.0\%$$

An annual ROI of approximately 25% demonstrates strong economic viability of the proposed hybrid system. This value exceeds typical returns reported for marine and industrial hybrid energy systems, particularly considering that the analysis accounts only for direct fuel cost savings and excludes secondary economic benefits such as reduced maintenance costs and extended generator lifespan.

Simple Payback Period = 200,000 ÷ 50,012.30 ≈ 4 years

This indicates strong economic viability for the proposed hybrid system.

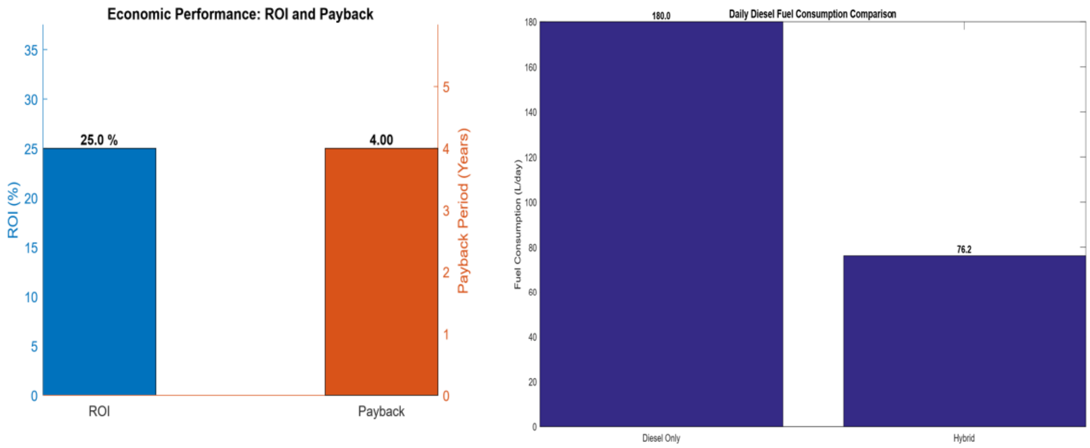

Figure 9 Economic performance and daily fuel consumption comparison

4. Conclusions

This study successfully developed and simulated an AI-enhanced hybrid solar-diesel power system for marine auxiliary loads, with a focus on maximizing DNI capture under dynamic vessel motion. The key contributions are:

1. **AI-Based Solar Tracking:** A dual-axis gimbal system driven by a neural network predictor achieved high accuracy in tilt and azimuth correction ($R^2 > 0.95$), maintaining 90% effective irradiance under moderate sea states.
2. **Enhanced Energy Yield:** The gimbal-tracked PV system increased energy capture by 17% compared to a fixed-tilt configuration, demonstrating the critical role of motion compensation in marine PV applications.
3. **Economic and Environmental Viability:** The system achieved significant annual fuel savings (USD 50,012.3) and CO_2 reductions (101.5 tonnes), with a projected payback period of 4 years, confirming its techno-economic feasibility.
4. **Marine-Specific Modelling:** The developed DNI compensation model and gimbal control framework provide a replicable approach for optimizing solar energy utilization in marine environments, addressing a critical gap in existing maritime renewable energy studies.

Future work should focus on real-world pilot implementation, integration with propulsion systems, and the application of advanced AI techniques such as reinforcement learning for further optimization of energy management in dynamic marine conditions.

References

Aboelezz, A. M., Sedhom, B. E., El-Saadawi, M. M., Eladl, A. A., & Siano, P. (2023). State-of-the-Art Review on Shipboard Microgrids: Architecture, Control, Management, Protection, and Future Perspectives. *Smart Cities*, *6*(3), 1435–1484. https://doi.org/10.3390/smartcities6030069

Animah, I., Adjei, P., & Djamesi, E. K. (2023). Techno-economic feasibility assessment model for integrating hybrid renewable energy systems into power systems of existing ships: A case study of a patrol boat. *Journal of Marine Engineering \& Technology*, *22*(1), 22–37. https://doi.org/10.1080/20464177.2022.2087272

Antonopoulos, S., Visser, K., Kalikatzarakis, M., & Reppa, V. (2021). MPC framework for the energy management of hybrid ships with an energy storage system. *Journal of Marine Science and Engineering*, *9*(9). https://doi.org/10.3390/jmse9090993

Aziz, A. S., Tajuddin, M. F. N., Adzman, M. R., Ramli, M. A. M., & Mekhilef, S. (2019). Energy management and optimization of a PV/diesel/battery hybrid energy system using a combined dispatch strategy. *Sustainability (Switzerland)*, *11*(3). https://doi.org/10.3390/su11030683

Azman, N., & Sulistiawan, R. (2024). Design and performance evaluation of an off-grid hybrid solar system in a remote location: A case study of Legundi Island. *MethodsX*, *12*, 102716. https://doi.org/10.1016/j.mex.2024.102716

Bacalja Bašić, B., Krčum, M., & Gudelj, A. (2023). Adaptation of Existing Vessels in Accordance with Decarbonization Requirements—Case Study—Mediterranean Port. *Journal of Marine Science and Engineering*, *11*(8). https://doi.org/10.3390/jmse11081633

Banaei, M., Ghanami, F., Rafiei, M., Boudjadar, J., & Khooban, M. H. (2020). Energy management of hybrid diesel/battery ships in multidisciplinary emission policy areas. *Energies*, *13*(6), 1–16. https://doi.org/10.3390/en13164179

Bui, T. M. N., Dinh, T. Q., Marco, J., & Watts, C. (2018). An Energy Management Strategy for DC Hybrid Electric Propulsion System of Marine Vessels. *2018 5th International Conference on Control, Decision and Information Technologies, CoDIT 2018*, 80–85. https://doi.org/10.1109/CoDIT.2018.8394785

Cheng, P., Liang, N., Li, R., Lan, H., & Cheng, Q. (2019). Analysis of influence of ship roll on ship power system with renewable energy. *Energies*, *13*(1). https://doi.org/10.3390/en13010001

Costa, T. S., & Villalva, M. G. (2020). Technical evaluation of a PV-diesel hybrid system with energy storage: Case study in the Tapajós-Arapiuns Extractive Reserve, Amazon, Brazil. *Energies*, *13*(11). https://doi.org/10.3390/en13112969

Diab, F., Lan, H., & Ali, S. (2016a). Novel comparison study between the hybrid renewable energy systems on land and on ship. *Renewable and Sustainable Energy Reviews*, *63*, 452–463. https://doi.org/10.1016/j.rser.2016.05.053

Diab, F., Lan, H., & Ali, S. (2016b). Novel comparison study between the hybrid renewable energy systems on land and on ship. *Renewable and Sustainable Energy Reviews*, *63*, 452–463. https://doi.org/10.1016/j.rser.2016.05.053

Ge, Y., Zhang, J., Zhou, K., Zhu, J., & Wang, Y. (2023). Research on Energy Management for Ship Hybrid Power System Based on Adaptive Equivalent Consumption Minimization Strategy. *Journal of Marine Science and Engineering*, *11*(7). https://doi.org/10.3390/jmse11071271

Ghenai, C., Bettayeb, M., Brdjanin, B., & Hamid, A. K. (2019). Hybrid solar PV/PEM fuel Cell/Diesel Generator power system for cruise ship: A case study in Stockholm, Sweden. *Case Studies in Thermal Engineering*, *14*(June), 100497. https://doi.org/10.1016/j.csite.2019.100497

Guo, X., Tang, D., Yuan, Y., Yuan, C., Shen, B., & Guerrero, J. M. (2025). A New Energy Management Strategy Supported by Reinforcement Learning: A Case Study of a Multi-Energy Cruise Ship. *Journal of Marine Science and Engineering*, *13*(4). https://doi.org/10.3390/jmse13040720

Kolodziejski, M., & Michalska-Pozoga, I. (2023). Battery Energy Storage Systems in Ships' Hybrid/Electric Propulsion Systems. *Energies*, *16*(3). https://doi.org/10.3390/en16031122

Lan, H., Bai, Y., Wen, S., Yu, D. C., Hong, Y. Y., Dai, J., & Cheng, P. (2016). Modeling and stability analysis of hybrid PV/Diesel/ESS in ship power system. *Inventions*, *1*(1), 1–16. https://doi.org/10.3390/inventions1010005

Mohamed, R. G., Hassan, A. A., & Abdel Aleem, S. H. E. (2025). A modified energy management strategy for PV/diesel hybrid system to reduce diesel consumption based on artificial protozoa optimizer. *Scientific Reports*, *15*(1), 4440. https://doi.org/10.1038/s41598-025-87716-y

Nivolianiti, E., Karnavas, Y. L., & Charpentier, J. F. (2024). Fuzzy Logic-Based Energy Management Strategy for Hybrid Fuel Cell Electric Ship Power and Propulsion System. *Journal of Marine Science and Engineering*, *12*(10). https://doi.org/10.3390/jmse12101813

Peng, X., Chen, H., & Guan, C. (2023). Energy Management Optimization of Fuel Cell Hybrid Ship Based on Particle Swarm Optimization Algorithm. *Energies*, *16*(3). https://doi.org/10.3390/en16031373

Petrychenko, O., Levinskyi, M., Goolak, S., & Lukoševičius, V. (2025). Prospects of Solar Energy in the Context of Greening Maritime Transport. *Sustainability (Switzerland)*, *17*(5). https://doi.org/10.3390/su17052141

Radica, G., Vidović, T., Šimunović, J., & Jurić, Z. (2025). Overview of Hybrid Marine Energy System Configurations and System Component Modeling Approaches. *Energies*, *18*(5), 1–24. https://doi.org/10.3390/en18051189

Riayatsyah, T. M. I., Geumpana, T. A., Fattah, I. M. R., & Mahlia, T. M. I. (2022). Techno-Economic Analysis of Hybrid Diesel Generators and Renewable Energy for a Remote Island in the Indian Ocean Using HOMER Pro. *Sustainability (Switzerland)*, *14*(16). https://doi.org/10.3390/su14169846

Roslan, S. B., Konovessis, D., & Tay, Z. Y. (2022). Sustainable Hybrid Marine Power Systems for Power Management Optimisation: A Review. In *Energies* (Vol. 15, Issue 24). https://doi.org/10.3390/en15249622

Somera, J. D. C., Parado, S. P. E., Castro, M. T., & Ocon, J. D. (2021). Techno-economics of Hybrid System Electrification of Roll-on/Roll-off Vessels in the Philippines. *Chemical Engineering Transactions*, *88*(August), 559–564. https://doi.org/10.3303/CET2188093

Tural, B., & Akar, O. (2025). Design and Economic Analysis of Marine Vessel PV Power System Based on Solar Radiation Estimation. *IEEE Access*, *PP*, 1. https://doi.org/10.1109/ACCESS.2025.3571875

Ünlübayir, C., Mierendorff, U. H., Börner, M. F., Quade, K. L., Blömeke, A., Ringbeck, F., & Sauer, D. U. (2023). A Data-Driven Approach to Ship Energy Management: Incorporating Automated Tracking System Data and Weather Information. *Journal of Marine Science and Engineering*, *11*(12). https://doi.org/10.3390/jmse11122259

Vieira, G. T. T., Pereira, D. F., Taheri, S. I., Khan, K. S., Salles, M. B. C., Guerrero, J. M., & Carmo, B. S. (2022). Optimized Configuration of Diesel Engine-Fuel Cell-Battery Hybrid Power Systems in a Platform Supply Vessel to Reduce CO2 Emissions. *Energies*, *15*(6), 1–34. https://doi.org/10.3390/en15062184

Yuan, Y., Wang, J., Yan, X., Li, Q., & Long, T. (2018a). A design and experimental investigation of a large-scale solar energy/diesel generator powered hybrid ship. *Energy*, *165*, 965–978. https://doi.org/10.1016/J.ENERGY.2018.09.085

Yuan, Y., Wang, J., Yan, X., Li, Q., & Long, T. (2018b). A design and experimental investigation of a large-scale solar energy/diesel generator powered hybrid ship. *Energy*, *165*. https://doi.org/10.1016/j.energy.2018.09.085

Yuan, Y., Wang, J., Yan, X., Shen, B., & Long, T. (2020). A review of multi-energy hybrid power system for ships. *Renewable and Sustainable Energy Reviews*, *132*, 110081. https://doi.org/10.1016/j.rser.2020.110081

Performance of Expansive Clay Soil Modified With Pulverized Ceramic Waste and an Alkali Activator for Construction

E.C. Kimaiyo*, B. Odero, T. Mungathia

Jomo Kenyatta University of Agriculture and Technology

Corresponding Author Email: kimaiyoeleanor@gmail.com

Abstract

Expansive clay soil poses a significant challenge to geotechnical engineers due to its excessive volume changes when exposed to varying moisture conditions. Construction of foundations and subgrades on expansive clay soils requires modification of the soil using appropriate methods to improve its geotechnical properties. The objective of this research is to investigate the effects on expansive clay soil after modification with pulverized ceramic waste and an alkali activator. Specifically, to determine the material properties, to determine consistency and swell of modified soil, to determine the strength of modified soil, and lastly to develop strength predictive models following the behaviour of modified Expansive clay soil. The research involved conducting chemical tests such as X-ray fluorescence analysis; physical tests such as Atterberg limits, and mechanical tests such as California Bearing Ratio, Unconfined Compressive Strength, and Compaction. Predictive modelling for expansive clay soil modified with pulverized ceramic waste and an alkali activator will also be developed. The results indicated That both CW and CKD significantly improved the soil's engineering properties. CW was particularly effective in reducing swell potential, achieving nearly a 90% reduction at higher replacement levels, while CKD produced substantial improvements in strength parameters such as California Bearing Ratio (CBR) and Unconfined Compressive Strength (UCS) even at lower percentages. The combined use of CW and CKD demonstrated the best overall performance, producing the lowest swell potential and the highest strength values due to synergistic pozzolanic reactions and formation of cementitious compounds. Predictive models developed through regression analysis showed strong correlations between stabilizer content and soil performance, enabling reliable estimation of swell reduction and strength improvement. Overall, the findings confirm that the combined use of ceramic waste and cement kiln dust provides an effective, sustainable solution for stabilizing expansive clay soils for construction applications while simultaneously promoting environmentally responsible utilization of industrial and construction waste materials.

Keywords: Expansive clay soil, Pulverized Ceramic Waste, Cement Kiln Dust, Swell, California Bearing Ratio (CBR), Unconfined Compressive Strength (UCS), Atterberg limits.

1. Introduction

In geotechnical engineering, several types of soils exist with different classifications and categorizations. Some of these soils can be used in the form they exist but others, categorized as problematic are not suitable for use before any modifications are done. Expansive clay soils are considered problematic and present significant challenges in geotechnical and structural engineering globally. The costs associated with the expansive behavior of these soils are estimated to reach several billion dollars each year. (Lee et.al 2012)

A well-known Expansive clay soil is the Black Cotton Soil (BCS). The problematic nature of BCS is due to the performance of their clay minerals which exhibit shrink-swell characteristics. The shrink-swell behaviour renders expansive clay soils inadequate for direct engineering application without any alterations. (Chijioke et.al 2019). The clay minerals present in BCS include montmorillonite, illites, and kaolinites with the montmorillonite group largely responsible for the shrink-swell tendencies. (Sangita et.al 2013). BCS is known to exhibit properties such as extreme changes in volume due to shrink-swell phenomena, high plasticity, low permeability, high compressibility, and low strength. (Vijayan et.al 2020)

In recent years, geotechnical engineers around the world have increasingly favoured environmentally friendly and sustainable techniques for enhancing the engineering properties of expansive clay soils. Soil stabilization is of critical concern to any construction that is to take place in an area extensively covered by BCS. Stabilization of the BCS is necessary to improve the soil's geotechnical properties, making it suitable for the construction of foundations and pavements. Stabilization can be achieved through mechanical, thermal, or chemical means as stated (Kaushal et.al 2015). The utilization of agricultural waste and industrial by-products in the stabilization of expansive clay soils not only improves their engineering properties but also contributes to reducing the negative environmental impacts associated with conventional stabilization methods. (Sivabalaselvamani et.al 2022)

Chemical stabilization of expansive clay soils involves adding pozzolanic admixtures that enhance soil bonding and give it cement-like properties. (Pankaj et.al 2012). Ceramics refer to inorganic materials created from non-metallic chemicals and fired; they may also contain organic substances. They are known to contain high quantities of silicon dioxide followed by aluminium oxide and other metallic oxides such as calcium oxide and iron oxide present in small amounts. The high content of silica and alumina enable the material to exhibit pozzolanic attributes. (Sharma et.al 2020). Ceramics include floor and wall tiles, sanitary ware, and home ceramics. High quantities of ceramic waste are generated from construction and demolition waste (C&DW), which accounts for 30% of solid waste globally, of which 35% of the C&DW is dumped in landfills annually. (Callun et.al 2022). Some ceramic waste can result out of the manufacturing process of ceramic products.

Pulverization is the process of mechanically crushing a material to reduce it to powder or soft mass. Additionally, the process of pulverization can be done to different levels depending on the method, machine used, and purpose of pulverization i.e. industrial/pharmaceutical among others. According to (Iknur et.al 2016) the level of pulverization plays a key role in achieving improved engineering properties in high plasticity clay soil stabilization. Fine pulverization results in significantly higher strength values as compared to coarse pulverization especially for cement treated high plasticity clay soils. (Iknur et.al 2016).

Pozzolanic materials are defined as silica-aluminous substances that have little or no cementitious value on their own. However, when finely divided and combined with moisture, they can chemically react with calcium hydroxide at normal temperatures to produce compounds that do exhibit cementitious properties (Abdullah et al., 2012). The alkali-activator reaction can be triggered using a waste by-product from cement production known as cement kiln dust. This dust contains high levels of calcium oxide, which, when exposed to moisture, reacts to form calcium hydroxide. This calcium hydroxide is essential for initiating the pozzolanic reaction. (Mohammadinia et al., 2018). This study, therefore, seeks to determine the performance of expansive clay soil treated with pulverized ceramic waste and an alkali activator for use in construction.

Expansive clay soil is widely recognized for its challenging geotechnical characteristics impacting the stability of construction projects. (Beyene et.al 2022) (Saber et.al 2022). These soils undergo unpredictable volume changes when exposed to varying moisture contents leading to excessive swelling and shrinkage of the soil. The poor workability and load-bearing capacity of expansive clay soils make them unsuitable for use as pavement subgrade, foundation soil for buildings, or underground utilities and piping without appropriate modification. Several structures constructed on expansive clay soil have been subjected to significant damage due to the differential heave caused by moisture changes in the expansive clay soil. (Sudhakar et.al 2021). In regions with expansive soil coverage, damages on the roads and low-rise buildings are prevalent, it is expected that much of these damages are caused by the excessive volume change of the black cotton soil. This very important factor should be addressed in both design and construction of the pavement and underground utility networks, and light structures to avoid the said damages. (Chijioke et.al 2019)

There is also the high cost attached to maintenance and repairs of structures and pavement damages due to the shortened design life of infrastructure constructed on expansive clay soil. Damages on structures or pavement subgrades could result in accidents which could lead to the loss of life or impairment of persons involved. Current industry practice entails the improvement of expansive clay soil properties using stabilizing agents with a growing interest in sustainable stabilizing agents. (Zimar et.al 2022).

Moreover, construction demolition waste, mainly ceramic waste and industrial by-product-Cement Kiln Dust (CKD) is hazardous to the environment as pollution is a key concern to environmentalists and the public as well. Ceramic waste materials, which include ceramic tiles and other ceramic products, contribute the highest content of wastes in the Construction and Demolition Wastes (C&DW). Globally about 35% of Construction Demolition Waste is dumped in landfills annually. (Menegaki et al. 2018). Ceramic tile production has surged globally, with Turkey leading in Europe and China as the top producer worldwide. Annually, about 250,000 tons of tiles are discarded, while around 100 million are used for repairs (Topcu & Canbaz, 2007). Unfortunately, ceramic waste is typically sent to landfills due to a lack of recycling practices, standards, and knowledge on its effective use. (Pacheco-Torgal & Jalali, 2010).

Furthermore, it is estimated that approximately 30 million tonnes of CKD is generated worldwide each year, and approximately 80% remains stockpiled or landfilled which poses an environmental problem. (Hossain et.al 2011) Therefore, it is an area that if addressed would ease the pollution of the environment. The alternative of cut and fill to replace expansive clay soil has proven to be costly and is a growing concern to Sustainability Experts due to the depletion of existing resources. (Balaguera et al. 2018)

2. Methodology

2.1. Material Sourcing and Preparation

Expansive Clay Soil

The Expansive clay soil needed for the study was obtained from Konza area of Machakos County, approximately 60 kilometres Southeast of Nairobi, Kenya. Soil was collected from multiple locations within the Konza area. This area was selected because it has expansive clay soils that often exhibit poor load-bearing capacity and significant swelling when exposed to moisture, and being an area that is hosting the Konza City Technopolis, a study of this nature is required (Gateri & Esho, 2013). Given the scope of this study, samples were taken at different depths ranging from 1 metre to 3 metres to capture a representative cross-section of the soil strata (Guetterman, 2020). The sample was determined based on the standard geotechnical testing procedures. These procedures ensure that an adequate amount of the clay soil is collected to aid in all the stages of the laboratory testing.

Ceramic Waste

Ceramic waste was sourced from construction demolition waste. For most areas where demolitions are occurring, ceramic tiles and ceramic sanitary ware can be found lying around in the demolition debris. Once ceramic waste was collected from such debris, it was taken to the laboratory where it was broken into finer pieces and, thereafter, ground by friction using a bow mill machine to achieve the required pulverization level. The pulverized ceramic waste will be added to the clay soil at 5%,10%, 15%, 20%, and 25% percentage ratios to achieve clay soil modification. Thereafter, an optimum ratio of CW at 25% was also used to modify the soil.

Cement Kiln Dust

Cement kiln dust is produced during the manufacture of cement and is a co-product. For this study, it was sourced from Bamburi Cement manufacturers in Athi River, Machakos County. Cement kiln dust was used as the alkali activator required for the pozzolanic reaction that will enhance the clay soil modification. It was added to the clay soil at 5%,10%, and 15% percentage ratios to achieve this. Thereafter, an optimum ratio of CW at 15% was also used to modify the soil.

Water

Water used in the tests was portable water of good quality and free from impurities such as acid, suspended solids, or organic matter. These impurities could alter soil chemistry. The water was used in the different tests as required.

2.2. Material Characterization

Moisture Content

This refers to the amount of water that can be extracted from the soil by heating it to 105°C, expressed as a percentage of the dry mass. The methodology used to determine the moisture content of the sample was oven drying. When presented as a percentage, the relationship between the mass of water and dry soil indicates the moisture content. Moisture content is also valuable for assessing the plasticity and shrinkage limits of fine-grained soils. This analysis was conducted following BS 1377-2.

Particle Size Distribution

In this process, a granular material is allowed to pass through a predetermined sequence of sieve sizes to access the particle size distribution. The particle size distribution was done in accordance with BS1377 Part 2:1990, by wet sieving and sedimentation by the hydrometer analysis. In accordance with this standard, combined sieving and sedimentation procedures enable a continuous particle size distribution curve to be plotted from the size of the coarsest particles down to the clay size. Wet sieving which is applicable to cohesion-less soils, was done by passing an oven dried sample of soil through a nest of sieves in descending order. The hydrometer analysis was done on material passing the 63 microns sieve, to determine the the proportions of sand, silt and clay.

The results of the wet sieving and the hydrometer analysis were combined and plotted on a semi-logarithmic scale of the percentage of material passing each sieve against the sieve sizes to give the grading properties from which the coefficient of uniformity, Cu and coefficient of curvature Cc were determined as shown in Equations 3.1 and 3.2 (Knappet & Craig, 2012: O'Flaherty, 2002):

$Cu=D60/D10$

$Cc= D302/D10xD60$

Where

D10 is the particle diameter at which 10% by mass is finer

D30 is the particle diameter at which 30% by mass is finer

D60 is the particle diameter at which 60% by mass is finer

Specific Gravity

Specific gravity is the ratio of soil density to the ratio of water. It is used to ascertain various soil properties soil density, void ratio, and saturation. Higher Specific Gravity values translate to having higher strength and vice versa for lower specific gravity. It was conducted on the expansive clay soil following BS 812-2:1995.

Masses of the density bottle (m1), density bottle and dry soil (m2), the bottle, soil and water (m3) and the bottle full of water (m4) were taken and the specific gravity was computed from the following equation

$Gs= m2-m1/(m4-m1)-(m3-m2)$

Atterberg Limits for untreated expansive soil

The plastic limit of soil indicates the lowest moisture content at which the soil retains its plastic characteristics. The plasticity index refers to the range of moisture content, expressed as a percentage of the mass of the oven-dried soil, within which the material remains in a plastic state. This index was determined by calculating the numerical difference between the liquid limit and the plastic limit of the soil. The liquid limit is the moisture content at which the soil transitions from a plastic to a liquid state. Measurements were taken before modification, on neat expansive soil following BS 1377-2. The breakdown and calculations are as shown in section 4.2.3

Free Swell Index for untreated expansive soil

The swell test was carried out to measure the expansion of the clay when it was exposed to moisture. The swelling behaviour is particularly important for expansive clay soils like those found in Konza, as excessive swelling can cause structural damage to roads and foundations. Free swell index was determined for the neat expansive soil. The breakdown and calculations are as shown in section 4.2.4

X-ray Fluorescence

The X-ray Fluorescence XRF method was used to determine the elements present in the expansive soil sample before and after treatment. This method was important as it contributed to investigating the chemical structural changes that occurred after the expansive soil had been modified. The neat and treated samples were subjected to the test to observe the changes brought about by the modifications to the clay soil. (Beare-Rogers et al., 2016). The tests were conducted at the Material Testing and Research Department (MTRD) laboratory for the Ministry of Transport and Infrastructure using a handheld XRF Analyzer- sample Running Procedure (Burker version)

The samples were uniformly pulverized for analysis in air mode, they were put in the XRF sample cup, and a thin film was used to cover. The analysis face (film face) was put face down on the sample chamber. The sample window was then aligned with the "Detector HT" being selected. Analysis was then started from the trigger. After analysis, the results were viewed on the "Analysis window," which displays the detected spectrum name resulting from the qualitative analysis. The "Result Display" window displays both qualitative and quantitative results. Longer test durations of up to 60 seconds were applied to ensure the accuracy of results.

X-ray Diffraction Analysis

This experimental method will be used to determine the mineral phases present in the soil, particularly clay minerals such as montmorillonite, kaolinite, and illite, which are known to influence swelling behaviour (Beare-Rogers et al., 2016). The treated and neat samples will undergo this test to determine the changes in the mineral phase due to the soil modification. This was carried out at the laboratory for the State Department of Mining using the XRD D6 Phaser.

The samples were delivered to the lab in uniformly pulverized form for analysis and loaded into the sample holder, ensuring the surface was flat and smooth. The sample was then loaded into the holder in the goniometer stage, and the chamber door was securely locked. Thereafter, the software was set up to scan the parameters and set to start the scan after all was counterchecked. To ensure accurate data was obtained, air gaps were avoided, thick samples were avoided, and uneven surfaces were avoided.

2.3. Modification of clay soil

Steps and Procedures

After the clay soil samples arrived at the laboratory, they were subdivided through the quartering method and prepared for testing. First, the samples were air dried at room temperature, which is essential to remove any excess moisture without altering the chemical constitution of the clay soil. Secondly, the soil samples were crushed and pulverized, then passed through sieves to remove any organic matter and large particles to essentially leave only fine clay particles. This process ensured that there was uniformity in the samples. Basic material properties of the soil were then determined according to the steps outlined in the various standards for testing. This included particle size distribution, moisture content, Atterberg limits, and specific gravity.

After that, the clay soil was modified by the addition of pulverized ceramic waste and an alkali activator-cement kiln dust. Percentage replacement by weight was done at 5%,10%, 15%, 20% and 25% for pulverized ceramic waste and 5%,10% and 15% cement kiln dust. Each additive was then mixed thoroughly to ensure even distribution in the soil matrix. Thereafter, an optimum mix obtained from the individual modification resulted in another sample with 25% CW and 15% CKD as the optimum combined percentage for testing. Samples were then moulded according to the test requirements. Some tests required curing of the samples for 7 days and 28 days. Tests to determine the strength of the modified soil samples were done.

For the fourth objective, modelling using regression analysis, after samples had been prepared, they underwent initial testing of CBR and swell properties in their natural state. A second batch was then modified and retested for the CBR and swell characteristics. For regression analysis, the additives that were used to modify the soil in addition to pulverized ceramic waste (5,10,15,20,25,30%) were alkali activator-cement kiln dust (5,10,15%). Each additive was mixed thoroughly to ensure even distribution and then cured for 7,14 and 28 days to allow for chemical reactions to take place. (Du Hayashi et al. 2020).

Experimental Setup and Instrumentation.

All materials were sourced to meet quality and quantity objectives for the study. Test samples were guided by the test standards and procedures that were followed. For CBR, a dial gauge was placed on the compacted sample in a mould, the original reading taken and the material soaked for 4 days. After 4 days soak, the final dial reading was taken, and force-penetration measurements were taken for both upper and lower ends of the sample. Cylindrical samples had an average diameter of 50mm and a height of 100mm before testing the UCS. These were then subjected to an axial load which increased at a rate of 1mm per minute until failure occurred. The apparatus used was from the university’s transportation engineering lab.

2.4. Consistency and Swell of Modified Clay Soil

Atterberg Limit

The plastic limit of soil indicates the lowest moisture content at which the soil retains its plastic characteristics. The plasticity index refers to the range of moisture content, expressed as a percentage of the mass of the oven-dried soil, within which the material remains in a plastic state. This index was determined by calculating the numerical difference between the liquid limit and the plastic limit of the soil. The liquid limit is the moisture content at which the soil transitions from a plastic to a liquid state. Measurements were taken after modification, following BS 1377-2.

i) Liquid limit (W_L)

The test was carried out on a sample of soil passing the 425 µm sieve, which was mixed with distilled water and made into a homogeneous paste. The mixed soil was then placed into a metallic cylindrical plasticity index cup, which was then placed on the cone penetrometer apparatus as shown in figure 3-4 below. Cone penetrations were made into the soil sample (Plate 3.2) for 5 seconds and the soil moisture content for each penetration was taken in the penetration range of 15 to 25 mm. The liquid limit was determined as the moisture content for a 20 mm penetration from a plot of the moisture content against the cone penetration. This was conducted on neat expansive clay soil, with percentage replacements of 5%, 10%, 15%, 20%, 25%, and 30% for Ceramic Waste and 5%, 10%, and 15% for Cement Kiln Dust. The optimum percentage adopted was 25% CW and 15% CKD.

ii) Plastic Limit (Wp)

The plastic limit test (Wp) was carried out on the paste from the liquid limit test. The material was plastic enough to be shaped into a ball. The ball was moulded and rolled until a 3 mm thread sheared longitudinally and transversely. Samples were then taken for moisture content determination.

iii) Plasticity Index (Ip)

The plasticity index (Ip) is the difference between the liquid limit and the plastic limit (BS1377 - Part 2: 1990;)

$$Ip = WL\text{-}Wp$$

Where:

IP is the plasticity index

WL is the liquid limit

WP is the plastic limit

iv) Linear Shrinkage

The linear shrinkage test was done on a sample passing a 425 micron sieve, having the moisture content of the liquid limit sample. The sample was placed in a brass linear shrinkage mould, air dried for 2 days until the soil shrunk from the walls of the mould, after which it was oven dried at 105°C. The length of the oven-dry specimen and the original length were measured and the linear shrinkage calculated as a percentage of the original length of the specimen as follows (BS1377 - Part 2: 1990):

$$\text{Percentage of linear shrinkage} = (1- Ld/Lo)\ x100.$$

Where:

Ld is the length of the oven-dry specimen

Lo is the original length

Free Swell Test

In addition, the swell test was carried out to measure the expansion of the clay when it is exposed to moisture. The swelling behaviour is particularly important for expansive clay soils like those found in Konza, as excessive swelling can cause structural damage to roads and foundations. The swell test involved submerging the soil sample in water for a period of time and measuring the resulting volumetric changes (Schreiner & Burland, 2022).10 ml of the material oven dried at 105°C was slowly poured into a 100 ml graduated cylinder filled with distilled water as shown in figure 3-6. The soil was allowed to settle, and the initial volume of the soil taken. The mixture was allowed to stand for 24 hours, and the swelled volume was measured from which the free swell was computed as shown below;

$$Swell\ percentage = \left(\frac{final\ volume - initial\ volume}{initial\ volume}\right) * 100$$

2.5. Strength Properties of Modified Clay Soil

Compaction Test

Compaction of soil is a procedure in which the solid particles are packed more closely together, usually by mechanical means, resulting in increased dry density of the soil. The dry density achievable is dependent on the degree of compaction applied and on the amount of water present in the soil. For a given degree of compaction of a given cohesive soil, there is an optimum moisture content at which the dry density obtained reaches a maximum value. The test was conducted according to BS 1377 part 4. The light manual compaction method (2.5kg hammer) was used on an air-dried pulverized material passing a 5 mm test sieve in this case. In this test, a 2.5 kg rammer falling through a height of 300 mm is used to compact the soil in three layers into a 1 L compaction mould. The following equations derive the dry densities which was then plotted as an ordinate against the corresponding moisture contents. A curve of best fit was then drawn to identify the position of the maximum.

$$\rho\ (bulk\ density) = \left(\frac{m2 - m1}{V}\right)$$

Where:

m1 is the mass of mould and baseplate (in g).

m2 is the mass of mould, baseplate, and compacted soil (in g).

V is the internal volume, (in cm3), of the mould.

$$\rho\ d\ (dry\ density) = \left(\frac{100\rho}{100 + w}\right)$$

Where:

w is the moisture content of the soil (in %)

California Bearing Ratio (CBR)

The California Bearing Ratio (CBR) test is critical for determining the load-bearing capacity of the untreated soil. In this test, a cylindrical plunger of given diameters was used to penetrate the soil sample, and the force required to achieve specific penetration levels was recorded. The CBR value was expressed as a percentage of the standard load-bearing capacity of crushed stone, serving as a benchmark. Higher CBR values indicate better load-bearing capacity, making the soil more suitable for road construction. The following steps were followed for this test (Arbianto et al., 2021);

- The soil sample was compacted in CBR moulds in layers. For each of the layers, stand and proctor compaction methods were used.
- The mould containing the compacted soil was placed in a CBR testing machine, a standard plunger of cross-sectional area of 1935mm2, was applied to the centre of the samples, and a load was applied to this plunger at a constant rate of penetration (Arbianto et al., 2021). The resistance of the plunger was noted as 13.2kN for the top and 20kN for the bottom.
- The force required to achieve penetration depths of the desired level was recorded and the CBR values of the sample were calculated as a percentage of the actual load recorded to the standard load at the same penetration levels. The formula to be used is as follows

$$CBR = \left(\frac{load\ at\ 2.5mm\ or\ 5mm\ penetration}{standrad\ load}\right) * 100$$

Unconfined Compressive Strength UCS

Unconfined Compressive strength is known as the maximum stress that a cohesive soil specimen can bear under zero confining stress. It is the load per unit area at which an unconfined cylindrical specimen of soil will fail in the axial compression test. The test was done according to BS 1377 (Part 7):1990. The test involved placing the prepared and measured sample on the bottom plate of the loading device, and the upper plate adjusted to make contact with the specimen. The force was then applied to produce an axial strain. The specimen was compressed until failure surfaces developed. (Arbianto et al., 2021).

- Stress-strain values.

$$Axial\ strain\ e, = \left(\frac{\Delta L\ (change\ in\ length)}{L0\ (initial\ specimen\ length\ )} * 100\right)$$

- Average cross-sectional area (A),

  $$Ave\ cross\ sectional\ area, A = \left(\frac{\text{A0 (initial cross−sectional area of specimen)}}{(1-e)}\right)$$

- Compressive Strength were determined from;

  $$Compressive\ strength, \sigma 0 = \left(\frac{\text{P (compressive force)}}{A\ (ave.cross-sectional\ area}\right)$$

Values of stress and strain obtained were plotted. The maximum stress from the plot gave the value of the unconfined compressive strength.

XRF and XRD was conducted for specimen that had been modified with the optimum percentage replacement of 25% CW and 15% CKD in order to check the changes that have occurred in the chemical/mineral composition of the modified expansive soil.

2.6. Development of Predictive Model

The methodology procedures included initial testing to determine the natural properties of the clay soil, subsequent modification of the expansive clay soil with pulverized ceramic waste and cement kiln dust to aid in stabilization and retesting of the CBR and swell properties after the application of pulverized CW and CKD to the expansive soil. Using the data obtained from these experiments, a predictive model was built to forecast the behaviour of the clay soil under different chemical treatments.

Soil Parameters

The key soil parameters to be investigated and thereafter develop a predictive model to forecast the behaviour of soil were the Swell potential and the soil CBR. Expansive clay soil without modification is known to have high swelling potential, which is not suitable for construction purposes. (Curtis 2013). The CBR of clay soil, which was reported to be poor, is also a common parameter that renders clay soil unsuitable for any construction or foundation works. (Shiding et al. 2018). These data were then used in coming up with a linear regression model to predict the Swell properties and CBR properties based on the different ratios of percentage replacements.

i) Swell Potential

Once the soil are applied, the treated soil samples will undergo another round of chemical property analysis. The XRF technique will be used again to detect any changes in the mineral and chemical structure of the soil. This test will help verify whether the chemical additives have effectively altered the soil's composition, thus contributing to improved Swell properties.

ii) Soil CBR

Once the chemical treatments are applied, the treated soil samples will undergo another round of chemical property analysis. The XRF technique will be used again to detect any changes in the mineral and chemical structure of the soil. This test will help verify whether the chemical additives have effectively altered the soil's composition, thus contributing to improved CBR properties.

Multiple Regression Model

The data collected from the initial and post-treatment CBR, and swell tests were used to develop a multiple regression model. The model was designed to predict the CBR, and swell properties of the modified soil based on the type and ratio of chemical additives used. The independent variables in the model included:

- Type of chemical additive (e.g., cement kiln dust, ceramic waste).
- Proportion of the chemical additive used (e.g. 5%, 10%,15% , 20% and 25%).

The dependent variables included:

- CBR value (measured as a percentage of the standard).
- Swell percentage (measured as the change in volume).

The multiple regression model will take the form;

$$Y_1 = \beta_0 + \beta_1 X_1 + \beta_2 X_2 + \beta_n X_n + e$$

Where;

Y is the dependent variable, in this case CBR or Swell

$\beta 0$ is the constant

$\beta 1$, $\beta 2$.... βn are the coefficients for the regression model’s independent variables,

X1, X2...Xn are the proportions of the different chemical treatments added

The model was built using statistical software R , and the predictive accuracy of the model was assessed using performance metrics, R-squared value.(Westfall & Arias, 2020). The model aims to serve as a valuable tool for determining the optimal chemical treatments for enhancing the stability of clay soils.

Model Validations

To ensure the reliability of the multiple regression model, several validation techniques will be employed:

- **Coefficient of determination:** To assess the predictive capability of the model, the coefficient of determination was used. The coefficient of determination is used to explain, the amount of variability in the model (Dependent variable) that can be explained by the predictor variables.
- **Residual analysis:** The residuals (differences between the observed and predicted values) will be examined to ensure that they are randomly distributed, indicating a good fit for the model (Neri, 2022).
- **Outlier analysis:** Any significant outliers that could distort the model's predictions will be identified and addressed (Neri, 2022).

3. Results

3.1. Material characteristics

The results for material characterization are discussed below.

Particle Size Distribution

These were the results of a Particle Size Distribution (PSD) test carried out on an expansive soil sample using standard sieve analysis. The purpose was to assess the gradation characteristics and determine the proportion of fine and coarse particles.

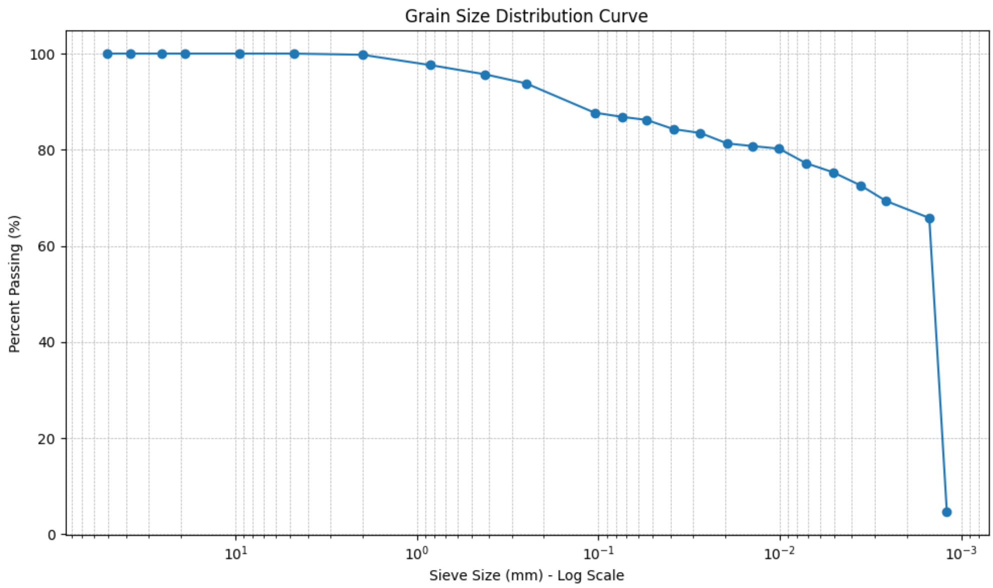

*Figure **Error! No text of specified style in document.**-10: Particle Size Distribution Curve*

The soil sample shows 100% passing for all course and medium gravel sizes (>4.76 mm), indicating an absence of gravel. Approximately 86.84% of the material passes the 0.075 mm sieve, classifying it as a fine-grained soil. The curve suggests the soil is well-graded with a smooth transition from course to fine particles. The steep slope in the fine region implies a relatively narrow distribution of fine particles, likely silt or clay.

Based on the Unified Soil Classification System (USCS), Soils with more than 50% passing the No. 200 sieve (0.075 mm) are classified as fine-grained. Given 86.84% passing the 0.075 mm sieve, this soil is classified as highly plastic clay (CH).

Specific Gravity

The specific gravity test was conducted using the pycnometer method. The specific gravity of the soil samples ranged between 2.10 and 2.41. The average specific gravity of the tested sample is 2.26 at 20°C. These values are typical for clay soils, indicating the presence of silicate minerals. A lower specific gravity compared to quartz-rich soils (~2.65) indicates the soil contains clay minerals with lower density, such as montmorillonite or kaolinite. This aligns with the classification of expansive soils (black cotton soils), which are rich in clay minerals responsible for swelling-shrinkage behaviour. Reddy, P. S., et al. (2018).

Atterberg Limits for Untreated Expansive Soil

For untreated expansive soil (neat), the liquid limit was recorded at 89.68%. The neat soil exhibited a plastic limit of 22.21%. The Plasticity Index of the neat soil was high at 67.47%, indicating highly plastic behaviour.

Such high LL and PI values classify the soil as highly expansive clay, consistent with the behaviour of black cotton soil. These values also explain the poor engineering performance—soils of this type typically cause heaving, shrinkage cracks, and structural distress in pavements and foundations.

Free Swell Index of Untreated Expansive Soil

The neat expansive soil recorded a very high Free Swell Index (FSI) of 193.75%. Most natural soils have an FSI below 50%, and anything above 100% is classified as highly expansive.

Such a high swell potential is consistent with soils dominated by montmorillonite-rich clays (like black cotton soil). When exposed to water, the clay minerals undergo hydration and interlayer expansion, which causes significant swelling. Upon drying, the soil shrinks dramatically, leading to cracking, differential settlements, and structural distress. Das, B. M. (2016).

XRD

X-ray diffraction (XRD) analysis was conducted on three distinct samples to determine their mineralogical compositions. These samples were labelled A, B, and C. The objective was to identify naturally occurring crystalline phases in each sample, which is essential for evaluating their engineering behavior and potential suitability for stabilization in future studies. The listed scan type for all samples was: Coupled TwoTheta/Theta | Radiation Wavelength: 1.78897 Å

i) XRD Sample A

Sample A shows the dominance of Moganite, indicating the presence of reactive silica. Sodium alum reflects ionic activity, while the presence of scandium and oxynitride phases illustrates mineral diversity. This profile is consistent with natural alumino-silicate-rich soils.

*Table **Error! No text of specified style in document.**-2: XRD Sample A profile*

Compound Name	Formula	Phase Type	Concentration (%)	Crystal System	Space Group (No.)	Density (g/cm³)
Moganite	O_2Si	Silica	37.6%	Monoclinic	I 1 2/a 1 (15)	2.620
Sodium Alum	$AlH_{24}NaO_{20}S_2$	Salt	12.46%	Cubic	P a -3 (205)	1.670
Scandium	Sc	Elemental	7.1%	Hexagonal	P 63/mmc (194)	2.990
PON	NOP	Oxynitride	1.8%	Orthorhombic	I 1 2/a 1 (15)	2.890

ii) XRD Sample B

Sample B is characterized by high calcite content, with additional phases including Galaxite and Clinomimetite. This indicates a mineralogical composition influenced by geochemical processes, possibly from carbonate or manganese-rich sources.

*Table **Error! No text of specified style in document.**-3: XRD Sample B profile*

Compound Name	Formula	Phase Type	Concentration (%)	Crystal System	Space Group (No.)	Density (g/cm³)
Calcite	$CCaO_3$	Carbonate	54.8%	Hexagonal	R -3 c :H (167)	2.710
Galaxite	$Al_{2.11}Mn_{0.89}O_4$	Spinel-type oxide	13.2%	Cubic	F d -3 m :2 (227)	4.120
Clinomimetite	$As_3ClO_{12}Pb_5$	Arsenate	32.0%	Monoclinic	P 1 1 21/b (14)	7.370

iii) XRD Sample C

Sample C is dominated by Moganite, suggesting a high silica content, along with Filipstadite, a complex oxide. These phases indicate unique mineral contributions, possibly from naturally occurring volcanic or igneous origin.

*Table **Error! No text of specified style in document.**-4: XRD Sample C profile*

Compound Name	Formula	Phase Type	Concentration (%)	Crystal System	Space Group (No.)	Density (g/cm^3)
Filipstadite	$Fe_{24.97}Mg_{35.53}O_{108}Sb_{20.496}$	Complex oxide	5.6%	Cubic	F d -3 m :2 (227)	4.940
Moganite	O_2Si	Silica	94.4%	Monoclinic	I 1 2/a 1 (15)	2.620

XRF

The results of the X-Ray Fluorescence (XRF) analysis conducted on the samples labelled A, B, C. The analysis provides the oxide composition of the material, which is essential in understanding its mineralogical and chemical characteristics. The results include major and minor oxides commonly found in geological and construction materials.

*Table **Error! No text of specified style in document.**-5: XRF Results – Sample A*

Analyte (Oxide)	**Result (%)**
SiO_2	52.214
Fe_2O_3	30.568
K_2O	9.153
CaO	4.354
TiO_2	1.599
MnO	1.339
ZrO_2	0.401
SO_3	0.120
SrO	0.100
CuO	0.090
NbO	0.061

The XRF results indicate that Sample A contains a high proportion of silicon dioxide (SiO_2), accounting for over 52% of the sample. This suggests a silica-rich composition, typical of ceramic or silicate-based materials. A notable feature is the elevated concentration of ferric oxide (Fe_2O_3) at approximately 30.57%, which may indicate the presence of iron-bearing minerals or industrial by-products such as red ceramic waste.Potassium oxide (K_2O) is present at over 9%, which is relatively high and could be indicative of feldspar content or the use of potassium-rich additives. Calcium oxide (CaO) and titanium dioxide (TiO_2) are present in moderate amounts, while other oxides such as MnO, ZrO_2, and SO_3 are detected in minor quantities. The trace levels of SrO, CuO, and NbO reflect background elemental content or possible contamination from industrial processes.

*Table **Error! No text of specified style in document.**-6: XRF Results Sample B*

Analyte (Oxide)	**Result (%)**
CaO	80.059
Fe_2O_3	8.061
SiO_2	6.567
K_2O	4.363
TiO_2	0.474
MnO_2	0.206
SrO	0.155
Br	0.076
ZrO_2	0.038

The XRF data for Sample B indicates a dominant presence of calcium oxide (CaO), accounting for over 80% of the composition. This suggests that the material is strongly calcareous, which is characteristic of substances such as lime, cement kiln dust (CKD), or similar industrial by-products. Moderate levels of ferric oxide (Fe_2O_3) and silicon dioxide (SiO_2) indicate the presence of iron and silicate phases, while potassium oxide (K_2O) and titanium dioxide (TiO_2) occur in smaller amounts. Trace elements such as strontium oxide (SrO), bromine (Br), and zirconium oxide (ZrO_2) appear in minor concentrations and may represent either natural mineral inclusions or residuals from processing.

*Table **Error! No text of specified style in document.**-7: XRF Results-Sample C*

Analyte (Oxide)	**Result (%)**
SiO_2	41.865
Al_2O_3	30.548
K_2O	14.866
CaO	5.091
Fe_2O_3	4.902
ZrO_2	1.214
TiO_2	1.094
ZnO	0.302
SrO	0.084
Rb_2O	0.033

Sample C is composed predominantly of silica (SiO_2) and alumina (Al_2O_3), comprising more than 70% of the total oxide content. This composition indicates that the sample is alumino-silicate rich, likely derived from clay-based or ceramic materials. The high potassium oxide (K_2O) content (14.866%) suggests the presence of feldspar or potassic minerals, typically used in ceramic manufacturing. Calcium oxide (CaO) and ferric oxide (Fe_2O_3) are present in modest amounts, while minor constituents such as ZrO_2, TiO_2, ZnO, SrO, and Rb_2O reflect trace mineral inclusions. This diverse mineralogy supports potential uses in ceramics, pozzolanic materials, or as fillers in construction.

3.2. Consistency and Swell Properties

Atterberg limits

i) Liquid limit

The liquid limit represents the water content at which soil changes from a plastic to a liquid state. For untreated expansive soil (neat), the liquid limit was recorded at 89.68%. With ceramic waste (CW) additions from 5% to 30%, there was a consistent and substantial reduction in the LL, reaching a low of 56.54% at 30% CW. This downward trend demonstrates the effectiveness of CW in reducing the moisture sensitivity of the soil. In contrast, CKD-stabilized soil showed a relatively slower decrease in LL, from 79.5% at 5% to 69.7% at 15%. This suggests that CW contributes more significantly to the reduction in LL than CKD. The reduction is attributed to flocculation and agglomeration of clay particles caused by pozzolanic reactions with CW and CKD, reducing water-holding capacity. Reddy et al. (2018), Sabat & Pati (2014). For the combined optimum mix of 25% CW + 15% CKD, the LL dropped sharply to 48.50%, compared to neat soil. This significant reduction surpasses the performance of both individual additives at their respective optimum levels. The combined improvement is likely due to the synergistic effect of CW's pozzolanic reactivity and CKD's cementitious and lime-rich composition, which together enhance particle binding, reduce diffuse double-layer thickness, and drastically lower the soil's affinity for water.

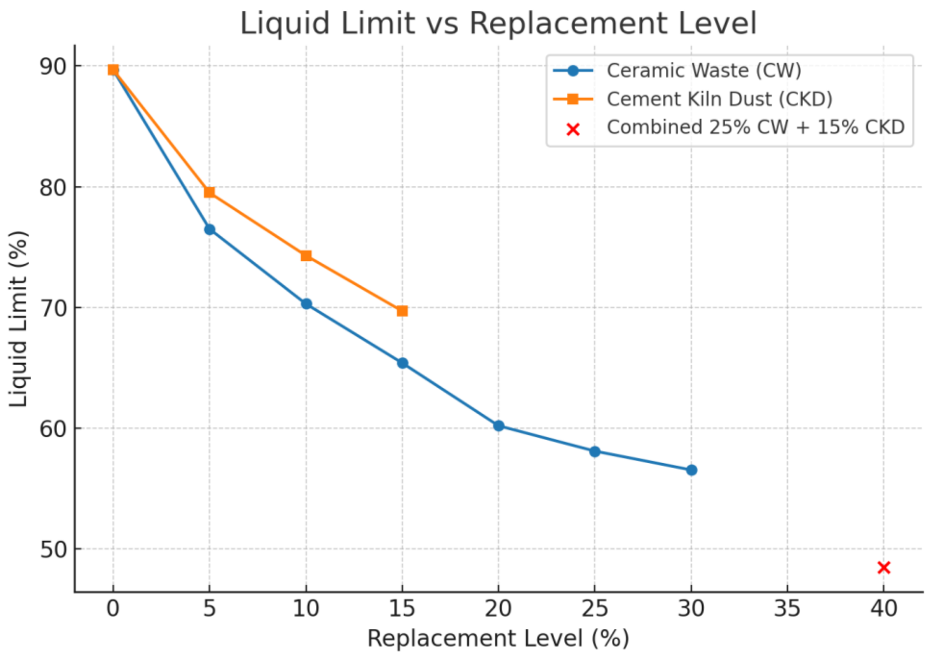

*Figure **Error! No text of specified style in document.**-11: Liquid limit vs Replacment level*

ii) Plastic limit

The plastic limit of expansive clay soil was analyzed for various replacement levels of Ceramic Waste (CW) and Cement Kiln Dust (CKD). Upon stabilization:

- With CW, the plastic limit steadily increased from 24.32% (5%) to 35.02% (30%) replacement, indicating enhanced workability and reduced soil plasticity.
- With CKD, the plastic limit increased from 24.29% (5%) to 31.66% (15%) replacement. This improvement is attributed to the cementitious and flocculating effects of CKD, which reduce the activity of expansive clay minerals.

For the combined mix of 25% CW and 15% CKD, the plastic limit reached 39.60%, representing the highest value observed among all mixes. The result indicates a synergistic effect: CW contributes significant pozzolanic activity and particle rearrangement, while CKD accelerates cementitious binding, producing a dense soil matrix with greatly reduced plasticity. The graph below presents a comparative trend of plastic limit variation for CW and CKD across different replacement percentages and the combined optimum replacement percentage.

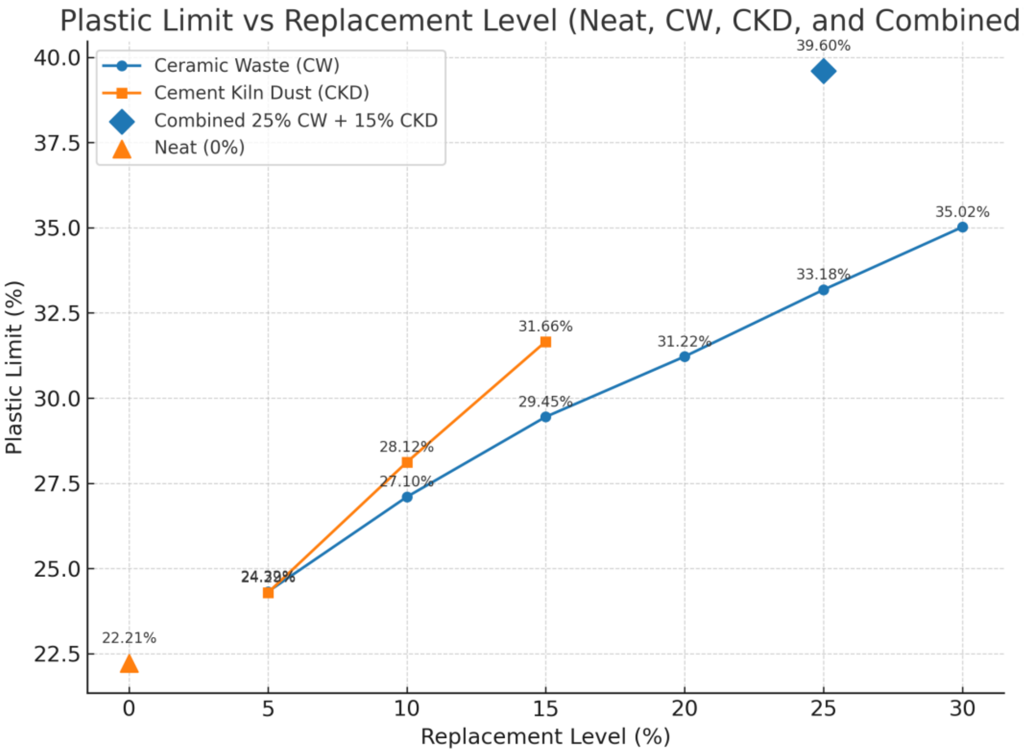

*Figure **Error! No text of specified style in document.**-12: Comparative trend of plastic limit variation for CW and CKD*

The addition of ceramic or cementitious particles reduces the plasticity by replacing clay fines and reducing surface activity. Kumar & Sharma (2017), Sivapullaiah & Baig (2011)

iii) Plasticity index

The plasticity index, calculated as the difference between the LL and PL, defines the range over which the soil remains plastic. With CW stabilization, the PI consistently reduced, reaching 20.97% at 30% replacement, reflecting a significant improvement in soil behavior. Conversely, CKD-stabilized soils showed a less steep reduction in PI from 49.2% to 36.8% across the same replacement range. These findings reinforce that ceramic waste is more effective in reducing the plasticity of expansive soils compared to CKD. Indicates improved soil behavior with less susceptibility to volume change. Soils become more workable and less expansive. Basha et al. (2005), Ramesh & Sivapullaiah (2012). For the combined optimum mix of 25% CW and 15% CKD, the PI was measured at 15%, indicating an even greater reduction in plasticity compared to either stabilizer used individually. This demonstrates the synergistic effect of combining CW and CKD, likely due to enhanced particle agglomeration and stronger cementitious bonding.

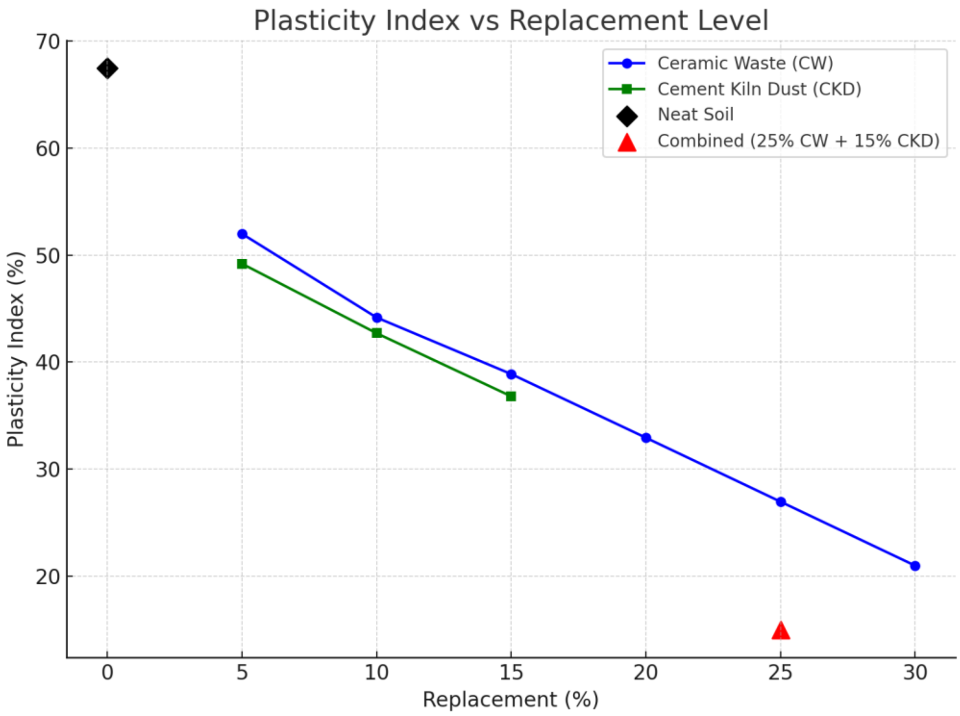

*Figure **Error! No text of specified style in document.**-13: Plasticity index vs Replacement level*

Free Swell Index

This analysis incorporated Free Swell Index (FSI) values for expansive soil treated with Ceramic Waste (CW) at replacement levels of 5%, 10%, 15%, 20%, 25%, and 30% and Cement Kiln Dust (CKD) at 5%,10% and 15%.

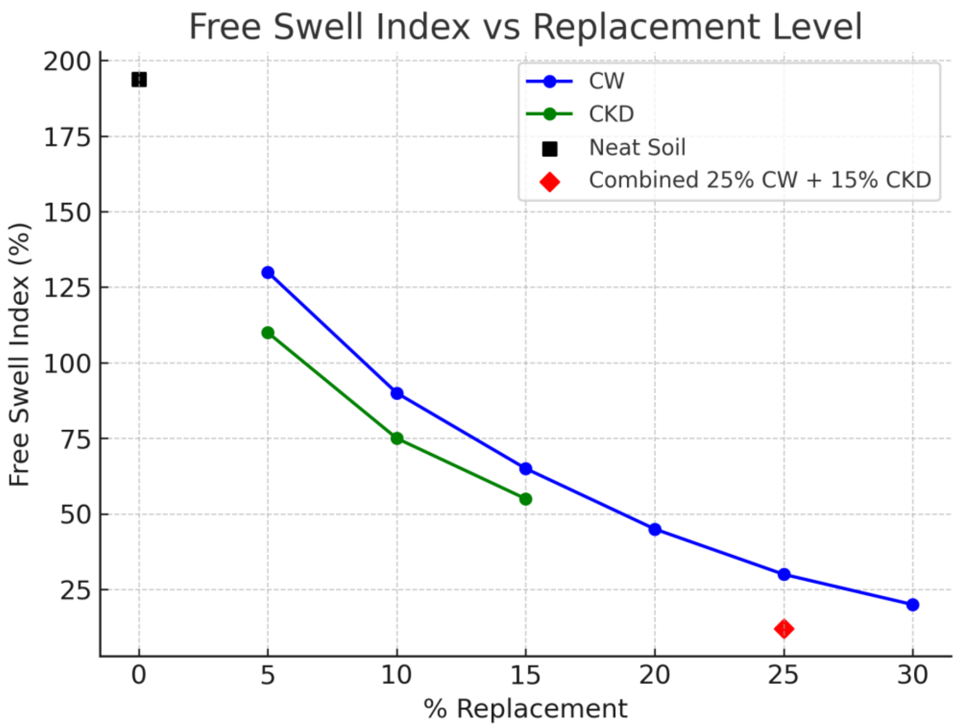

*Figure **Error! No text of specified style in document.**-14: Swell index vs Replacement level*

The results showed that the FSI reduced significantly with increasing CW content. Specifically, FSI reduced from 193.75% for neat black cotton soil to 20% at 30% CW replacement, representing an 89.7% decrease. Cement Kiln Dust (CKD) also demonstrated a decline in FSI, though less drastic. FSI reduced from 193.75% (neat) to 55% at 15% CKD replacement, which corresponds to a 71.6% reduction. These trends affirm that both CW and CKD significantly improve the volumetric stability of expansive soils, with CW exhibiting a more effective reduction rate at higher dosages. The combined stabilization at 25% CW and 15% CKD achieved the most dramatic reduction in FSI, reaching a value of 12%, representing a 93.8% decrease compared to the neat soil. This indicates a synergistic effect between CW and CKD, where the pozzolanic activity, cementitious reactions, and particle rearrangement collectively minimize water absorption and swelling.

3.3. Strength Properties

Compaction Characteristics

This section presents the detailed analysis of compaction characteristics for neat expansive soil, Ceramic Waste (CW) stabilized soil (5%–30% replacement), Cement Kiln Dust (CKD) stabilized soil (5%–15% replacement), and the optimum combined mix of 25% CW + 15% CKD. The parameters considered are Maximum Dry Density (MDD) and Optimum Moisture Content (OMC).

MDD vs % Replacement

The graph below illustrates the variation of MDD with percentage replacement for CW, CKD, and the combined optimum mix. For neat soil, MDD was recorded at 1.68 g/cm³. With CW addition, MDD increased slightly to a maximum of 1.72 g/cm³ at 15% replacement, then decreased marginally to 1.68 g/cm³ at 30% replacement. For CKD, MDD improved consistently from 1.69 g/cm³ at 5% to 1.725 g/cm³ at 15%. The combined mix exhibited an MDD of approximately 1.74 g/cm³, reflecting the synergistic effect of both stabilizers.

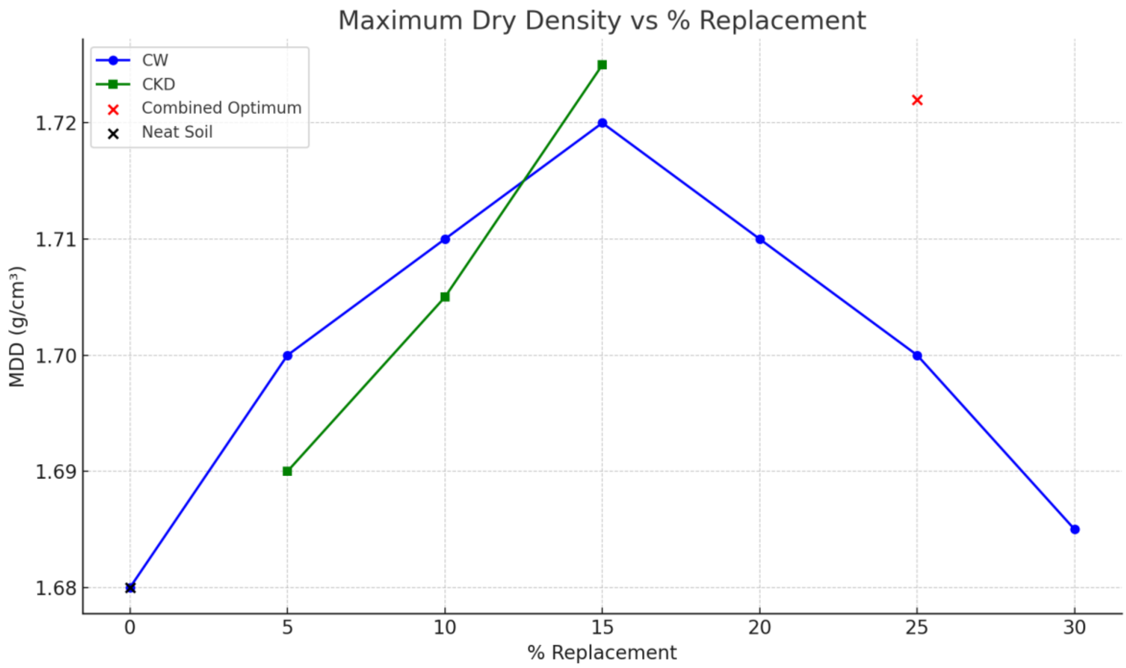

Figure ***Error! No text of specified style in document.****-15: Variation of MDD with percentage replacement for CW &CKD,*

OMC vs % Replacement

The OMC trends show a general increase with higher replacement percentages. Neat soil had an OMC of 12.5%. CW increased OMC from 13.0% at 5% replacement to 14.7% at 30% replacement. CKD showed a more gradual increase, from 12.8% at 5% to 13.5% at 15%. The combined mix recorded an OMC of approximately 14.2%, indicating slightly higher water demand during compaction due to improved soil particle packing and cementitious bonding.

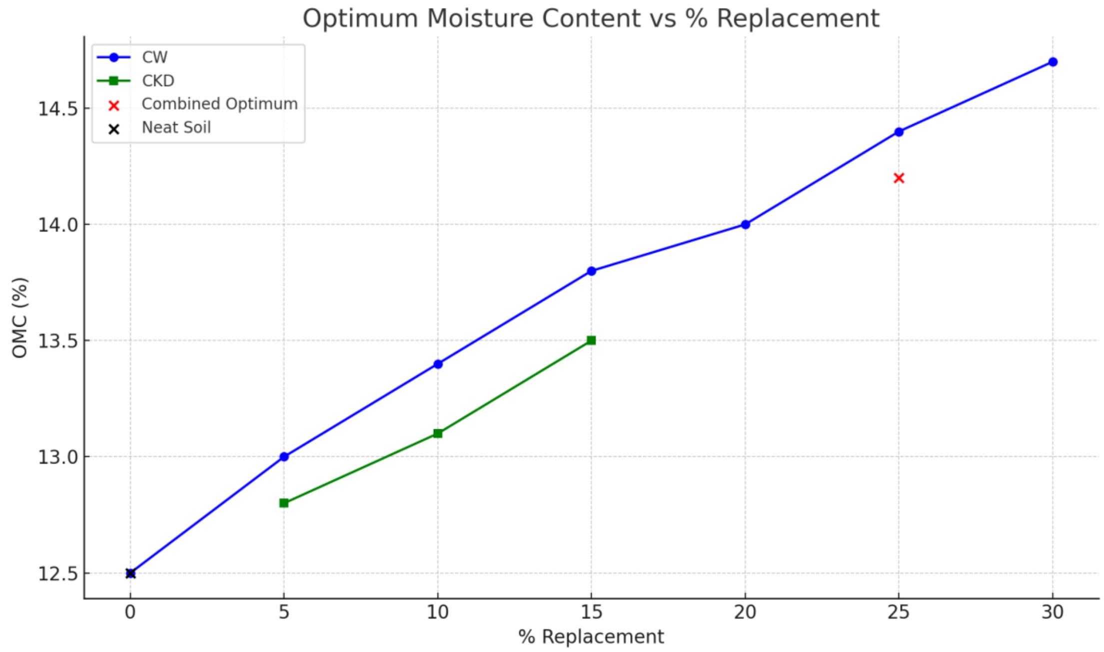

*Figure **Error! No text of specified style in document.**-16: Variation of OMC with percentage replacement for CW, CKD,*

California Bearing Ratio (CBR)

The California Bearing Ratio (CBR) test results for black cotton soil (BCS) samples treated with ceramic waste (CW) and cement kiln dust (CKD) are presented below. The objective was to evaluate how ceramic waste and CKD influence the strength characteristics of expansive soil, specifically its CBR value.

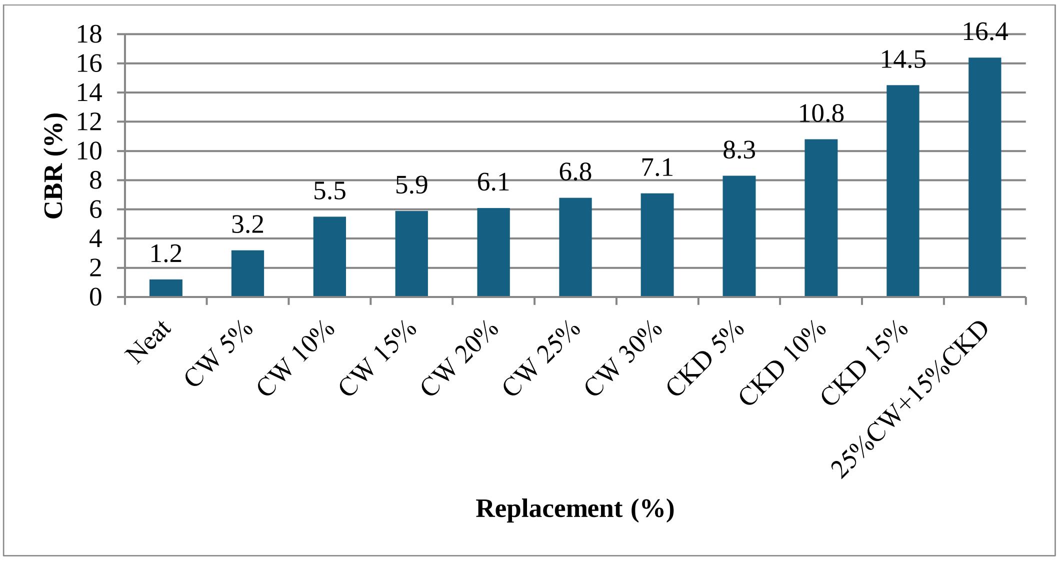

*Figure **Error! No text of specified style in document.**-17: CBR vs Replacement Percentage*

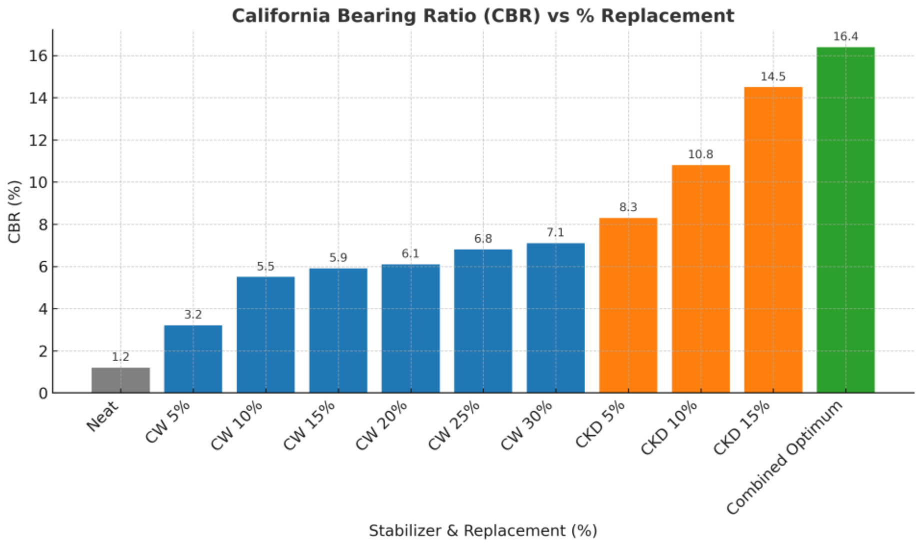

*Figure **Error! No text of specified style in document.**-18: CBR changes with Stabilizer percentages*

The neat black cotton soil (BCS) recorded a CBR value of 2.4%, indicating weak subgrade strength. With increasing percentages of ceramic waste, the CBR gradually improved, peaking at 7.1% for 30% The trend confirms that higher dosages improve strength, but with diminishing returns, especially for CW beyond 20–25%. CKD exhibited a stronger stabilizing effect: 5% CKD resulted in 8.3% CBR, and 15% CKD peaked at 14.5%. This demonstrated that CKD, due to its alkaline content and reactivity, offers superior strength improvement compared to CW alone.The combined optimum mix of 25% CW and 15% CKD exhibited the highest CBR value at 16.4%, representing a substantial increase compared to the neat soil. This synergistic effect is attributed to the complementary mechanisms of CW and CKD—CW provides fine particles for packing and reducing voids, while CKD contributes strong cementitious bonds.

The result is a stabilized soil with improved strength, durability, and reduced susceptibility to deformation under load.

Unconfined Compressive Strength (UCS)

This report presents the Unconfined Compressive Strength (UCS) of expansive black cotton soil stabilized using Pulverized Ceramic Waste and Cement Kiln Dust (CKD). UCS testing was conducted at 7, 14, and 28 days of curing to assess strength development over time.

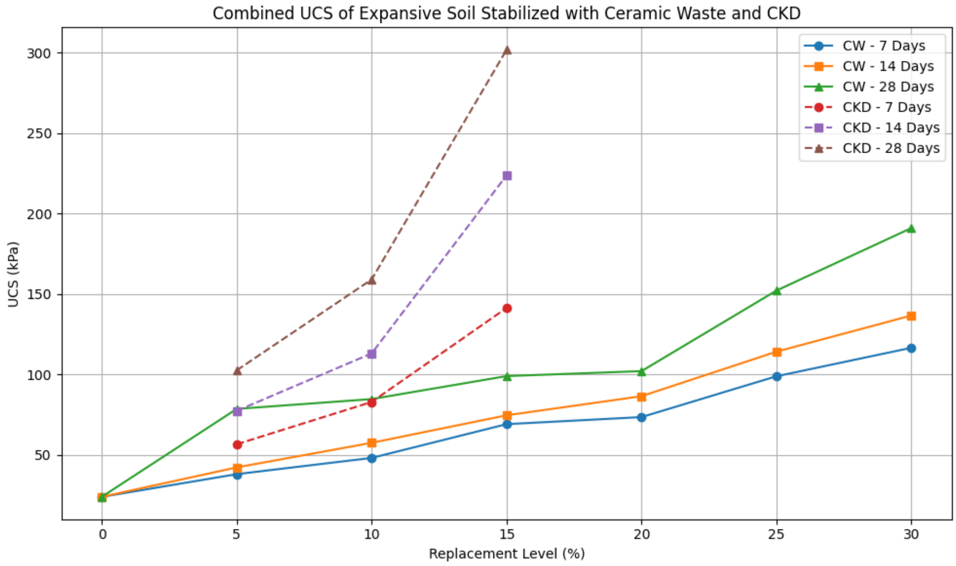

*Figure **Error! No text of specified style in document.**-9: UCS changes with stabilizer addition*

This combined graph illustrates the Unconfined Compressive Strength development for both CW and CKD stabilized soils at 7, 14, and 28 days of curing. CKD exhibits significantly higher UCS values across all time intervals, with maximum strength of 301kPa achieved at 15% replacement. CW also shows progressive strength gain, particularly at higher replacement levels, attaining a maximum of 191kPa at 30%. The trends highlight CKD's superior early strength due to rapid pozzolanic activation, while CW provides steady gains over time.

The combined mix delivered the highest UCS of 325.5 kPa at 28 days, indicating a synergistic effect between CW and CKD, combining pozzolanic reactivity and cementitious binding (Yahia Mohamedzein, Mohamed Al-Aghbari, & Zuweina Al Kindi, 2025).

XRD Sample for CW+CKD Treated Expansive soil

The treated soil sample—composed of expansive soil modified with ceramic waste and cement kiln dust—displays a distinctly altered mineral composition.

*Table **Error! No text of specified style in document.**-8: XRD Sample for CW+CKD Treated Expansive soil*

Compound Name	Formula	Phase Type	Concentration (%)	Crystal System	Space Group (No.)	Density (g/cm³)
Sanidine	$AlKO_8Si_3$	Feldspar	35.2%	Monoclinic	C 1 2/m 1 (12)	2.570

Calcite	$CCa_{0.9}Mg_{0.1}O_3$	Carbonate	28.1%	Hexagonal	R -3 c :H (167)	2.750
Moganite	O_2Si	Silica	19.8%	Monoclinic	I 1 2/a 1 (15)	2.620
Magnesium Calcite	$CCa_{0.94}Mg_{0.06}O_3$	Carbonate Variant	16.8%	Hexagonal	R -3 c :H (167)	2.730

Sanidine ($AlKO_8Si_3$) – 35.2%: A potassium feldspar typically found in ceramics. Calcite ($CCa_{0.9}Mg_{0.1}O_3$) – 28.1%: A carbonate mineral associated with CKD. Moganite (O_2Si) – 19.8%: Still present but in reduced quantity. Magnesium Calcite ($CCa_{0.94}Mg_{0.06}O_3$) – 16.8%: A variant of calcite with magnesium substitution. The XRD comparison reveals that the CW + CKD treatment significantly alters the mineral profile of the expansive soil. Reactive silica phases like Moganite are reduced in favor of feldspars and carbonates, indicating the presence and influence of the additives. These changes reflect both chemical substitution and mineral dilution effects and provide insight into how industrial waste materials can structurally alter soil composition.

XRF Sample for CW+CKD Treated Expansive soil

Table ***Error! No text of specified style in document.****-11: XRF Sample for CW+CKD Treated Expansive soil*

Analyte oxide	**Results**
CaO	49.871
SiO2	29.190
MgO	7.950
Fe	5.243
Al2O3	4.669
Ti	0.719
K2O	0.491
Zr	0.342
S	0.278
Cl	0.240
Mn	0.207

Zn	0.149
Sr	0.119
Y	0.058
Rb	0.033
Nb	0.026
Ni	0.022
Cu	0.014
As	0.013

In contrast with the neat sample, the treated soil sample—modified using CW and CKD—exhibits a drastically increased CaO concentration (49.871%), pointing to substantial input from cement kiln dust. This enrichment significantly enhances the potential for pozzolanic activity when reacted with available silica (SiO_2 = 29.190%) and alumina (Al_2O_3 = 4.669%). Magnesium oxide (MgO = 7.950%) and iron (Fe = 5.243%) contribute further to the binding phase formation, typically forming strength-enhancing C-S-H, C-A-H, and M-S-H gels.

Specific Gravity

Below is a comparative analysis of the specific gravity of expansive clay soil treated with varying percentages of Ceramic Waste (CW) and Cement Kiln Dust (CKD). Specific gravity values increased with higher replacement levels for both CW and CKD. For CW: The specific gravity ranged from 2.28 at 5% to 2.37 at 30%, indicating a steady improvement. For CKD: Specific gravity rose from 2.33 at 5% to 2.39 at 15%, showing a slightly steeper increase than CW. The higher values in CKD-treated samples may be attributed to the denser nature and finer particles of CKD compared to CW.

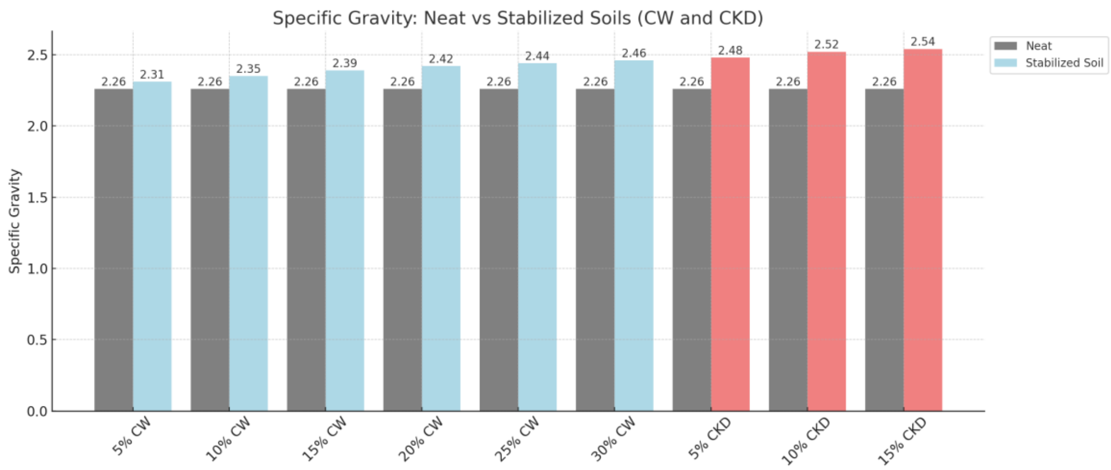

*Figure **Error! No text of specified style in document.**-19: Specific gravity of Treated expansive clay soil*

3.4. Regression Analysis and Strength Predictive Models

Introduction

In order to better understand the relationship between the stabilizer content and the behavior of the Konza soil, regression analysis was carried out using linear models, and this was done to address the fourth objective of this study, which is to develop equations that can predict soil properties without the need to repeat laboratory experiments, which as such, saves both time and resources, and on the other hand, helps engineers to make informed decisions when planning stabilization projects (Mitchell, 2018). In simpler terms, regression analysis shows the trend of how increasing CW or CKD content affects the swell potential, CBR, of the soil, and moreover, it provides a tool to forecast soil behavior for different percentages of stabilizer, which is important when designing subgrades, pavements, or light structures.

Regression Analysis for Swell Potential

The effect of stabilizer content on the swell potential of Konza soil was analyzed using linear regression, and the results showed that both CW and CKD reduce the swell in a roughly linear manner. The derived equations along with the goodness of fit (R^2) are shown in Table 4-12.

*Table **Error! No text of specified style in document.**-12: Linear Regression Models for Swell Potential*

Stabilizer	**Linear Regression Equation**	R^2
CW	Swell (%) = 138.33 – 4.286 × CW%	0.947
CKD	Swell (%) = 135.0 – 5.5 × CKD%	0.976

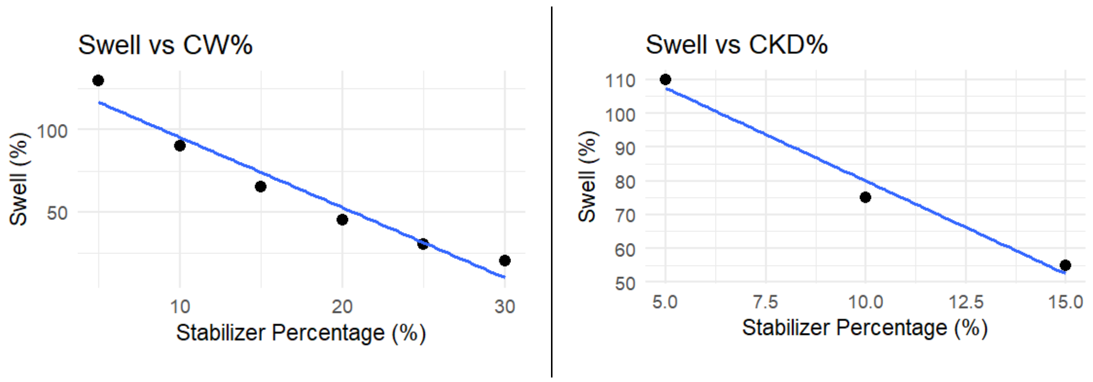

*Figure **Error! No text of specified style in document.**-20: Swell potential regression plots*

Figure 4-12 illustrates the regression plots for swell potential against stabilizer content. The high R^2 values indicate a strong linear relationship between stabilizer dosages and swell reduction. From the regression coefficients, it is observed that each 1% increase in CW content reduces swell potential by approximately 4.29%, whereas CKD achieves a higher reduction of about 5.5% per 1% addition. This indicates that CKD is more effective in controlling swell at lower dosages compared to CW. The close agreement between experimental data points and regression lines confirms the suitability of these models for predicting swell behavior within the investigated stabilizer range.

Regression Analysis for CBR

Linear regression was also applied to CBR data, and it was observed that increasing the stabilizer content leads to a steady increase in CBR, with CKD providing faster improvement than CW. Table 4-13 shows the derived linear equations and R^2 values.

*Table **Error! No text of specified style in document.**-13: Linear Regression Models for CBR*

Stabilizer	Linear Regression Equation	R^2
CW	CBR (%) = 3.407 + 0.135 × CW%	0.826
CKD	CBR (%) = 5.0 + 0.62 × CKD%	0.988

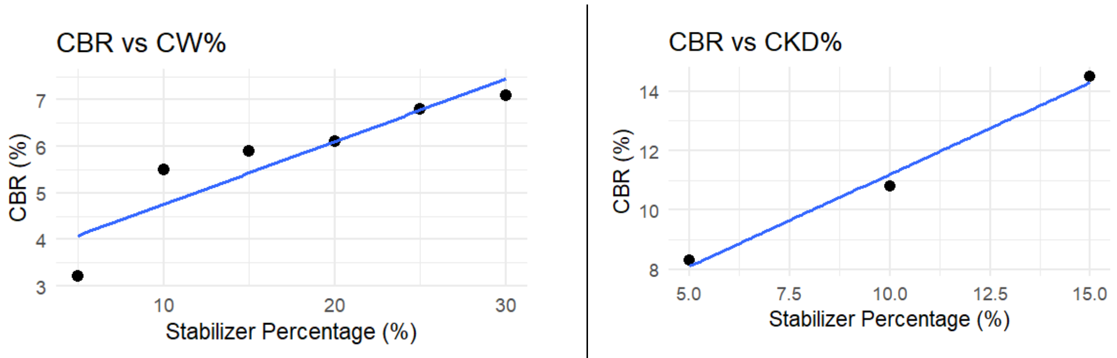

*Figure **Error! No text of specified style in document.**-21: CBR regression plots*

As shown in Figure 4-13, the regression lines closely follow the experimental data, particularly for CKD-treated soil. The regression coefficients indicate that each 1% increase in CW content results in an average CBR increase of 0.135%, while CKD increases CBR by approximately 0.62% per 1% addition. The significantly higher R^2 value obtained for CKD (0.988) suggests a very strong predictive capability of the model. These regression equations can therefore be reliably used to estimate the CBR of stabilized Konza soil for various stabilizer dosages, making them valuable tools in the preliminary design of pavement subgrades and foundation layers.

Model Validation

Coefficient of Determination

To assess the predictive capability of the model, the coefficient of determination was used. The coefficient of determination is used to explain, the amount of variability in the model (Dependent variable) that can be explained by the predictor variables. In this case, both the models for predicting swell and CBR showed high R^2 values indicating a strong linear relationship between stabilizer dosage and the resulting outcome in swell and CBR.

Residual Analysis

Residual analysis was conducted to evaluate the adequacy of the linear regression models and to verify compliance with regression assumptions. The residuals, defined as the differences between observed and predicted values, were examined and found to be randomly distributed around zero, with no discernible systematic patterns. This randomness indicates that the linear model appropriately captures the relationship between stabilizer content and soil response variables. Additionally, the absence of trends or curvature in the residual plots suggests that the assumption of linearity is valid and that the models provide unbiased predictions of both swell potential and CBR.

Outlier Analysis

Outlier analysis was performed to identify any extreme data points that could disproportionately influence the regression results and compromise model reliability. The dataset was examined for unusually large residuals and leverage points, and no significant outliers were detected that required exclusion or correction. The consistency of the data points around the regression lines further supports the robustness of the developed models. This confirms that the predictive equations are based on stable and representative experimental data, enhancing confidence in their application for estimating the behavior of stabilized expansive clay soils.

4. Discussions

Discussion of Key Findings

Material Characteristics

Baseline characterization revealed that the natural soil is highly expansive, dominated by fine particles (86.84% passing 0.075 mm) and classified as CH-highly plastic clay, consistent with montmorillonite-rich black cotton soils. The very high Liquid Limit (89.68%), Plasticity Index

(67.47%), and Free Swell Index (193.75%) confirmed severe susceptibility to moisture-driven heave and shrinkage.

XRD and XRF analyses indicated that the soil and ceramic waste are alumino–silicate rich, while CKD is predominantly calcareous, containing up to 80% CaO. This complementary chemical profile provided a high potential for pozzolanic and cementitious reactions when used together.

Compaction Characteristics

Compaction tests showed Maximum Dry Density (MDD) improved slightly from 1.68 g/cm³ (neat) to 1.72 g/cm³ at 15% CW, and 1.725 g/cm³ at 15% CKD. The combined mix achieved the highest density at approximately 1.74 g/cm³, indicating improved particle packing and reduced void ratio.

OMC increased modestly due to higher moisture demand during hydration and bond formation, similar to other alkali-activated systems (Kumar & Sharma, 2017).

Swell Potential Reduction

The natural Konza soil showed very high swell potential of 193.75% which indicates it is highly expansive and cannot be used for any engineering purpose without modification. As such, it becomes very important to apply some form of stabilization before using this soil for foundations or any structural application (Mitchell & Soga, 2005). In simpler terms, this very high swell is caused by the presence of montmorillonite clay mineral in the soil that absorbs water and expands significantly, and on the other hand, such behavior explains why untreated Konza soil often causes cracks and structural failures when used directly in construction.

When we look at the CW stabilization, the swell potential reduced to 20% at 30% content. This represents an approximate reduction of nearly 90% compared with the untreated soil, indicating that ceramic waste is highly effective in suppressing the swelling behaviour of expansive clays. This improvement can be linked to the filler effect where the ceramic particles replace some of the active clay minerals and reduce water absorption (Cabalar et.al 2016). In simpler terms, the ceramic particles take up the space that would normally be occupied by water. On the other hand, CKD stabilization reduced swell to 55% at only 15% content, showing it works better per percentage added. This reduction represents a decrease of over 70% relative to the natural soil, demonstrating the strong chemical stabilization potential of CKD even at relatively low dosages. This can be attributed to CKD's chemical activation where it reacts with clay minerals to form cementitious bonds that bind the soil particles and limit their expansion (Abdullah et.al 2011). As such, while both stabilizers reduce swell, CW is better for maximum swell control while CKD works faster at lower percentages.

Improvement in California Bearing Ratio (CBR)

The natural Konza soil showed a very low California Bearing Ratio of 1.20% which indicates it has extremely poor subgrade strength and cannot support pavement or foundation loads without modification. As such, it becomes very important to apply some form of stabilization before using this soil for any road construction or structural application (Mitchell & Soga, 2005). In simpler terms, this very low bearing capacity is caused by the weak, expansive nature of the clay minerals in the soil, and on the other hand, such behavior explains why untreated Konza soil often leads to pavement failures and structural settlement when used in construction.

When we look at the CW stabilization, the CBR increased to 7.1% at 30% content. This improvement can be linked to the mechanical stabilization where the ceramic particles provide better particle interlock and density to the soil mixture (Kabubo et.al 2017). In simpler terms, the hard ceramic particles help the soil resist penetration better by creating a more stable particle arrangement. On the other hand, CKD stabilization showed much better performance with CBR of 14.5% at only 15% content. This can be attributed to CKD's chemical bonding where it reacts with clay minerals to form cementitious compounds that significantly increase the soil's stiffness and load-bearing capacity (Dang et.al 2016). As such, while both stabilizers improve CBR, CKD is much more effective for achieving the higher CBR values required for quality subgrade materials according to the Kenya Road Design Manual.

Enhancement of Unconfined Compressive Strength (UCS)

The natural Konza soil showed a very low Unconfined Compressive Strength of 23.8 kPa which indicates it is very weak and cannot resist structural loads without modification. As such, it becomes very important to apply some form of stabilization before using this soil for foundations or any structural application (Mitchell & Soga, 2005). In simpler terms, this very low strength is caused by the weak bonding between clay particles in the natural soil, and on the other hand, such behavior explains why untreated Konza soil fails quickly under compression when used in construction.

When we look at the CW stabilization, the UCS increased to 191 kPa at 30% content. This improvement can be linked to the particle interlock and partial pozzolanic activity where the ceramic particles provide better mechanical strength to the soil mixture (Chibuzor et.al 2018).

In simpler terms, the hard ceramic particles create a stronger skeleton that resists compression forces better. On the other hand, CKD stabilization showed much better performance with UCS of 301.9 kPa at only 15% content. This can be attributed to CKD's strong chemical activation where it rapidly forms cementitious C-S-H and C-A-H gels that bind soil particles together into a strong mass (Abdullah et.al 2011). As such, while both stabilizers improve UCS, CKD is much more effective for achieving the high strength values required for structural foundations, while CW provides good improvement where maximum strength is not the main requirement. In addition, the unconfined compressive strength was observed to increase with curing time, indicating that stabilization reactions continue to develop gradually as cementitious compounds form within the soil structure.

Comparative Analysis of CW and CKD Performance

When comparing the performance of CW and CKD, it can be argued that both stabilizers have resulted in tremendous improvements to Konza soil properties. However, there are clear differences in their effectiveness that have greatly influenced which stabilizer is better for specific engineering goals. For instance, CW stabilization has been more effective in swell reduction, achieving 20% at 30% content, while CKD stabilization has shown better strength performance, reaching 301.9 kPa UCS at only 15% content. These differences are not only due to differences in material composition, but also due to the chemical interactions between the stabilizers and the soil's mass.

In addition to evaluating the individual performance of CW and CKD, the combined use of both stabilizers produced even greater improvements in soil behavior. The mixture of CW and CKD resulted in the best overall performance among all tested combinations, demonstrating that the interaction between the two materials enhances the stabilization process. For instance, the combined mixture achieved the lowest swell potential of approximately 12%, the highest CBR value of about 16.4%, and the maximum UCS value of about 325.5 kPa. These results indicate that the combined stabilizer system is more effective than using either material individually. The combined mix produced the most stable soil structure due to simultaneous: pozzolanic binding,, calcium–silica–hydrate (C–S–H) and calcium–aluminate–hydrate (C–A–H) gel formation, reduction in clay-water affinity. (Reddy et al., 2018; Das, 2016).

In today's soil stabilization processes, both physical and chemical methods have been on the rise. This has led to the ability of these methods being in a position to construct different soil properties and influence the choice of stabilizer for specific projects (Kabubo et.al 2017). In simpler terms, CW works mainly through physical stabilization where ceramic particles replace expansive clay, and on the other hand, CKD works through chemical activation that creates strong cementitious bonds (Abdullah et.al 2011). The CBR results further show this pattern, where CKD reached 14.5% at 15% content while CW achieved only 7.1% at 30% content. As such, for projects requiring high strength, CKD is the preferred stabilizer, while for applications where swell control is the main concern, CW provides excellent performance.

Predictive Modelling

Linear regression analysis was successfully applied to develop predictive models for swell potential and CBR of expansive clay soil stabilized with Ceramic Waste (CW) and Cement Kiln Dust (CKD):

- Strong linear relationships between stabilizer content and soil performance were established, with high coefficients of determination ($R^2 > 0.94$ for swell potential and up to 0.99 for CBR).
- Both CW and CKD reduced swell potential in a near-linear manner, with CKD achieving faster reduction at lower dosages while CW required higher replacement levels to achieve comparable reductions.
- The derived swell prediction equations can reliably estimate expected swell reduction for any stabilizer content within the tested range.
- CBR values increased steadily with increasing stabilizer content for both materials, with CKD providing greater strength improvement per percentage addition due to its cementitious nature.
- The CBR predictive models, particularly for CKD ($R^2 = 0.988$), demonstrated excellent accuracy in estimating subgrade load-bearing capacity.

The developed predictive models minimize the need for repetitive laboratory testing, saving time and resources during pavement and foundation design. Overall, the successful development and validation of these predictive models confirm the full achievement of Objective 4 of this study.

5. Conclusions and Recommendations

Conclusions

In conclusion, this study has shown that industrial by-products can significantly change how we deal with difficult soils in Kenya. The research confirms that both Ceramic Waste and Cement Kiln Dust can improve Konza clay soil, though each material works differently for different soil problems. However, while it can be argued that both materials work well, there are clear differences in what each one does best.

CW works very well for reducing soil swelling, while CKD is much better at making soil stronger. These differences are not only because of what the materials are made of, but also because they work in different ways inside the soil. CW works mainly through physical stabilization where ceramic particles replace expansive clay, and on the other hand, CKD works through chemical activation that creates strong cementitious bonds (Abdullah et.al 2011). N the other hand, the combination of CW and CKD produces a synergistic effect, outperforming either material used individually, especially in, reduction of LL, PI, and FSI, increase in MDD, improvement in CBR, and UCS strength. As such, using these materials provides a good solution for improving bad soils in Kenya, while also helping to reduce waste materials in the country.

Recommendations

Based on the study findings, and in a country where engineers have faced a lot of challenges with expansive soils that have greatly affected building projects negatively, this study has shown that industrial by-products can provide new solutions for these soil problems. Based on the findings, several recommendations can be made for how to use these materials in Kenya's construction industry.

For construction projects that need very strong soil, such as highway pavements or building foundations, Cement Kiln Dust (CKD) is strongly recommended because it makes soil much stronger even when using small amounts. On the other hand, for projects where the main problem is soil swelling, such as in road embankments, Pulverized Ceramic Waste (CW) works much better, especially when using higher amounts. This material can reduce swelling by a very large amount compared to normal soil.

Furthermore, using both CW and CKD together might work well for difficult projects with the optimum mix of 25% CW + 15% CKD. In this case, CW can work as a filler that improves the soil structure while CKD works as a chemical that makes the soil stronger. This combination could give both good swelling control and good CBR and UCS strength. Finally, engineers could use the prediction models from this study to estimate how soil will behave before starting projects. This can help save both time and money on construction projects in Kenya while minimizing repetitive laboratory testing during feasibility and preliminary design stages.

Other recommendation include advocating for a minimum curing period of 14–28 days for significant compressive strength development. And lastly, where CKD chemical content varies between factories, pre-characterization tests should be conducted to determine available lime (CaO), LOI, and pozzolanic potential.

Suggested Areas for Further Research

While this study has answered some important questions, it also shows that more research is needed in several areas. There is still very little information about how these improved soils will behave over many years in real and different weather conditions in Kenya. Future research should therefore focus on several important topics that need more understanding.

First, more studies should look at the long-term performance of treated soils, including how they handle weather changes like rainy seasons and dry periods. Second, conducting microstructural analysis using methods such as SEM and FTIR to confirm the physical and chemical changes suggested by the mechanical results in this study would provide more insights. Third, further research should find the best way to mix CW and CKD together to get the best results from both materials in order to achieve a balance of swell reduction and improved CBR and UCS.

Moreover, studying whether using these materials is cheaper than using traditional methods would be very useful for getting more people to use them in Kenya. These research areas would help fill the current gaps in knowledge and provide better understanding of how to use industrial by-products for soil improvement across the country.

References

1. A Sheron 2022. Study of structures in black cotton soil.
2. A. Abdullah, M. S Jaafar, Y. H Taufiq-Yap, A. Alhozaimy and A. Al-Negheimish and J. Noorzaei 2012. The effect of various chemical activators on pozzolanic reactivity.
3. A. Abdullah, M. S Jaafar, Y. H Taufiq-Yap, A. Alhozaimy And A. Al-Negheimish and J. Noorzaei 2011. The effect of various chemical activators on pozzolanic reactivity: a review.
4. A. F. Cabalar∗, D. I. Hassan and M. D. Abdulnafaa 2016. Use of waste ceramic tiles for road pavement subgrade.
5. A. Maneli, W. K. Kupolati, O. S. Abiola and J. M. Ndambuki 2015. Influence of fly ash, ground-granulated blast furnace slag and lime on unconfined compressive strength of black cotton soil.

6. A. Sridharan, Phd, Dsc and K. Prakash, Phd 2000. Classification procedures for expansive soils.
7. Ajay Upadhyay, Suneet Kaur 2016. Review on soil stabilization using ceramic waste
8. Akshaya Kumar Sabat 2012. Stabilization of Expansive Soil Using Waste Ceramic Dust
9. Alejandra Balaguera, Gloria,Isabel Carvajal, Jaume Albertí , Pere Fullana-i-Palmer 2018. Life cycle assessment of road construction alternative materials.
10. Ali Akbar Firoozi, Ali Asghar Firooz 2023. Assessment of lime stabilization of black cotton soil for roads construction projects.
11. Al-Mukhtar, M., Lasledj, A., And Alcover, J.-F. (2010). “Behaviour and mineralogy changes in lime-treated expansive soil at 20°c.” *Appl. Clay sci.*, 50(2), 191–198.
12. Araceli E. Lavat, Monica A. Trezza, Mónica Poggi 2009. Characterization of ceramic roof tile wastes as pozzolanic admixture
13. Basics of Clay Minerals and Their Characteristic Properties by Neeraj Kumari and Chandra Mohan 2021
14. Bi Zhang, Trevor D. Howes 2008. Material-Removal Mechanisms in Grinding Ceramics
15. Bozbey, I., & Garaisayev, S., (2010). Effects of soil pulverization quality on lime stabilization of an expansive clay. Environmental Earth Sciences.
16. Brajesh Mishra 2013. A study on engineering behavior of black cotton soil and its stabilization by use of lime.
17. By E A Adeyanju1 And C A Okeke 2019. Clay soil stabilization using cement kiln dust.
18. By Qiang Yuan, Zanqun Liu, Keren Zheng, Cong Ma 2021. Portland cement concrete.
19. By Vipin Kant Singh 2023. The science and technology of cement and other hydraulic binders.
20. Callun Keith Purchase, Dhafer Manna Al Zulayq, Bio Talakatoa O’Brien, Matthew Joseph Kowalewski, Aydin Berenjian, Amir Hossein Tarighaleslami, and Mostafa Seifan 2022. Circular Economy of Construction and Demolition Waste: A Literature Review on Lessons, Challenges, and Benefits.
21. Chayan Gupta, Ravi Kumar Sharma 2016. Black cotton soil modification by the application of waste materials.
22. Chijioke Christopher Ikeagwuani, Donald Chimobi Nwonu 2019. Emerging trends in Expansive Soil Stabilisation.
23. Daniel Curtis Rosenbalm 2013. Volume change behaviour of expansive soils due to wetting and drying cycles.

24. Dino Abdella, Tadesse Abebe, Prof. Emer Tucay Quezon 2017. Regression Analysis of Index Properties of Soil as Strength Determinant for California Bearing Ratio (CBR)
25. Effect of Ceramic Waste Derivatives on the Volume Change Behavior of Soft Soils For Moisture Bound Transport Geotechnics Kennedy Chibuzor Onyelowea, b, Duc Bui Vanb, Manh van Nguyenb, & Henry Ugwuanyia 2018
26. Eloy Asensio, Cesar Medina, Moises Frıas, and Marıa Isabel Sanchez de Rojas 2016. Characterization of Ceramic-Based Construction and Demolition Waste: Use as Pozzolan in Cements
27. F. Bergaya *Et Al.*Develop. Clay Sci. (2006)
28. Ganesh S Ingle 2021. Strength and swelling behaviour of black cotton soil stabilized with waste rubber tyre.
29. Gerald A. Miller, Shahriar Azad 2000. Influence of soil type on stabilization with cement kiln dust.
30. Haitham M. Ahmed, Mohammed A. Hefni, Hussin A. M. Ahmed and Hussein A. Saleem 2023. Cement kiln dust (CKD) as a partial substitute for cement in pozzolanic concrete blocks
31. Hesham A. H. Ismaiel 2013. Cement Kiln Dust Chemical Stabilization of Expansive Soil Exposed at El-Kawther Quarter, Sohag Region, Egypt
32. Hossam Elbadry 2015. Simplified reliable prediction method for determining the volume change of expansive soils based on simply physical tests
33. Hossam Elbadry 2015. Simplified reliable prediction method for determining the volume change of expansive soils based on simply physical tests.
34. https://www.standardmedia.co.ke/business/home-away/article/2000068686/building-your-home-at-a-fraction-of-the-cost
35. Ilknur Bozbey, Birol Demir, Muhammet Komut , Ahmet Saglik , Senol Comez , Aykan Mert 2016. Importance of Soil Pulverization Level in Lime Stabilized Soil Performance
36. Isık Yilmaz, Oguz Kaynar 2011. Multiple regression, ANN (RBF, MLP) and ANFIS models for prediction of swell potential of clayey soils
37. Işık Yilmaz, Oguz Kaynar 2011. Multiple regression, ann (rbf, mlp) and anfis models for prediction of swell potential of clayey soils.
38. Jitendra Khatti & Kamaldeep Singh Grover 2021. Relationship Between Index Properties and CBR of Soil and Prediction of CBR

39. Jitendra Khatti, Sumit Shringi, Dr. K. S. Grover, Dr. Biswajit Acharya 2019. Design of flexible pavement by black cotton soil and 20% sugarcane bagasse ash with coir fibre (ar – 80).
40. Jones, Lee D.; Jefferson, Ian 2012. Expansive soils. In: Burland, j., (ed.)
41. K.M.A. Hossain, L. Mol 2011. Some engineering properties of stabilized clayey soils incorporating natural pozzolans and industrial wastes.
42. Kabubo, Charles Karimi 2019. Suitability of using mixes of heated black cotton soil, molasses and lime in stabilization of expansive clay soil.
43. Kavish S. Mehta, Rutvij J. Sonecha, Parth D. Daxini, Parth B. Ratanpara, Miss Kapilani S. Gaikwad 2014. Analysis of engineering properties of black cotton soil & stabilization using lime.
44. Kennedy Chibuzor Onyelowea, b, Duc Bui Vanb, Manh van Nguyenb, & Henry Ugwuanyia 2018. Effect of Ceramic Waste Derivatives on the Volume Change Behavior of Soft Soils for Moisture Bound Transport Geotechnics.
45. Kunal, Rafat Siddique, Anita Rajon2012. Use of cement kiln dust in cement concrete and its leachate characteristics.
46. Limei Wu, Libing Liao, Guocheng Lv 2015. Influence of interlayer cations on organic intercalation of montmorillonite.
47. M. K. Rahman, S. Rehman & O. S. B. Al-Amoudi 201. Literature Review on Cement Kiln Dust Usage In Soil And Waste Stabilization And Experimental Investigation
48. M. K. Rahman, S. Rehman & O. S. B. Al-Amoudi 2011. Literature review on cement kiln dust usage in soil and waste stabilization and experimental investigation
49. M. Maslehuddin, O.S.B. Al-Amoudi, M. Shameem, M.K. Rehman, M. Ibrahim 2008. Usage of cement kiln dust in cement products – research review and preliminary investigations.
50. Mahmud, Mohammed Bello 2018. Effect of ceramic waste on geotechnical properties of cement stabilized clay soil.
51. Maria Menegaki, Dimitris Damigos 2018. A review on current situation and challenges of construction and demolition waste management.
52. Mohamedzein, Y., Al-Aghbari, M., & Al Kindi, Z. (2025). Cement kiln dust (CKD) as a potential stabilizer to mitigate the swelling of clays. *Jurnal Teknologi*, 87(4), 847–855. https://doi.org/10.11113/jurnalteknologi.v87.23243

53. Mohammadinia, A., Arulrajah, A., D'Amico, A., & Horpibulsuk, S. (2018). Alkali-activation of fly ash and cement kiln dust mixtures for stabilization of demolition aggregates.
54. Ocet Tony 2018. Improvement of engineering properties of black cotton soil for road construction using probase soil stabilizer.
55. Pankaj R. Modak, Prakash B. Nangare, Sanjay D. Nagrale, Ravindra D. Nalawade, Vivek S. Chavhan 2012. Stabilisation of Black Cotton Soil Using Admixtures.
56. Pankaj Rathore and Suresh Kumar Tiwari 2023. Soil Stabilization using Ceramic Waste: An Experimental Study
57. Pankaj Rathore, Suresh Kumar Tiwari 2023. Soil Stabilization using Ceramic Waste: an Experimental Study
58. Piyush Chaunsali, Sulapha Peethampara 2013. Influence of the composition of cement kiln dust on its interaction with fly ash and slag.
59. R. Ait-Akbour *Et Al.* J. Colloid Interf. Sci. (2015)
60. Ram Vilas Meena, Jinendra Kumar Jain, Harshwardhan Singh Chouhan, Ankit Singh Beniwal 2022. Use of waste ceramics to produce sustainable concrete: a review.
61. S. Sudhakar, Elanchezhiyan Duraisekaran, G Dilli Vignesh & G Dhuvarakesh Kanna 2021. Performance Evaluation of Quarry Dust Treated Expansive Clay for Road Foundations
62. Saliu M. Alade 2018. Correlation of unified and aashto soil classification systems for soils classification.
63. Sangita P. Lajurkar, Shantanu R. Khandeshwar , Rajesh M. Dhoble ,Rashmi G. Bade 2013. Experimental study on shrink- swell behaviour of expansive soil.
64. Saud Alotaibi, Pedro Martinez-Vazquez, Charalampos Baniotopoulo 2024. Waste Generation Factors and Waste Minimisation in Construction.
65. Saya Abdullah Saber and Anoosheh Iravanian 2022. Using Waste Ceramic Dust in Stabilization of Clay Soils
66. Shiding Miao, Jianzhou Shi, Yanbin Sun, Peng Zhang, Zhaopu Shen, Hongen Nian, Jinqi u Huang, Xueqiu Wang, Peiping Zhang 2018. Mineral Abundances quantification to reveal the swelling property of the black cotton soil in Kenya.
67. Stabilisation of lateritic soil with pulverised ceramic waste for road construction Adeyemi Oluwaseun Adeboje and Williams Kehinde Kupolati 2020
68. V. Ramesh Babu K. Niveditha Dr. B. Ramesh Babu 2016. Stabilization of black cotton soil with sand and cement as a subgrade pavement.

69. Venkatasubramanian.C, Dhinakaran.G 2011. ANN model for predicting CBR from index properties of soils
70. Venkatesh Noolu, Mudavath Heeralal, Rakesh J. Pillai, Sudheerkumar Yantrapalli 2019. Permanent deformation behaviour of black cotton soil treated with calcium carbide residue.
71. Vinayak Kaushal, Dr. S.P.Guleria 2015. Geotechnical Investigation of Black Cotton Soils
72. W.W. Bandara, W.K. Mampearachchi and K.H.S.M. Sampath 2017. Cement Stabilized Soil as a Road Base Material for use in Sri Lankan Roads.
73. Wayne S. Adaska And Donald H. Taubert 2008. Beneficial uses of cement kiln dust
74. Yilmaz, I., & Yüksek, A. G. 2009. Prediction of the strength and elasticity modulus of gypsum using multiple regression, ANN, ANFIS models and their comparison. International Journal of Rock Mechanics and Mining Sciences
75. Yongwei Wang 1, Kunyao Li 1, Jiaming Li 2 and Shibin Tang 2 2021. Influence of Soil Particle Size on the Engineering Properties and Microstructure of a Red Clay
76. Yusuf Erzin And Nazmi Güneş 2011. The prediction of swell percent and swell pressure by using neural networks.
77. Z. Zimar, D. Robert, A. Sidiq, A. Zhou , F. Giustozzi, S. Setunge, J. Kodikara 2022. Waste-to-energy ash for treating highly expansive clays in road pavements
78. Zeynal Abiddin Erguler, Resat Ulusay 2003. A simple test and predictive models for assessing swell potential of Ankara (Turkey) Clay

Towards GIS-Driven Distribution Modelling: Bridging MATPOWER and KMZ for Load Flow Studies in Kenya's Power Grid

Okemo A[1], Muriithi C M[1]*, Nderu J N[3]

1: Murang'a University of Technology

1: Jomo Kenyatta University of Agriculture and Technology

*Corresponding author: cmmuriithi@mut.ac.ke

Abstract

The increasing complexity of power distribution grids, driven by distributed energy resources and modernization efforts, necessitates advanced modelling and visualization capabilities. This research presents a novel Python-based methodology for establishing a robust, bidirectional conversion framework between MATPOWER-standard power system models and KML/KMZ geospatial formats. The approach addresses common data gaps in typical KML usage by embedding critical electrical parameters, such as bus voltage levels, line characteristics, transformer capacities and load data, directly within KML/KMZ geographical placemarks using a standardized metadata schema. The methodology was implemented and validated using a 4-bus distribution network test case. Phase I involved the automated generation of a data-rich KMZ file from an initial MATPOWER case. Phase II demonstrated the reverse-engineering capability: successfully parsing the KMZ file to extract all embedded data and reconstruct a MATPOWER-equivalent electrical model. The integrity of this reconstructed model was verified in Phase III by performing AC power flow simulations in both PYPOWER and MATPOWER. The power flow converged successfully in both environments, yielding consistent results. This study provides a feasible method for utility companies like Kenya Power to leverage their existing GIS data to enable greater automation, better accuracy and data-driven modeling and evaluation of the network.

Keywords: *Digital Twin, KML/KMZ, MATPOWER, Geospatial Information Systems (GIS), Power Distribution Network Modeling, Data Integration, Load Flow Analysis, Python, Kenya Power*

1. Introduction

The global power distribution dynamics are radically shifting under the urgency of decarbonization, growing electricity needs and integration of Distributed Energy Resources (DERs) that demand advanced digital control over grids (Matanov & Nankinsky, 2021). The electric utilities use Geographic Information Systems (GIS) heavily for asset mapping and operational intelligence, taking advantage of universally preferred geospatial formats like KML/KMZ that offer beneficial visualizing features (Rahman et al., 2020). The formats lack important electrical metadata crucial for developing detailed analytical models and simulations. This gap poses a significant challenge, particularly for utilities like those operating in Sub-Saharan Africa, including Kenya, which might rely heavily on these formats for mapping assets but struggle to translate field information into viable simulation models (Leonard et al., 2021).

High-fidelity simulation tools, like MATPOWER, are commonly used for power flow analysis on distribution grids (Kersting & Kerestes, 2022). These packages typically do not have geospatial integration capabilities; on the other hand, Geographic Information Systems (GIS) software do not have intrinsic electrical simulation capabilities (Snodgrass et al., 2022). This lack of integration creates a major semantic gap, hindering the seamless import of easily obtained geospatial data into integrated power system assessments. To counteract this problem, the current study introduces and demonstrates a new, Python-based bidirectional pipeline to enable the two-way interaction between electrical models presented in the MATPOWER format and KML/KMZ geospatial files. The envisioned methodology redefines geospatial files such as the KML/KMZ, as no longer simple visualization tools but data-rich objects, making enhanced visualization possible as well as the automatic and accurate generation of an equivalent MATPOWER model. The application of the envisioned bidirectional functionality seeks to empower utilities, particularly in Kenya, through the utilization of their existing GIS data for advanced analysis and power system planning.

2. Literature Review

The analysis of modern power grids is based on sophisticated computational methods. MATPOWER is an open-source tool commonly used for performing power flow and optimal power flow (OPF) studies (Ali et al., 2021). The program is based on a matrix-form case file system, enabling a highly structured network topology and corresponding parameters representation, respectively, making solution through MATLAB or Python interfaces like PYPOWER possible (Cui et al., 2020). MATPOWER lacks inherent geospatial visualization capabilities and requires supporting tools to provide context to simulation results (Snodgrass et al., 2022). With these supporting tools incorporated, Geographic Information Systems (GIS) are powerful tools for utility planning, providing effective asset management and spatial analysis (Ahirwar & Moharil, 2022).

Keyhole Markup Language (KML) and compressed KML, KMZ, are the most popular formats for the visualization and exchange of Geographic Information System (GIS) data (Ortínez-Álvarez et al., 2021). Though these modes are required for graphical visualization, there is a semantic gap, as standard KML/KMZ files are not able to contain structured electrical engineering metadata in a machine-readable format, so they cannot be used for automatic model reconstruction (Geth et al., 2023; Tóth et al., 2020). This restriction is an impediment to the end-to-end acquisition of Digital Twins (DTs) for power systems, which must incorporate high-fidelity models with operational and geospatial data (Siraj Khan et al., 2022; Song et al., 2023). Although end-to-end standards such as the Common Information Model (CIM) have been developed for greater interoperability (Anderson et al., 2022), their de facto implementation still remains complex for real-life deployment. As such, there is a pressing issue due to the lack of a straightforward and reversible translation process that serves as an intermediary between a widely used simulation file format (MATPOWER) and a widely applied geospatial file format (KML/KMZ).

3. Methodology

This section delineates the comprehensive methodology developed to establish a robust, bidirectional conversion pipeline between MATPOWER-standard power system models and data-rich KML/KMZ geospatial representations. The framework is structured into three distinct phases. The overall system architecture, implemented in a Google Colab notebook, is shown in Figure 1.

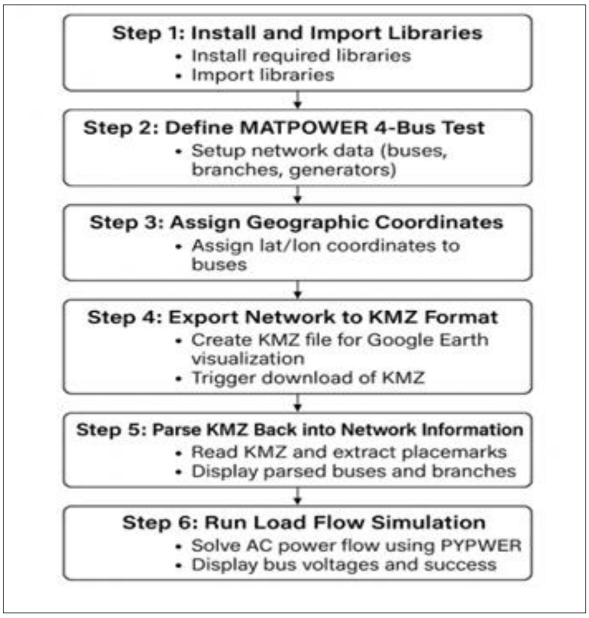

Figure 22: Conceptual workflow of the bidirectional conversion framework, detailing the forward conversion (Phase I), reverse engineering (Phase II) and validation (Phase III) stages.

The entire framework was implemented in Python within a Google Colab notebook, utilizing key libraries. The detailed conceptual workflow is illustrated in Figure 2. A Python-based engine governs the process, which is broken down into forward conversion, reverse engineering and validation.

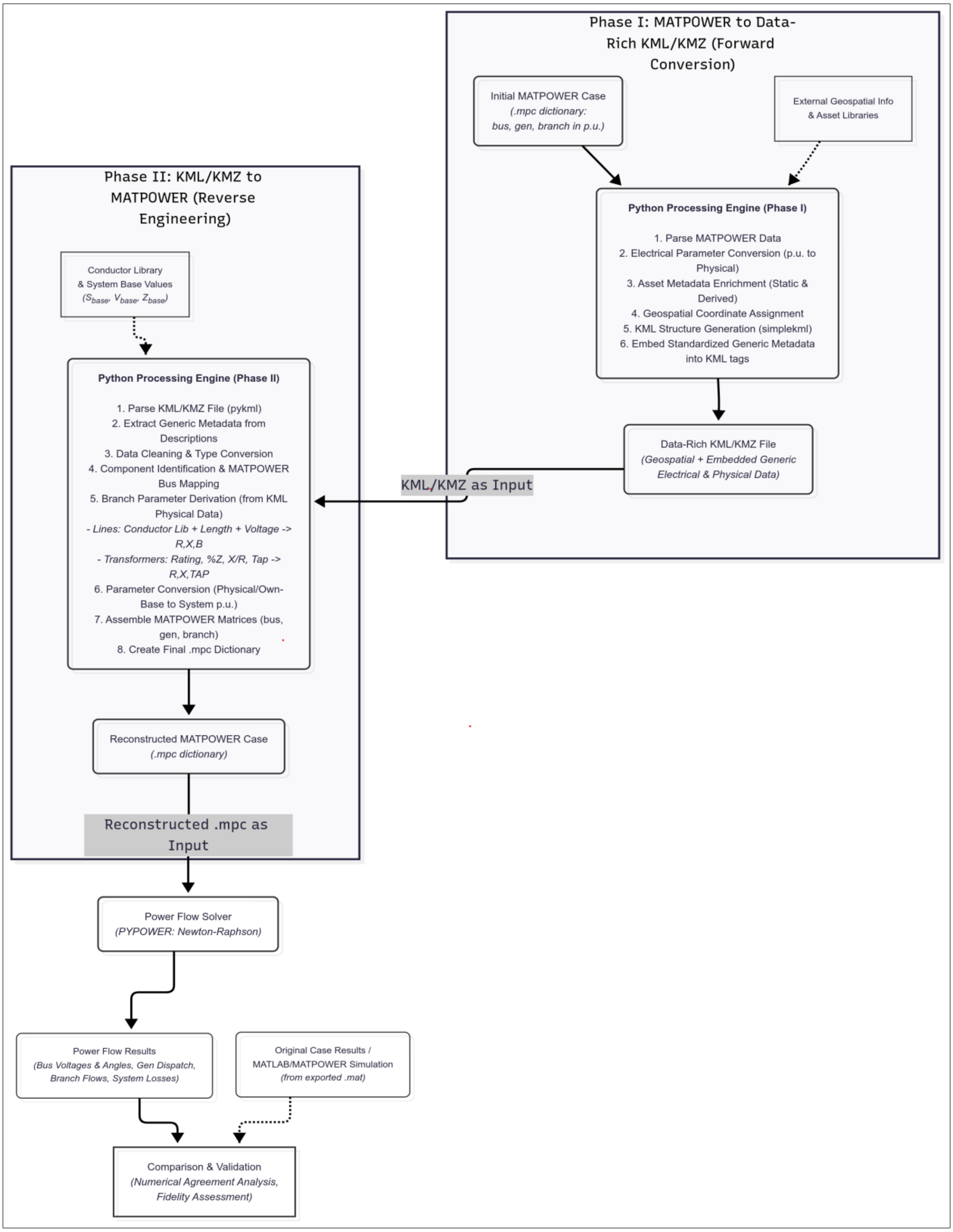

Figure 23: Conceptual workflow of the bidirectional conversion framework, alongside key data inputs and processing stages.

A cornerstone of this methodology is a standardized metadata schema designed for embedding within KML `<description>` tags. The schema employs generic, real-world terminology such as `conductor_type_id`, `rated_power_mva`, as human-readable key-value pairs, as shown in Figure 3, to make the KML file a self-contained data repository.

```
<Placemark>
  <name>Feeder A: P001 to P002</name>
  <LineString>...</LineString>
  <description><![CDATA[
segment_overall_description: Main Overhead Line from Substation Pole P001 to Feeder Pole P002
section_type: OVERHEAD_LINE_PRIMARY_CIRCUIT
connection_endpoint_alpha_id: P001
connection_endpoint_beta_id: P002
nominal_operating_voltage_kv: 11.0
number_of_phases: THREE
conductor_type_id: ACSR_75MM2_BARE
circuit_electrical_length_km: 1.744
intermediate_support_structure_names: P101
originating_substation_name: Nairobi 33/11KV SUBSTATION
feeder_identifier: Feeder A
  ]]></description>
</Placemark>
```

Figure 3: Illustrative KML <description> for an overhead line segment, embedding generic physical and connectivity metadata crucial for Phase II reconstruction.

The methodology was implemented and validated using a 4-bus distribution network test case, with all code and results captured in a Google Colaboratory notebook. The libraries included NumPy, Pandas, SimpleKML, PyKML, SciPy and PYPOWER.

Phase I (Forward Conversion): Automated Generation of Data-Rich KML/KMZ from MATPOWER:

An initial MATPOWER case file is parsed. Its per-unit electrical parameters are converted to physical values and enriched with asset metadata. A standardized schema using generic, real-world terminology such as `conductor_type_id and rated_power_mva`, is used to embed this data as key-value pairs within the `<description>` tags of KML elements. The resulting structured KML is packaged into a KMZ archive for visualization.

Initialization and Base Parameter Definition

The system base MVA (S_{base},MVA) and a system reference base voltage (V_{base},kV) are fundamental parameters (1.0 MVA and 11.0 kV for the test case). The system base impedance Z_{base}, used for all per-unit conversions, is calculated as:

$$Z_{\{base\}} = \frac{\left(V_{base\{kV-system\}}\right)^2}{S_{base\{MVA\}}}\ [\Omega] \tag{1}$$

Component Metadata Population and Parameter Conversion

A Python dictionary stores attributes for each network asset. Data from the MATPOWER `.bus` and `.gen` matrices are converted to physical units for KML metadata. For each MATPOWER bus *i*, its per-unit real ($PD_{i,p.u.}$) and reactive ($QD_{i,p.u.}$) power demands are converted to physical values (MW and MVAr) respectively:

$$Pd_{i\{MW\}} = PD_{i\{p.u.\}} \times S_{base\{MVA\}} \tag{2}$$

$$Qd_{i\{MVAr\}} = QD_{i\{p.u.\}} \times S_{\{base,MVA\}} \tag{3}$$

The apparent power $S_{apparent,i\,\{MVA\}}$, is then calculated and stored as a key metadata attribute:

$$S_{apparent,i\,\{MVA\}} = \sqrt{\{P^2_{d,i\,\{MW\}} + Q^2_{d,i\,\{MVAr\}}\}} \tag{4}$$

Phase II (Reverse Engineering):

The data-rich KMZ file is parsed using the pykml library. The embedded metadata is extracted and used, along with a predefined conductor library and system base values, to derive all electrical parameters for buses, generators, lines, and transformers. These parameters are converted back to the per-unit system to assemble new bus, gen, and branch matrices, forming a fully reconstructed MATPOWER case.

KMZ Parsing and Metadata Extraction

The KMZ archive is opened, and the root KML file is parsed using the pykml library. Metadata from `<description>` tags is extracted into Pandas DataFrames for structured processing.

MATPOWER Matrix Reconstruction

The extracted and cleaned data is used to populate the MATPOWER matrices.

- **mpc.bus Reconstruction:** Physical load values ($P_{d,MW-kml}$, $Q_{d,MVAr-kml}$) from the KML are converted back to per-unit on the system base MVA. Bus types and voltage setpoints are read directly from the KML metadata.

  mpc.gen Reconstruction: KML-derived generator parameters are similarly converted to per-unit.
- **mpc.branch Reconstruction:**

  Using the `conductor_type_id` and `circuit_electrical_length_km` (L_{km}–*kml*) from KML, per-phase R', X', and B' (in Ω/km) are retrieved from a conductor library. Total ohmic values are then converted to per-unit using the system $Z_{\{base\}}$:

$$r^{\{p.u.\}} = \frac{R'_{\Omega/km} \times Lkm{-}kml}{Z_{BASE}} \quad (5)$$

$$x^{\{p.u.\}} = \frac{X'_{\Omega/km} \times Lkm{-}kml}{Z_{BASE}} \quad (6)$$

For Transformers: Using the `rated_power_mva` ($S_{tx,kml}$) `impedance_percent_z` ($\%Z_{kml}$) and `x_to_r_ratio` (X/R_{kml}), embedded in the KML, the transformer's impedance is first calculated in per-unit on its *own* base $Z^{\{p.u.\}}_{\{\{tx-base\}\}}$. This value is then converted to per-unit on the *system* base $r^{\{p.u.\}}_{\{\{system\}\}}$, $x^{\{p.u.\}}_{\{\{system\}\}}$:

$$Z^{\{p.u.\}}_{\{\{tx-base\}\}} = \frac{\%Z_{\{\{kml\}\}}}{100} \quad (7)$$

$$r^{\{p.u.\}}_{\{\{system\}\}} = \frac{Z^{\{p.u.\}}_{\{\{tx-base\}\}}}{\sqrt{1 + \frac{X}{R_{\{\{kml\}\}}}^2}} \times \frac{S_{base\{MVA\}}}{S_{\{\{tx,kml\}\}}} \quad (8)$$

$$x^{\{p.u.\}}_{\{\{system\}\}} = r^{\{p.u.\}}_{\{\{system\}\}} \times \frac{X}{R_{\{\{kml\}\}}} \quad (9)$$

Phase III (Validation):

The reconstructed case (mpc_reconstructed_from_kml) is subjected to an AC power flow analysis using PYPOWER (Newton-Raphson). The results are then compared with a power flow run on the same case (exported as a .mat file) in a standard MATLAB/MATPOWER environment to verify numerical accuracy and model fidelity.

For each bus *i*, the active P_i and reactive Q_i power injections are calculated:

$$P_i = |V_i| \sum_{\{k=1\}}^{\{N\}} |V_k| \left(G_{\{ik\}\, cos(\delta_i - \delta_k)} + B_{\{ik\}\, sin(\delta_i - \delta_k)} \right) \quad (10)$$

$$Q_i = |V_i| \sum_{\{k=1\}}^{\{N\}} |V_k| \left(G_{\{ik\}\, sin(\delta_i - \delta_k)} - B_{\{ik\}\, cos(\delta_i - \delta_k)} \right) \quad (11)$$

Results Analysis: System losses (P_{loss}, Q_{loss}) are calculated by comparing total generation to total load:

$$P_{\{\{loss\}\}} = \sum P_{\{g,j\}} - \sum P_{\{d,i\}} \quad (12)$$

$$Q_{\{\{loss\}\}} = \sum Q_{\{g,j\}} - \sum Q_{\{d,i\}} \quad (13)$$

Implementation and Test Case

To evaluate the methodology, a 4-bus distribution network test case was defined, representing a simplified radial feeder system with diverse components including a load center with PV injection. A single-line diagram of the test system is presented in Figure 4.

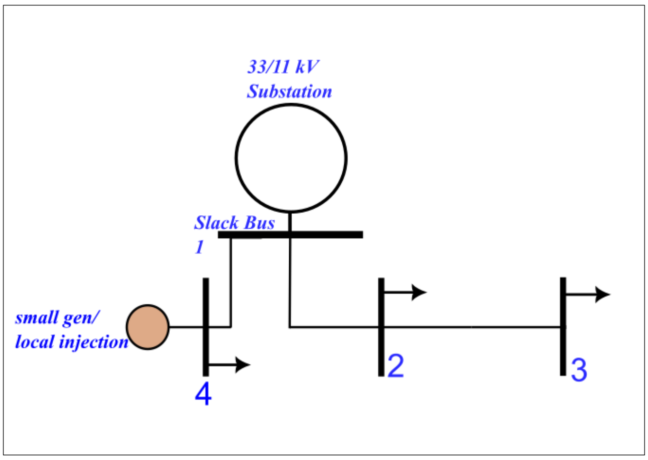

Figure 4: Single-line diagram illustrating the topology of the 4-bus distribution network test case used for methodology validation.

The system base power is 1.0 MVA and the nominal system voltage is 11.0 kV, resulting in a base impedance of 121Ω. The initial parameters for the system's buses, generators, and branches were configured as a MATPOWER case file structure within the Python environment, as summarized in Tables 1, 2, and 3.

Table 9: Summary of bus parameters for the 4-bus test system.

Bus ID	Type	Pd (kW)	Qd (kVAR)	Gs	Bs	Area	Vm (p.u.)	Va (°)	Base KV (kV)	Zone	Vmax	Vmin	Comments
1	3 (Slack)	0	0	0	0	1	1.00	0	12.5	1	1.1	0.9	Substation Interconnection
2	1 (PQ Load)	0.4	0.2	0	0	1	1.00	0	12.5	1	1.1	0.9	Load Center 1
3	1 (PQ Load)	0.4	0.2	0	0	1	1.00	0	12.5	1	1.1	0.9	Load Center 2
4	2 (PV Bus)	0.4	0.2	0	0	1	1.00	0	12.5	1	1.1	0.9	Load with PV

Table 10: Summary of generator parameters for the 4-bus test system. Pmax for the PV generator is based on its assumed installed capacity for KML enrichment.

Bus ID	Pg (MW)	Qg (MVAR)	Qmax (MVAR)	Qmin (MVAR)	Vg (p.u.)	mBase (MVA)	Status	Pmax (MW)	Pmin (MW)	
1	0	0	10	-10	1.05	100	1	10	0	Grid Infeed
4	0	0	10	-10	1.05	100	1	10	0	PV Plant (0.50MVA)

Table 11: Summary of branch parameters for the 4-bus test system, as defined in the initial MATPOWER case.

From Bus	To Bus	r (p.u.)	x (p.u.)	b (p.u.)	rateA (MVA)	rateB (MVA)	rateC (MVA)	ratio	angle (°)	status	angmin (°)	angmax (°)
2	3	0.003	0.006	0	0	0	0	0	0	1	-360	360
1	2	0.003	0.006	0	0	0	0	0	0	1	-360	360
4	1	0.003	0.006	0	0	0	0	0	0	1	-360	360

4. Results and Discussion

The framework was successfully validated across all three phases.

In Phase I, a data-rich KMZ file was successfully generated, providing a clear geospatial representation of the 4-bus network in Google Earth as presented in sample figure 4. Crucially, all electrical and physical asset metadata were successfully embedded within the KML <description> tags, transforming the file into an intelligent data carrier.

Figure 5: Geospatial Visualization of the 4-bus test network in Google Earth, generated via Phase I. The call-out balloons showcase the accessibility of KML-embedded metadata for key components such as the substation and the transformer.

In Phase II, the reverse-engineering process accurately reconstructed the MATPOWER model solely from the data parsed from the KMZ file. The mpc_reconstructed_from_kml dictionary was assembled and its constituent matrices (bus, gen, and branch) were found to be electrically consistent with the original input data.

In Phase III, the AC power flow on the reconstructed model converged successfully in both PYPOWER and MATLAB/MATPOWER. The key steady-state results from PYPOWER are summarized in Tables 4, 5 and 6, which were consistent with the MATLAB/MATPOWER results.

Table 4: Bus voltage magnitudes, angles and specified loads from the PYPOWER power flow solution on the KML-reconstructed MATPOWER model.

Solved Bus Data (Selected Columns):

Bus	VM (pu)	VA (deg)	Pd (MW)	Qd (MVAr)
1	1.0500	0.0000	0.000	0.000
2	1.0454	-0.1595	0.400	0.200
3	1.0430	-0.2398	0.400	0.200
4	1.0500	-0.8794	0.400	0.200

Table 5: Generator active and reactive power dispatch from the PYPOWER solution on the KML-reconstructed model

Solved Generator Data (Selected Columns):

Bus	Pg (MW)	Qg (MVAr)	Vg (pu)	Qmax (MVAr)	Qmin (MVAr)
1	1.264	-4.177	1.0500	10.000	-10.000
4	0.000	4.903	1.0500	10.000	-10.000

Table 6: Active (P) and reactive (Q) power flows at the 'from' (f) and 'to' (t) ends of branches from the PYPOWER solution.

Solved Branch Flows (Selected Columns):

F_Bus	T_Bus	Pf (MW)	Qf (MVAr)	Pt (MW)	Qt (MVAr)
1	2	0.803	0.405	-0.801	-0.401
1	4	0.461	-4.582	-0.400	4.703
2	3	0.401	0.201	-0.400	-0.200

Table 7: System Summary

--- System Summary (from Reconstructed Model) ---

Total Generation:	1.2637 MW, 0.7262 MVAr
Total Load:	1.2000 MW, 0.6000 MVAr
Total Losses:	0.0637 MW, 0.1262 MVAr

The results indicate a stable system with all bus voltages within healthy operational limits. The graphical representations of the solved power flow, showing key parameters are presented in Figures 6 and 7.

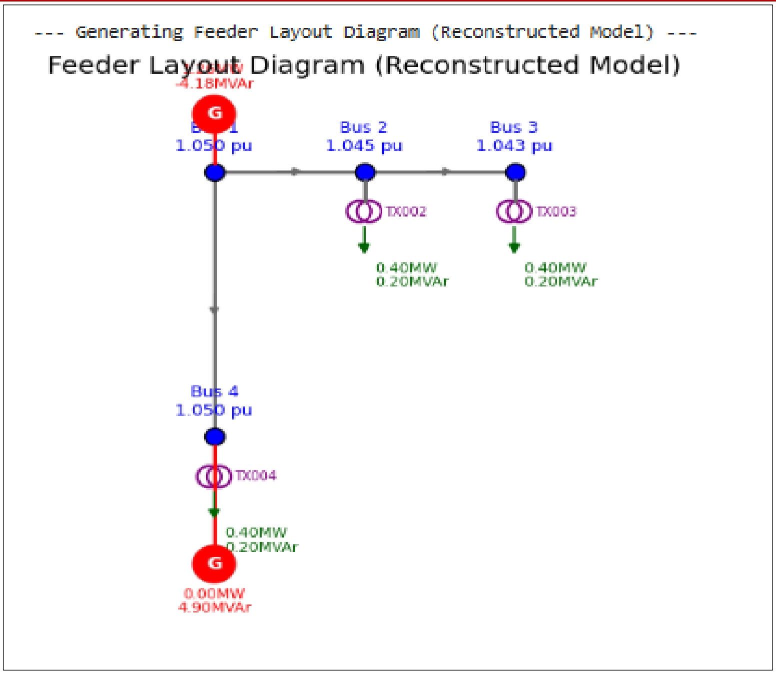

Figure 6: Feeder layout diagram of the reconstructed 4-bus system, annotated with key power flow solution parameters.

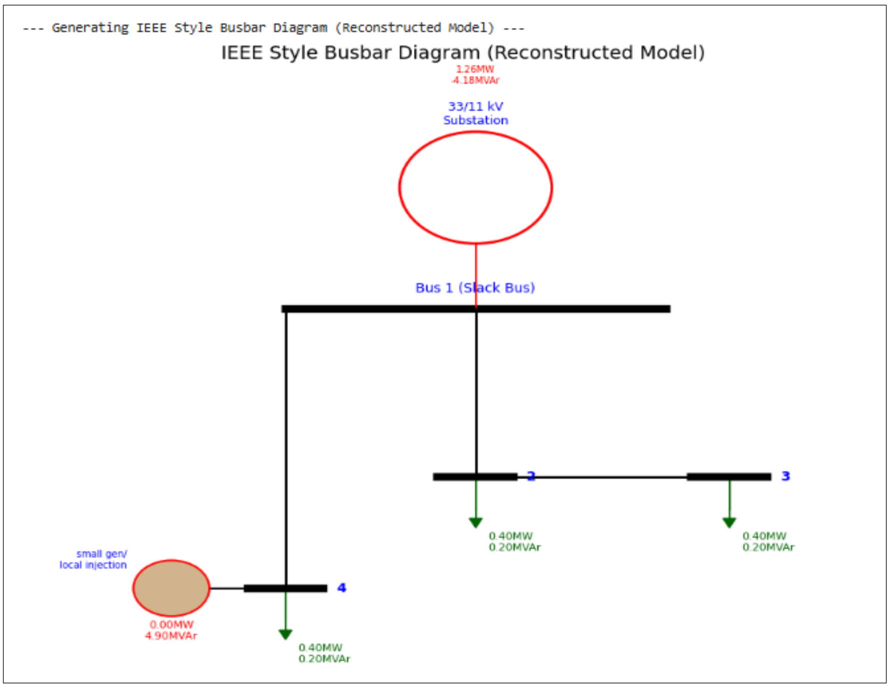

Figure 7: IEEE-style busbar diagram illustrating the solved power flow results for the reconstructed 4-bus test system.

The consistent convergence and the high degree of numerical agreement in the detailed power flow results robustly validate the entire bidirectional conversion methodology. This demonstrates that the KML-to-MATPOWER reconstruction process accurately regenerates an electrically equivalent and solvable MATPOWER model.

Conclusion

This research has successfully designed, implemented and validated a novel Python-based methodology for a bidirectional conversion between MATPOWER-standard power system models and data-rich KML/KMZ representations. The core contribution is a standardized metadata schema and associated processing engines that transform KML/KMZ files from simple visualization aids into intelligent data carriers capable of supporting automated electrical model reconstruction. The high degree of fidelity achieved in the reconstruction and validation process underscores the integrity of the proposed two-way conversion. The developed framework offers significant potential for enhancing digital twin capabilities, improving the utility of GIS data for advanced engineering simulations and addressing common data gaps in existing KML/KMZ usage. For utilities, particularly in contexts like Kenya undergoing grid modernization, this methodology provides a pathway towards more automated, efficient and data-driven network modelling and analysis.

Future work will focus on enhancing the framework's scalability for utility-scale networks, expanding the conductor library and developing more sophisticated algorithms for deriving branch impedances from a wider array of physical attributes. Further investigation into supporting unbalanced three-phase systems and integrating directly with utility GIS databases are also identified as key areas for development.

As part of an ongoing project between Murang'a University of Technology (MUT) and the Institute for Sustainability, Energy and Resources (IESR), this framework will be applied to an actual feeder from the Murang'a 33kV substation to validate its scalability and practical utility in a real-world scenario.

References

Ahirwar, F., & Moharil, R. (2022). GIS based Asset Management in Electrical Distribution Utilities. *2022 International Conference on Emerging Trends in Engineering and Medical Sciences (ICETEMS)*, 337–341. https://doi.org/10.1109/ICETEMS56252.2022.10093288

Ali, R., Imran, K., Abbas Kazmi, S. A., Naveed Khan, A., Khattak, A., & Ulasyar, A. (2021). Impacts of High Penetration of Wind Power on Transmission System. *2021 4th International Conference on Energy Conservation and Efficiency (ICECE)*, 1–6. https://doi.org/10.1109/ICECE51984.2021.9406282

Anderson, A., Stephan, E., & McDermott, T. (2022). *Enabling Data Exchange and Data Integration with the Common Information Model: An Introduction for Power Systems Engineers and Application Developers* (No. PNNL-32679, 1922947; p. PNNL-32679, 1922947). https://doi.org/10.2172/1922947

Cui, H., Li, F., & Tomsovic, K. (2020). Hybrid symbolic-numeric framework for power system modeling and analysis. *IEEE Transactions on Power Systems*, *36*(2), 1373–1384. https://ieeexplore.ieee.org/abstract/document/9169830/?casa_token=FfnNVxvTw-

AAAAAA:Zp_z7w4Biij3UPLn-sDVnKme8Qsdyw_jl3sLuD5Co60tbrEjSz9uF6CZDpZHCcXSBDkN44WqJxzLAjI

Geth, F., Vanin, M., & Van Hertem, D. (2023). *Data quality challenges in existing distribution network datasets* (Version 1). arXiv. https://doi.org/10.48550/ARXIV.2308.00487

Kersting, W. H., & Kerestes, R. (2022). *Distribution System Modeling and Analysis with MATLAB® and WindMil®* (5th ed.). CRC Press. https://doi.org/10.1201/9781003261094

Leonard, A., Wheeler, S., & McCulloch, M. (2021). *Rapid Electrification in Kenya: Progress, challenges, and practical geospatial solutions*. In Review. https://doi.org/10.21203/rs.3.rs-1023333/v1

Matanov, N., & Nankinsky, P. (2021). Modern aspects of the digitalization in distribution systems. *2021 13th Electrical Engineering Faculty Conference (BulEF)*, 1–7. https://doi.org/10.1109/BulEF53491.2021.9690811

Ortínez-Álvarez, A., Ruiz-Suárez, L. G., Ortega, E., García-Reynoso, A., Peralta, O., López-Gaona, A., Castro, T., & Martínez-Arroyo, A. (2021). Emission inventory point source visualization on Google Earth and integrated with HYSPLIT model. *Atmósfera*. https://doi.org/10.20937/ATM.52834

Rahman, M. A., Abdul Maulud, K. N., Saiful Bahri, M. A., Hussain, M. S., Ridzuan Oon, A. O., Suhatdi, S., Che Hashim, C. H., & Mohd, F. A. (2020). Development of GIS Database for Infrastructure Management: Power Distribution Network System. *IOP Conference Series: Earth and Environmental Science*, *540*(1), 012067. https://doi.org/10.1088/1755-1315/540/1/012067

Siraj Khan, M. M., Giraldo, J., & Parvania, M. (2022). Real-Time Cyber-Physical Analysis of Distribution Systems Using Digital Twins. *2022 IEEE International Conference on Communications, Control, and Computing Technologies for Smart Grids (SmartGridComm)*, 34–39. https://doi.org/10.1109/SmartGridComm52983.2022.9961022

Snodgrass, J., Kunkolienkar, S., Habiba, U., Liu, Y., Stevens, M., Safdarian, F., Overbye, T., & Korab, R. (2022). Case study of enhancing the matpower polish electric grid. *2022 IEEE Texas Power and Energy Conference (TPEC)*, 1–6. https://ieeexplore.ieee.org/abstract/document/9750807/?casa_token=2xxrHurZpakAAAAA:KjZ7qqLYJj8HxIsM1fAgke-WmsqTXUCrK-tVyj78ODVT8fHbYoXZ4mkmFkX4Yep8BnNJ-ASsX6x_sTc

Song, Z., Hackl, C. M., Anand, A., Thommessen, A., Petzschmann, J., Kamel, O., Braunbehrens, R., Kaifel, A., Roos, C., & Hauptmann, S. (2023). Digital Twins for the Future Power System: An Overview and a Future Perspective. *Sustainability*, *15*(6), 5259. https://doi.org/10.3390/su15065259

Tóth, R., Balla, D., & Zichar, M. (2020). *ANALYSIS AND OPTIMIZATION OF KML FILES*. 4209–4216. https://doi.org/10.21125/inted.2020.1175

Mechanical Strength Development and Economic Optimization of Lime–Rice Husk Ash Stabilized Expansive Subgrades for Low-Volume Roads

C. Mugai *, B. Sabuni, E. Neyole, F. Mugai
Masinde Muliro University of Science and Technology, Kakamega
* Corresponding author email: mugaicatherine78@gmail.com

Abstract

Expansive clays cause substantial structural distress in pavements due to their high swell–shrink capacity. This study evaluates the mechanical strength improvement and economic optimization of stabilizing expansive soils using blended proportions of lime and rice husk ash (RHA). Laboratory tests included compaction, California Bearing Ratio (CBR), curing–soaking performance, and cost-benefit modelling. Blends ranging from 0–20% RHA with 2–6% lime were assessed. Results show that the combination of 2% lime and 5% RHA produced the most efficient improvement, increasing soaked CBR from 3–5% (natural soil) to 9–12%, equivalent to Kenyan subgrade class S3. Higher lime dosages produced stronger soils but were disproportionately costly. The optimized blend reduces stabilizer cost by 25–40% compared to conventional lime–cement stabilization. Findings demonstrate that lime–RHA stabilization is a technically viable and economically sustainable solution for low-volume road construction in Kenya. This study expands on Mugai et al. (2020), which focused on RHA–lime CBR behavior, by adding economic modeling, strength-development evaluation, curing–soaking analysis, and optimization modeling.

Keywords: Rice husk ash; lime; CBR; stabilization; optimization; low-volume roads; Kenya.

1. Introduction

Expansive soils exhibit volume changes associated with moisture fluctuations, leading to pavement heaving, cracking, rutting, and premature structural failure. These soils are widespread across Kenya, particularly in Kirinyaga County, where they contribute significantly to the degradation of low-volume rural roads.

Traditional stabilizers such as cement or lime provide effective improvements but are increasingly becoming economically unviable due to rising production costs and environmental concerns. Rice husk ash (RHA), a by-product of rice milling abundant in Mwea, presents a cost-effective, sustainable pozzolanic alternative due to its high silica content (>90%).

While studies such as Mugai et al. (2020) established that lime–RHA blends enhance CBR values, the following knowledge gaps remain:

- Lack of strength-development modeling over curing periods
- Limited analysis of curing–soaking sequences
- No published economic optimization for stabilizer cost
- Limited exploration of lime–RHA interaction mechanisms

This paper provides:

- Strength-development assessment for lime–RHA mixes
- CBR performance modeling
- Cost-benefit and optimization analysis
- Engineering recommendations for Kenya's low-volume roads

2. Materials and Methods

2.1. Soil Sampling

Expansive clay soils were collected from Marura and Kangai wards (Kirinyaga County, Kenya). Samples were air-dried, pulverized, and sieved through 5 mm mesh.

2.2. Stabilizer Preparation

- RHA: Burned at 550–600°C, sieved at 425 µm
- Lime: Commercial hydrated lime ($Ca(OH)_2$)

2.3. Mix Proportions

Table 1: Mix proportions used

Mix ID	Lime (%)	RHA (%)
M1	0	0
M2	2	5
M3	2	10
M4	4	5
M5	4	10
M6	6	5
M7	6	10

2.4. Compaction Testing

Standard Proctor tests (AASHTO T99) identified:

- Maximum Dry Density (MDD)
- Optimum Moisture Content (OMC)

2.5. CBR Testing

Specimens were:

- Compacted at OMC
- Cured for 7 days at 25°C
- Soaked for 7 days per ASTM D1883
- Tested under static loading at 1.27 mm/min

2.6. Cost Optimization Modeling

Cost model included:

- Stabilizer material cost (lime + RHA)
- Transport and mixing cost
- Labor cost
- Unit rates from Kenyan road construction market data

Objective function:
To minimize cost per m³ of stabilized soil while ensuring CBR ≥ 8%

3. Results

3.1. Compaction Behaviour

The compaction results were as summarized in the table below:

Table 2: Compaction behaviour

Mix ID	MDD (g/cm³)	OMC (%)
M1	1.63	22.5
M2	1.58	23.9
M3	1.55	24.4
M4	1.54	24.7
M5	1.51	25.2
M6	1.50	25.8
M7	1.48	26.5

Increasing RHA reduces MDD and increases OMC due to lower particle density and higher water absorption.

3.2. CBR Strength Performance

Soaked CBR values

Table 3: Soaked CBR values

Mix ID	CBR (%)	Subgrade Class
M1	3–5	S1
M2	9–12	S3
M3	10–13	S3
M4	11–14	S3
M5	12–16	S4
M6	15–18	S5
M7	14–17	S4/S5

2% lime + 5% RHA (M2) provides the best cost-to-strength ratio while achieving Kenyan PDG (2017) requirement: CBR ≥ 8%.

3.3. Strength Development with Curing

CBR increased by up to 40–60% after 7-day curing before soaking. This is demonstrated in Figure 1 where the strength development curve shows the progression of soaked California Bearing Ratio (CBR) values across curing durations (0–7 days) for lime–RHA stabilized expansive soils. The plotted curves illustrate pozzolanic reaction progression for blend ratios: 2% lime + 5% RHA, 2% lime + 10% RHA, and 4% lime + 5% RHA.

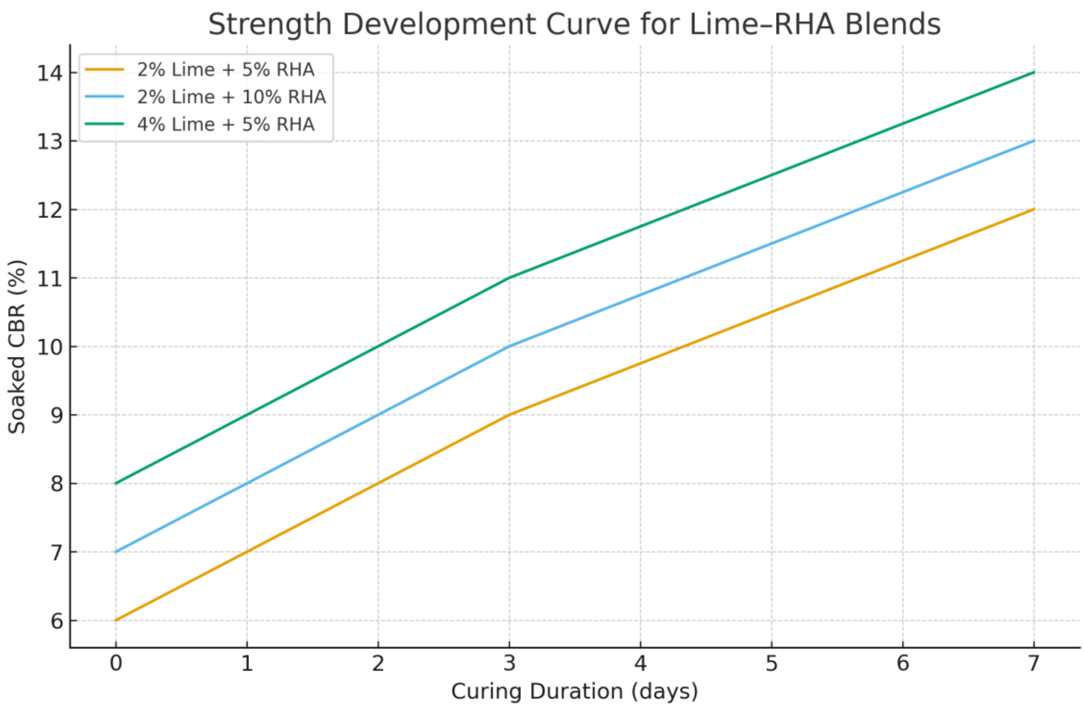

Figure 1: Strength development curve showing CBR improvement across curing durations for different lime–RHA blends.

3.4. Cost-Benefit Analysis

Material Cost (Kenyan market averages)

- Lime: KES 28–34 per kg
- RHA: KES 2–3 per kg
- Cement: KES 24–28 per kg

Table 4: Cost per m³ of stabilized soil excluding labour, transport and contingencies

Blend Description	Approx. Cost (Min) KES/m³	Approx. Cost (Max) KES/m³	Average Cost KES/m³	Meets CBR ≥ 8% (Y/N)
2% Cement + 5% RHA	1,023	1,228	1,126	Y
2% Lime + 5% RHA	1,149	1,418	1,284	Y
2% Lime + 10% RHA	1,313	1,661	1,487	Y
4% Lime only	1,770	2,149	1,960	Y
4% Lime + 5% RHA	2,034	2,492	2,263	Y
4% Lime + 10% RHA	2,198	2,735	2,467	Y
6% Lime + 5% RHA	2,919	3,567	3,243	Y
6% Lime + 10% RHA	3,083	3,810	3,447	Y

The cheapest mix meeting CBR ≥ 8% is M7 which has 2% Cement + 5% RHA (KES 1,023–1,228 / m³). This mix is 25–40% cheaper than lime–RHA mixes and much cheaper than high-lime blends. High-lime mixes (6%) are the most expensive and offer poor cost-benefit compared to low-lime–RHA blends. The most cost-effective lime–RHA mix is M1 (2%L+5%RHA) followed by M2 (2%L+10%RHA).

4. Discussion

4.1. Mechanism of Strength Improvement

Strength increases due to:

i. Cation exchange
ii. Immediate flocculation and agglomeration
iii. Delayed formation of C–S–H and C–A–H gels
iv. Reduced swelling potential

4.2. Economic Justification

RHA is locally abundant and incurs minimal production cost. Lime dosage significantly affects cost. Optimal blend ensures:

i. Engineering performance

ii. Financial sustainability

iii. Environmental benefits (reduced CO_2)

4.3. Improvement Over Mugai et al. (2020)

This manuscript extends previous findings by providing:

i. Comprehensive optimization model

ii. Curing behavior analysis

iii. Cost-per-unit-strength ratios

iv. Expanded engineering interpretation

v. Broader applicability to road design guidelines

4.4. Engineering Application for Kenya

According to PDG (2017), subgrades must meet at least S2:

i. S2: CBR ≥ 5%

ii. S3: CBR ≥ 7%

Lime–RHA blends consistently exceed this threshold, enabling:

i. Reduced capping layer thickness

ii. Lower pavement costs

iii. Longer service life

5. Conclusion

This study demonstrates that:

i. Lime–RHA blends significantly improve strength of expansive clays

ii. 2% lime + 5% RHA provides best engineering and economic performance

iii. Material cost reduces by up to 40%

iv. The blend meets Kenyan low-volume road requirements

v. RHA is a viable low-cost stabilizer, supporting Kenya’s local-content and sustainability goals.

References

Mugai, C., Sabuni, B., Neyole, E., & Mugai, F. (2020). Influence of rice husk ash on subgrade bearing strength in stabilization of expansive soils for low volume roads in Kenya. *Civil and Environmental Research, 12*(11), 24–27.

Adhikary, S., & Jana, K. (2016). Potentials of rice husk ash as a soil stabilizer. *IJLRET.*

Ampera, A., & Aydogmust, O. (2005). Lime and cement stabilization of Chemnitz clay.

Choobbasti, A. J., et al. (2010). Influence of RHA and lime in soil stabilization. *Frontiers of Earth Science.*

Patel, M., & Patel, H. (2012). Stabilization of weak soils using industrial by-products.

Yadu, L., Tripathi, R. K., & Singh, D. (2011). Mechanical behavior of RHA–fly ash stabilized soils.

INSTRUCTIONS TO CONTRIBUTORS

The editorial staff of the AJERI requests contributors of articles for publication to observe the following editorial policy and guidelines accessible at https://www.iekenya.org/ in order to improve communication and to facilitate the editorial process.

Criteria for Article Selection

Priority in the selection of articles for publication is that the articles:

a. Are written in the English language
b. Are relevant to the application relevant of engineering and technology research and Innovation
c. Have not been previously published elsewhere, or, if previously published are supported by a copyright permission
d. Deals with theoretical, practical and adoptable innovations applicable to engineering and technology
e. Have a 150 to 250 words abstract, preceding the main body of the article
f. The abstract should be followed by a list of 4 to 8 "key Words"
g. Manuscript should be single-spaced under 4,000 words (approximately equivalent to 5-6 pages of A4-size paper)
h. Are supported by authentic sources, references or bibliography

Rejected/Accepted Articles

a. As a rule, articles that are not chosen for AJERI publication are not returned unless writer (s) asks for their return and are covered with adequate postage stamps. At the earliest time possible, the writer (s) is advised whether the article is rejected or accepted.
b. When an article is accepted and requires revision/modification, the details will be indicated in the return reply from the AJERI Editor, in which case such revision/modification must be completed and returned to AJERI within three months from the date of receipt from the Editorial Staff.
c. Complementary copies: Following the publishing, three successive issues are sent to the author(s)

Procedure for Submission

a. Articles for publication must be sent to AJERI on the following address:

The Editor

African Journal of Engineering Research and Innovation

P.O Box 41346- 00100

City Square Nairobi Kenya

Tel: +254 (20) 2729326, 0721 729363, (020) 2716922

E-mail: editor@iekenya.org

b. The article must bear the writer (s) name, title/designation, office/organization, nationality and complete mailing address. In addition, contributors with e-mail addresses are requested to forward the same to the Editor for faster communication.

For any queries, authors are requested to contact by mail (editor@iekenya.org).

PUBLISHER

The Institution of Engineers of Kenya (IEK)

P.O Box 41346- 00100

City Square Nairobi Kenya

Tel: +254 (20) 2729326, 0721 729363, (020) 2716922

Email: editor@iekenya.org

Website: www.iekenya.org

CONTENTS **Pages**